

Copyright
by
Hasnain Ahmad Khan
2009

**The Thesis Committee for Hasnain Khan
Certifies that this is the approved version of the following thesis:**

Shear Induced Relative Permeability Change in Uncemented Sands

**APPROVED BY
SUPERVISING COMMITTEE:**

Supervisor:

Jon E. Olson

Jon T. Holder

Shear Induced Relative Permeability Change in Uncemented Sands

by

Hasnain Ahmad Khan, B.Sc

Thesis

Presented to the Faculty of the Graduate School of

The University of Texas at Austin

in Partial Fulfillment

of the Requirements

for the Degree of

Masters of Science in Engineering

The University of Texas at Austin

December 2009

Dedication

To my parents, Dr. Fakhar Raza Khan and Dr. Ghazala Fakhar for guiding and supporting me in all the endeavors in life and for teaching me values and lessons that have been the source of success for me in life.

Acknowledgements

I would like to thank my supervisor Dr. Jon E. Olson for his advice and support for this research work. Dr. Olson's help, guidance and encouragement helped me achieve desired results for this research work. I would also like to acknowledge Dr. Jon Holder's help with the instrumentation and lab work. I really appreciate his friendly and helpful attitude.

I would also like to thank Antonio Bermudez, Glen Baum and Gary Miscoe for their help with instrumentation in the lab. I would also like to acknowledge the moral support and encouragement from my father Fakhar Raza Khan, my mother Ghazala Fakhar, my sisters Amna and Fatima and my brother Ali Khan to continue with graduate education.

And a special thanks to my friends Raza, Gilani, Farroukh, Farroukh Sheibani, Mehran, Raushan, Furqan, Umair, Fahad, Vinay, Vikrm, Faiz, Abhinav, Mehmet, Mehdi, Anwar and others for their help and support in various matters. I would also like to thank all the friends who helped me with the courses.

December 2009

Abstract

Shear Induced Relative Permeability Change in Uncemented Sands

Hasnain Ahmad Khan, M.S.E

The University of Texas at Austin, 2009

Supervisor: Jon E. Olson

Laboratory deformation of uncemented sand samples at low confining stress showed advantageous increases in absolute and relative permeabilities caused by localized shearing under dilatant volumetric strain conditions. In addition, associated residual oil saturation reduction caused by dilatant behavior would also be beneficial for recovery operations, indicating shear deformation could result in improved oil recovery factors.

The laboratory samples were constructed from Ottawa sand having three different grain size distributions, with median grain size varying from 100 to 420 microns. The initial permeability of these sands varied from 5 to 35 Darcies. A series of experiments were performed following two different effective stress paths, triaxial compression and radial extension. The triaxial compression tests followed a path of increasing mean stress while radial extension tests followed a path of decreasing mean stress. Stress magnitudes

used during the tests were designed to represent the conditions in shallow heavy oil reservoirs. Both test types were run to a maximum of 10% axial strain.

Absolute permeability measurements during triaxial loading at 50 psi confining stress showed decreasing permeability until about 2-3% axial strain, after which volumetric strain became dilatant absolute permeabilities increased at most by 20%. Radial extension tests performed with a constant axial stress of 200 psi showed dilatant volumetric strain at the very beginning of deformation, and absolute permeability was immediately enhanced, reaching peak enhancements of 50% over initial values. Interestingly, the permeability enhancement seen at 50 psi in the triaxial tests was suppressed by increasing the confining stress to 200 psi.

In addition to absolute permeability evaluation, relative permeability, initial water saturation and residual oil saturation were determined using the unsteady state JBN method. In the triaxial compression tests, relative permeability to oil (K_{ro}) decreased initially as the sample compacted but increased as the sample dilated. Relative permeability (K_{rw}) to water showed a trend that was similar to K_{ro} , but was not as pronounced as it is the case of oil. Residual oil saturation (S_{or}) increased during compaction but decreased during dilation. Radial extension tests produced increased relative permeability to oil and water, while residual oil saturation uniformly decreased with the sample dilated.

CT scans of the deformed sand samples indicated localized shear deformation along discrete, high porosity bands with radial symmetry. The porosity in the deformation bands was as much as 50% higher than the less deformed surrounding sand pack.

Table of Contents

List of Tables	x
List of Figures	xi
Chapter 1	1
Introduction.....	1
1.1 Steam Assisted Gravity Drainage (SAGD).....	3
1.2 Geomechanics and SAGD	6
1.3 Mechanism of Shear Band Formation and Dilation	8
1.4 Permeability Change of Unconsolidated Sands.....	10
1.5 Permeability Change in Consolidated Sandstones and Its Comparison to Unconsolidated Sands	12
1.6 Relative Permeability.....	13
1.6.1 Effect of Stress on Relative Permeability in Sandstones and Unconsolidated Sands	15
1.7 Research Objective	18
Chapter 2	19
Experimental Apparatus and Test Procedures	19
2.1 Experimental Apparatus.....	19
2.1.1 Triaxial Cell	19
2.1.2 Load Frame	21
2.1.3 Syringe Pumps and Glass Column.....	22
2.1.4 Vacuum Pump.....	23
2.1.5 Pressure Transducers	24
2.1.6 Mass Balance	25
2.1.7 Pore Fluids	25
2.2 Sand Properties And Grain Size Distribution	25
2.3 Porosity Measurement	27
2.4 Permeability Measurement	27
2.5 Volumetric Strain Calculations.....	29
2.6 Sample Permeability and Its Relation to Grain Size.....	32
2.7 Procedures.....	36
2.7.1 Sample Preparation	36
2.7.2 Sample Saturation	38
2.7.3 End Point Permeability and Relative Permeability (oil).....	39
2.7.4 End Point Permeability and Relative Permeability (water).....	40
2.7.5 Phase Saturations	40

Chapter 3	42
Results and Discussion	42
3.1 Triaxial Compression Tests	42
3.1.1 Stress-Strain Behavior	42
3.1.2 Volumetric Strain.....	47
3.1.3 Absolute Permeability.....	50
3.1.4 Relative Permeability.....	53
3.1.5 Residual Oil Saturation.....	58
3.1.6 Initial Water Saturation.....	60
3.1.7 Corey Type Curves for Relative Permeability.....	61
3.2 Radial Extension Tests.....	66
3.2.1 Stress-Strain Behavior	66
3.2.2 Volumetric Strain.....	70
3.2.3 Permeability	72
3.2.4 Relative Permeability.....	75
3.2.5 Residual Oil Saturation	78
3.2.6 Initial Water Saturation.....	80
3.2.7 Corey Type Relative Permeability Curves	81
3.3 Cat Scan Images of the Sand Packs and Porosity Analysis.....	85
Chapter 4	95
Summary and Conclusions	95
4.1 Field Applications.....	96
4.2 Future Research and Recommendations.....	97
Appendix A: Grain Size Details	98
Appendix B: Stress-Strain and Volumetric Strain curves.....	101
References.....	117
Vita.....	122

List of Tables

Table 1.1: Major Commercial production methods of heavy oils (Clark <i>et al.</i> , 2007).....	3
Table 2.1: Dead volume of the apparatus.	41
Table 3.2: K_{ro} values and their comparison to values from repeated experiments (triaxial compression with 50 psi and 200 psi confining stress).....	55
Table 3.3: K_{rw} values and their comparison to values from repeated experiments (triaxial compression with 50 psi and 200 psi confining stress).....	55
Table 3.4: Residual oil saturation for the triaxial compression tests performed with 50 psi and 200 psi confining stress.	59
Table 3.5: Porosity and permeability of sand samples with a 200 and 500 psi constant axial stress and decreasing confining stress.	73
Table 3.6: K_{ro} in the radial extension tests with a constant 200 and 500 psi axial load and decreasing radial stress. The table also contains the values for the repeated experiments for comparison with the values obtained from initial experiments.	76
Table 3.7: K_{rw} in the radial extension tests with a constant 200 and 500 psi axial load. The table also contains the values for the repeated experiments for comparison with the values obtained from initial experiments.	77
Table 3.8: Residual oil saturation for the three types of sands with decreasing confining pressure and constant axial stress of 200 psi.	79

List of Figures

Figure 1.1: Current production and future forecast of oil production from Oil sands and Conventional oil fields in western Canada (Crude Oil Forecast, Markets and Pipeline Expansions, Canadian Association of Petroleum producers, June 2009).....	1
Figure 1.2: Schematic of SAGD process. The steam injector at the top causes the formation of steam envelope around the injection which pushes the oil towards the producer. Oil moves under the influence of gravity towards the producer, rather than steam drive.....	4
Figure 1.3: Vertical cross section through growing steam chamber. Steam reduces the oil viscosity, which then drains towards the producer under the influence of gravity.....	5
Figure 1.4: Schematic illustration of stress paths followed by Touhidi-Baghini (1998). Path 1 is the stress path representing the thermal expansion in the reservoir. This is a typical drained compression triaxial stress. Path 2 is referred to as the constant mean effective stress path. Path 3 and 4 represent the effects of decreasing confining stress.	8
Figure 1.5: Development of shear bands at low confining stress. The CAT scan (computer aided tomography) was taken at different points along the stress-strain curve (marked on the curve). Darker areas in the picture show the formation and growth of shear bands with increasing axial strain (from Li <i>et al.</i> , 2002).....	9
Figure 1.6: Shear bands in sheared Athabasca oil sand (from Wong, 2004).....	10
Figure 1.7: Behavior of Porosity in experiments conducted by Morita <i>et al.</i> , (1992) (from Morita <i>et al.</i> , 1992). Porosity shows a decrease initially with increasing stress and an increase near the peak stress. This Figure is comparable to Figure 1.10 for Ottawa sands which show a similar behavior.	13
Figure 1.8: Change in relative permeability to oil and water with increasing overburden (from Ali <i>et al.</i> , 1987). Reduced relative permeability to oil and a slight decrease in relative permeability to water is observed.	16
Figure 1.9: Effective permeability to water under isotropic unloading and triaxial compression. Increase in effective permeability is observed in all the tests (from Wong <i>et al.</i> , 2001).	17
Figure 2.1: Schematic of the apparatus.....	20

Figure 2.2: Triaxial cell.....	21
Figure 2.3: Load Frame.....	22
Figure 2.4: Arrangement for injecting Oil into the sample.....	23
Figure 2.5: Arrangement of pressure transducers.....	24
Figure 2.6: Grain size distribution of the sands used in the experiment. The coarsest sand is the Medium Ottawa while the finest is Lower Fine Ottawa. Athabasca oil sand has a grain size distribution similar to that of Lower Fine Ottawa (Yaich, 2008).....	26
Figure 2.7: SEM images (from Yaich, 2008) of Medium Ottawa (Left) and Lower Fine (Right) Ottawa sand.....	26
Figure 2.8: Volume change due to decreasing confining pressure for an aluminum sample initially loaded isotropically to 200 psi.....	32
Figure 2.9: Initial permeability as a function of mean grain size diameter. Mean grain diameter determines the permeability of the sand sample.....	33
Figure 2.10: Initial porosity versus permeability.....	34
Figure 2.11: Calculated versus measured initial permeability with $A=9.75$ (Kozeny-Carman equation). The black line represents the line $Y=X$ in the graph.....	36
Figure 2.12: Porosity values obtained by wet vibration. Uniform porosities can be obtained by using wet vibration.....	38
Figure 3.1: Stress strain curves in triaxial compression for the sand samples tested with 50 psi confining stress (LF-Lower Fine Ottawa, LA-Lower Amalgamated Ottawa, MO-Medium Ottawa).....	45
Figure 3.2: Stress strain curves in triaxial compression for the Lower Fine Ottawa samples tested with constant 50 and 200 psi confining stress.....	46
Figure 3.3: Volumetric strain for triaxial compression tests done with 50 psi confining pressure (LF-Lower Fine Ottawa, LA-Lower Amalgamated Ottawa, MO-Medium Ottawa).....	49

Table 3.1: Initial porosity and permeability of the different sand samples during triaxial compression with 50 and 200 psi constant confining stress and increasing values of axial strain.....	51
Figure 3.4: Permeability of sand samples in triaxial compression with 50 and 200 psi confining stress.	52
Figure 3.5: Normalized permeability of sand samples in triaxial compression with 50 and 200 psi confining stress.....	53
Figure 3.6: End point relative permeability to oil during triaxial compression with 50 and 200 psi confining stress. Lower Fine Ottawa had a lower end point relative permeability as compared to the other two sands.	56
Figure 3.7: End point relative permeability to water in triaxial compression with 50 and 200 psi confining stress.....	57
Figure 3.8: Residual oil saturation trend for the triaxial compression tests with 50 and 200 psi confining stress.....	60
Figure 3.9: Initial water saturation for the triaxial compression tests with 50 psi and 200 psi confining stress.....	61
Figure 3.10: Relative permeability curves for Lower Fine Ottawa samples at 2%, 5% and 0% axial strain. The relative permeability curves are plotted using end point K_{ro} and K_{rw} derived from triaxial compression tests at 50 psi confining stress. The K_{ro} curves moved downwards for compaction (2% axial strain, indicating a reduction in K_{ro}) and upwards for dilation (5% axial strain, indicating an increase in relative permeability to oil). The end point K_{rw} increased but the curves do not show a clearly defined trend.....	63
Figure 3.11: Relative permeability curves for Lower Amalgamated Ottawa samples at 2%, 5% and 10% axial strain. The relative permeability curves are plotted using end point K_{ro} and K_{rw} derived from triaxial compression tests with 50 psi confining stress. The K_{ro} curves moved downwards (decrease in K_{ro}) for compaction (2% axial strain) and upwards (increase in K_{ro}) for dilation (5% axial strain). The end point K_{rw} increased but the curves do not show a clearly defined trend.....	64
Figure 3.12: Relative permeability curves for Medium Ottawa specimens at 2%, 5% and 10% axial strain. The relative permeability curves are plotted using end point K_{ro} and K_{rw} derived from triaxial compression tests with 50 psi confining stress. The oil relative permeability curves moved downwards (decrease in K_{ro}) for compaction (2% axial strain)	

and upwards (increase in K_{ro}) for dilation (5% axial strain). The end point K_{rw} increased but the curves do not show a clearly defined trend. 65

Figure 3.13: Stress-strain curves for radial extension tests with constant axial stress of 200 psi and decreasing radial stress (LF-Lower Fine Ottawa, LA-Lower Amalgamated Ottawa, MO-Medium Ottawa). 68

Figure 3.14: Stress-strain curves for radial extension tests (Lower Fine Ottawa) with constant axial stress of 200 and 500 psi and decreasing radial stress. 69

Figure 3.15: Volumetric strain curves for radial extension tests with constant axial stress of 200 and 500 psi and decreasing confining stress (LF-Lower Fine Ottawa, LA-Lower Amalgamated Ottawa, MO-Medium Ottawa). 71

Figure 3.15: Permeability of different sand samples tested at different values of axial strain with a constant 200 and 500 psi axial stress. Increasing axial strain values denote a decreasing confining stress and increasing permeability. 74

Figure 3.16: Normalized permeability of different sand samples tested at different values of strain with a constant 200 and 500 psi axial stress. Increasing axial strain values denote a decreasing confining stress and increasing permeability. 75

Figure 3.17: Comparison of end point relative permeability to oil in the three sands at a constant axial stress of 200 and 500 psi. All the sands show an increase in end point relative permeability to oil. 77

Figure 3.18: Comparison of end point relative permeability to water in the three sands at a constant axial stress of 200 and 500 psi. All the sands show an increase in end point relative permeability to water. 78

Figure 3.19: Change in residual oil saturation with increasing axial strain in radial extension tests with decreasing confining pressure and a constant 200 psi axial stress. .. 80

Figure 3.20: Change in initial water saturation during the radial extension tests with decreasing confining stress and constant axial stress of 200 and 500 psi. 81

Figure 3.21: Relative permeability curves for oil and water for Lower Fine Ottawa in radial extension tests with 200 psi axial stress. The K_{ro} curves show a clear shift upwards with increasing strain, indicating an increase in K_{ro} at any given water saturation. While K_{rw} curves do not show a well defined trend. 82

Figure 3.22: Relative permeability curves for oil and water for Lower Amalgamated Ottawa in radial extension tests with 200 psi axial stress. The K_{ro} curves show a clear shift upwards with increasing strain, indicating an increase in K_{ro} at any given water saturation. But the shift is less as compared to Lower Fine Ottawa. The K_{rw} curves show a downward shift with increasing strain, but it not a well defined or a considerable change. 83

Figure 3.23: Relative permeability curves for oil and water for Medium Ottawa in radial extension tests with 200 psi axial stress. The K_{ro} curves show a clear shift upwards with increasing strain, indicating an increase in K_{ro} at any given water saturation. But the shift is less as compared to Lower Fine Ottawa. The K_{rw} curves show a downward shift with increasing strain, but it not a well defined or a considerable change. 84

Figure 3.24: Images from the triaxial compression tests on Lower Fine Ottawa with constant 50 psi confining pressure. (a)The pictures show the change in fracture pattern when moving from top of the sample to the middle of the sand sample. (b) The pictures show the change in fracture pattern when moving from middle of the sample to the bottom of the sand sample. 88

Figure 3.25: Images from the triaxial compression tests on Lower Fine Ottawa with constant 200 psi confining pressure. (a) The pictures show the change in fracture pattern when moving from top of the sample to the middle of the sand sample. (b)The pictures show the change in fracture pattern when moving from middle of the sample to the bottom of the sand sample. 89

Figure 3.26: Images from the radial extension tests on Lower Fine Ottawa with constant 200 psi axial stress and decreasing confining stress. (a) The pictures show the change in fracture pattern when moving from top of the sample to the middle of the sand sample. Fractures are wider than the fractures which develop in triaxial compression tests. (b) The pictures show the change in fracture pattern when moving from top of the sample to the middle of the sand sample. Fractures are wider than the fractures which develop in triaxial compression tests. 90

Figure 3.27: Images from the radial extension tests on Lower Fine Ottawa with constant 500 psi axial stress and decreasing confining stress. (a) The pictures show the change in fracture pattern when moving from top of the sample to the middle of the sand sample. Fractures are wider than the fractures which develop in triaxial compression tests. (b) The pictures show the change in fracture pattern when moving from middle of the sample to the bottom of the sand sample. Fractures are wider than the fractures which develop in triaxial compression. 91

Figure 3.28: Radial extension test with 500 psi constant axial stress (image slice taken from the middle of the sample) (a) CT number variation along the traverse. (b) Image of

the slice along with the traverse (yellow line). (c) Porosity analysis for a slice from the middle of the sample. The humps in porosity curve denote the porosity of the deformation bands..... 92

Figure 3.29: Radial extension test with 500 psi constant axial stress (image slice taken from the bottom of the sample) (a) CT number variation along the traverse. (b) Image of the slice along with the traverse (yellow line). (c) Porosity analysis for a slice from the middle of the sample. The humps in porosity curve denote the porosity of the deformation bands..... 93

Figure 3.30: Triaxial compression test with 200 psi constant confining stress (a) CT number variation along the traverse for the slices. (b) Image of the slices along with the traverse (yellow line). (c) Porosity analysis for a slice from the middle of the sample. The humps in porosity curve denote the porosity of the deformation bands. 94

Figure A1: Grain size distribution of the Medium Ottawa 99

Figure A2: Grain size distribution of the Lower Fine Ottawa 99

Figure A3: Grain size distribution of the Lower Amalgamated Ottawa (LA)..... 100

Figure B1: Stress strain curves in triaxial compression (at 2%, 3%, 5% and 10% axial strain) for Lower Fine Ottawa (LF) samples tested with 50 psi confining stress. 101

Figure B2: Stress strain curves in triaxial compression (at 2%, 3%, 5% and 10% axial strain) for Lower Amalgamated Ottawa (LA) samples tested with 50 psi confining stress..... 102

Figure B3: Stress strain curves in triaxial compression (at 1%, 2%, 3%, 5% and 10% axial strain) for Medium Ottawa (MO) samples tested with 50 psi confining stress. 103

Figure B4: Volumetric strain in triaxial compression tests (at 1%, 2%, 3%, 5% and 10% axial strain) for Lower Fine Ottawa (LF) done with 50 psi confining pressure. 104

Figure B5: Volumetric strain in triaxial compression tests (at 1%, 2%, 3%, 5% and 10% axial strain) for Lower Amalgamated Ottawa (LA) done with 50 psi confining pressure. 105

Figure B6: Volumetric strain in triaxial compression tests (at 1%, 2%, 3%, 5% and 10% axial strain) for Medium Ottawa (MO) done with 50 psi confining pressure. 106

Figure B7: Differential stress, confining stress and axial stress plotted against axial strain for Lower Fine Ottawa Specimens with 200 psi constant axial stress.....	107
Figure B8: Differential stress, confining stress and axial stress plotted against axial strain for Lower Amalgamated Ottawa Specimens with 200 psi constant axial stress.....	108
Figure B9: Differential stress, confining stress and axial stress plotted against axial strain for Medium Ottawa Specimens with 200 psi constant axial stress.....	109
Figure B10: Differential stress, confining stress and axial stress plotted against axial strain for Lower FineOttawa Specimens with 500 psi constant axial stress.....	110
Figure B11: Stress-strain curves for radial extension tests (at 2%, 5% and 10% axial strain) for Lower Fine Ottawa (LF) with constant axial stress of 200 psi and decreasing radial stress.....	111
Figure B12: Stress-strain curves for radial extension (at 2%, 5% and 10% axial strain) tests for Lower Amalgamated Ottawa (LA) with constant axial stress of 200 psi and decreasing radial stress.	112
Figure B13: Stress-strain curves for radial extension tests (at 2%, 5% and 10% axial strain) for Medium Ottawa (MO) with constant axial stress of 200 psi and decreasing radial stress.....	113
Figure B14: Volumetric strain curves for radial extension tests (at 2%, 5% and 10% axial strain) for Lower Fine Ottawa (LF) with constant axial stress of 200 and decreasing confining stress.	114
Figure B15: Volumetric strain curves for radial extension tests (at 2%, 5% and 10% axial strain) for Lower Amalgamated Ottawa (LA) with constant axial stress of 200 and decreasing confining stress	115
Figure B16: Volumetric strain curves for radial extension tests (at 2%, 5% and 10% axial strain) for Medium Ottawa (MO) with constant axial stress of 200 and decreasing confining stress.	116

CHAPTER 1

Introduction

According to the International Energy Agency (IEA), there are 6 trillion barrels in place of heavy oil, bitumen and extra-heavy oil worldwide. There are 2.5 trillions bbl of heavy oil in Western Canada, 1.5 bbl in Venezuela, and 1.1 trillion bbl in Russia. 300 billion barrels out of the total 2.5 trillion barrels in Canada are considered to be recoverable under current technology and economic conditions. Heavy oil production has been on the rise for the past decade due to the declining production from conventional oil producing assets and improved technologies that have helped increase recovery factors from heavy oil reservoirs. Figure 1.1 shows the increasing trend in heavy oil production.

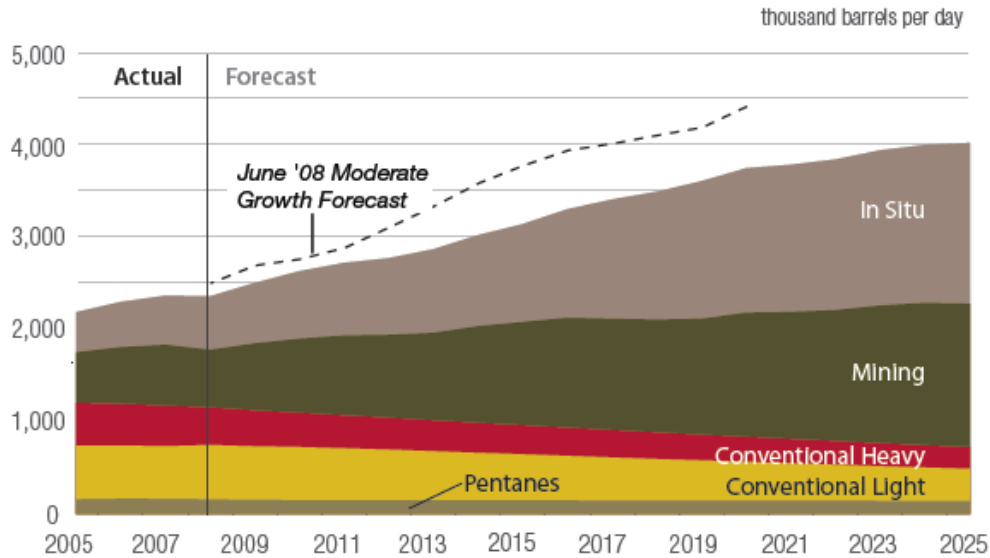


Figure 1.1: Current production and future forecast of oil production from Oil sands and Conventional oil fields in western Canada (Crude Oil Forecast, Markets and Pipeline Expansions, Canadian Association of Petroleum producers, June 2009).

Heavy oils are unconventional oil resources that are characterized by high viscosities (i.e. resistance to flow) and high densities compared to conventional oil. Heavy oil is typically produced from geologically young formations, with ages from the Miocene to Pleistocene (Gallup, 1974). In general, heavy oil deposits such as the Athabasca sands in Canada consist of uncemented clastic sediments deposited in a variety of depositional environments. These unconsolidated reservoirs are usually characterized by high porosity (30-35% porosity) and permeability (0.5 Darcy to 20 Darcy; Bachu *et al.*, 1992). The reservoirs are shallow and have less effective seals, allowing them to be exposed to conditions conducive to formation of heavy oils. Conventional light oil formed in deeper formations migrates to shallow reservoirs where lower overburden pressure allows more volatile fractions of the crude oil to escape. Shallow reservoirs having low reservoir temperature encourage rapid growth of bacterial populations (Wilhelms *et al.*, 2001). Degradation by bacteria converts lighter oil to heavier oil by breaking down medium and lighter fractions into less volatile fractions and gas, which later escape the fluid mixture leaving behind the heavier fractions (Clark *et al.*, 2007).

The production from heavy oil reservoirs may be divided into two phases- initial cold production and subsequent thermal recovery. Cold production uses the natural reservoir pressure drive to produce oil. In some cases a cold EOR (enhanced oil recovery) method such as waterflooding is used to help displace the oil and increase recovery. However, the drawback for cold production is the low recovery factor, typically 6% to 15% (Clark *et al.*, 2007).

Thermal recovery is the injection of steam into heavy oil reservoirs to reduce the oil viscosity and improve the recovery from the heavy oil reservoirs (Meyer *et al.*, 2003). Injected steam raises the reservoir temperature leading to an oil viscosity reduction and improved oil mobility (Kumar *et al.*, 2005). Several methods such as cyclic steam

injection (CSS) and steam assisted gravity drainage (SAGD) are included in the thermal recovery. SAGD is a more recent development than cyclic steam stimulation or simple steam floods. Table 1.1 lists the methods being used for heavy oil production.

Method	Current Usage	Comment
Open –pit Mining	Used for shallow oil sands	Reasonably high recovery (over 70%) , but high environmental impact
Cold heavy oil production	Initial recovery phase	Low recovery factor (5-10%), needs good gas/oil ratio (GOR),
Steam flood	Used in USA, Canada, Indonesia, many others	High recovery factor (50-70%)
Cyclic steam stimulation (CSS)	Used in USA, Canada, Indonesia, many others	Fair recovery factor (20-40%)
Steam assisted gravity drainage (SAGD)	Used in Canada mostly	Used for shallower oil deposits with a fair to high recovery.

Table 1.1: Major Commercial production methods of heavy oils (Clark *et al.*, 2007)

1.1 STEAM ASSISTED GRAVITY DRAINAGE (SAGD)

SAGD has been successful in revolutionizing the economics of heavy oil recovery (Albahlani *et al.*, 2008) and instrumental in increasing the recovery factors from heavy oil reservoirs, making it a technology most suitable for shallow heavy oil reservoirs (Butler, 1998). SAGD is a special form of steam flooding where the producer and injector wells are horizontal. Conventional steam flooding using vertical wells is hampered by steam override, where the less dense steam rises to the top of the formation and bypasses

the lower sections, resulting in poor sweep and low recovery (Kumar *et al.*, 2005). Early breakthrough of the steam front at the producer also hampers recovery. SAGD can overcome these gravity override effects mainly due to a different well geometry.

In SAGD, the injector well is drilled horizontally and directly above the producer (Figure 1.2). The wells are drilled at a vertical separation of 3-7 meters depending on the oil viscosity. The horizontal sections are typically 500 to 1,500 m long.

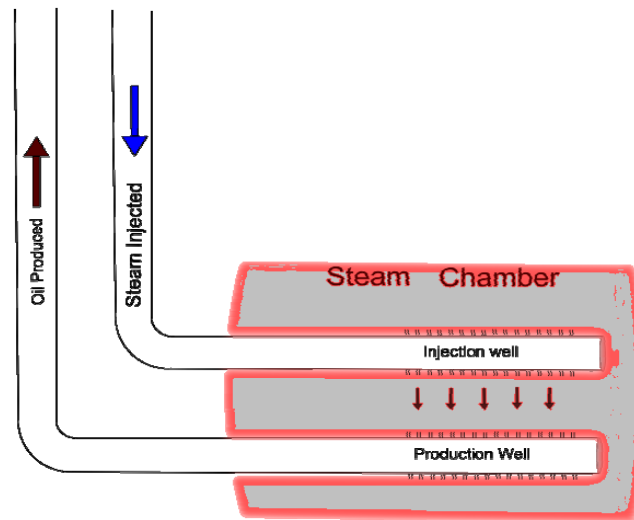


Figure 1.2: Schematic of SAGD process. The steam injector at the top causes the formation of steam envelope around the injection which pushes the oil towards the producer. Oil moves under the influence of gravity towards the producer, rather than steam drive.

Steam from the injector moves upwards and sideways into the surrounding formation. Gradually, it forms a zone around the injector known as the steam chamber. Heat travels by convection to the edge of the steam chamber, where the steam releases its heat to oil and formation, and condenses into water eventually. The viscosity of the oil in and around the steam chamber is reduced and the oil moves towards the producer under the influence of gravity (Figure 1.3).

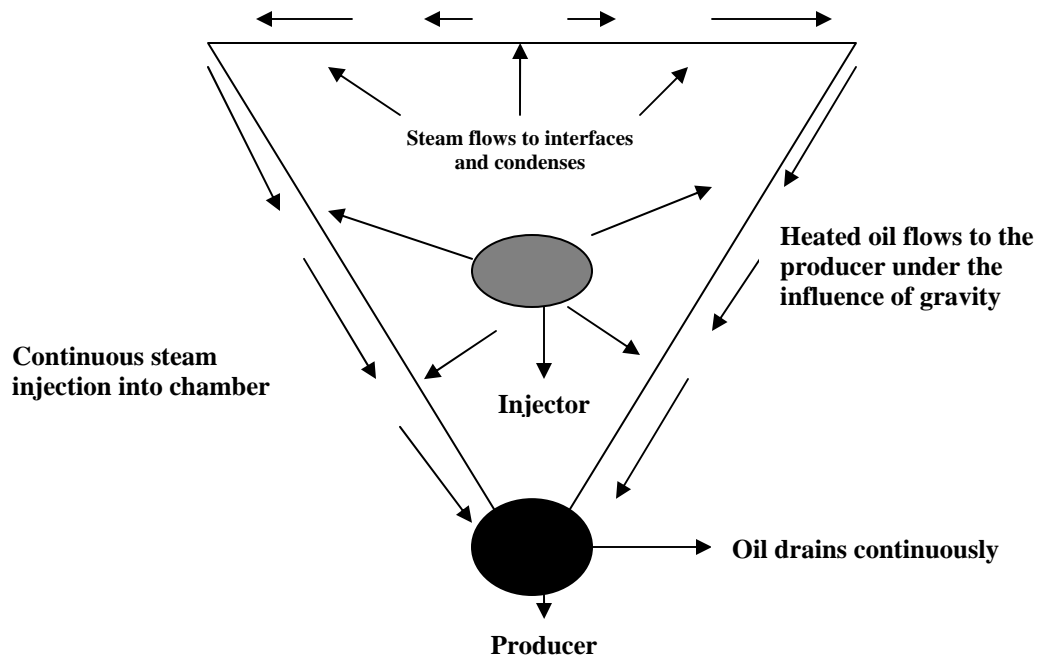


Figure 1.3: Vertical cross section through growing steam chamber. Steam reduces the oil viscosity, which then drains towards the producer under the influence of gravity.

The stress path caused by steam injection in SAGD is believed to enhance formation permeability (Collins et al., 2002). The expanding steam chamber causes a pore pressure increase which produces a path of decreasing mean effective stress. Conversely, the immediate areas outside the steam chamber may experience an increasing mean stress path because of thermal expansion associated with increasing temperature (Chalaturnyk *et al.*, 1997, Tohidi-Baghini, 1998, Oldakowski, 1994 and Yaich, 2008). Deformation may cause dilation which can result in an increase in porosity and permeability. Chalaturnyk *et al.*, (1997) inferred an increase of 30% to 50% increase in the absolute permeability of oil sands in field trials near Fort McMurray, Canada. Tohidi-Baghini (1998) measured a 60% to 100% increase in permeability in his deformation experiments with non-bituminous Mc-Murray sand samples. Field

observations and lab tests both indicate that shear failure of the sand results in a net increase in absolute permeability.

1.2 GEOMECHANICS AND SAGD

Increased pore pressures result in the unloading of a formation due to the decrease in the effective stress. The concept of effective stress was introduced by Terzaghi (1943), who proposed that the total stresses are divided between the particle to particle stress and the pore fluid. The effective stress mathematically is given as

$$\sigma = S - P_p \quad (1.1)$$

where

σ = effective stress,

P_p = pore pressure, and

S = total stress.

If the differential stresses in the reservoir are high enough, the reservoir may experience shear dilation and an associated increase in permeability when pore pressure is increased (Li, 2006).

Temperature increase in SAGD results in thermal expansion of the sand. Sands can move freely (expand) in the vertical direction due earth's free surface, but horizontally the expansion is constrained by surrounding rock formations. This leads to a net increase in horizontal stresses while the vertical stresses remain constant. Zoback *et al.*, (1989) identified that the Canadian oil sands are in a thrust faulting regime, where $S_{Hmax} > S_{hmin} > S_v$. Thus an increase of in situ maximum horizontal stress (S_{Hmax}) results in an increase in differential stress and increasing mean stress.

Two main loading paths (Figure 1.4) were identified by Chalaturnyk *et al.*, (1997), Tohidi-Baghini (1998), Oldakowski (1994) and Yaich (2008) to be followed in SAGD operations. First was the path of mean increasing stress and the

other was the path of decreasing mean stress. Chalaturnyk *et al.*, (1997) also identified that an additional isotropic stress path was followed during SAGD operations; this loading path was attributed due to increasing pore pressure resulting in equal reduction in the maximum and minimum principal stresses. Tohidi-Baghini's (1998) investigation was based on a total of four loading paths which all simulated either path of mean increasing or mean decreasing stress but unlike Chalaturnyk *et al.*, (1997) he did not follow the isotropic stress path. Odakowski (1994) followed loading paths similar to those followed by Tohidi-Baghini (1998) and also proposed that the loading path of mean increasing stress simulated stress conditions that occur laterally in front of the steam chamber. Yaich (2008) in his experimental investigation of the effect of stress paths and shear failure on the permeability of unconsolidated sands followed the triaxial compression (path of mean increasing stress) and the radial extension (path of mean decreasing stress) path.

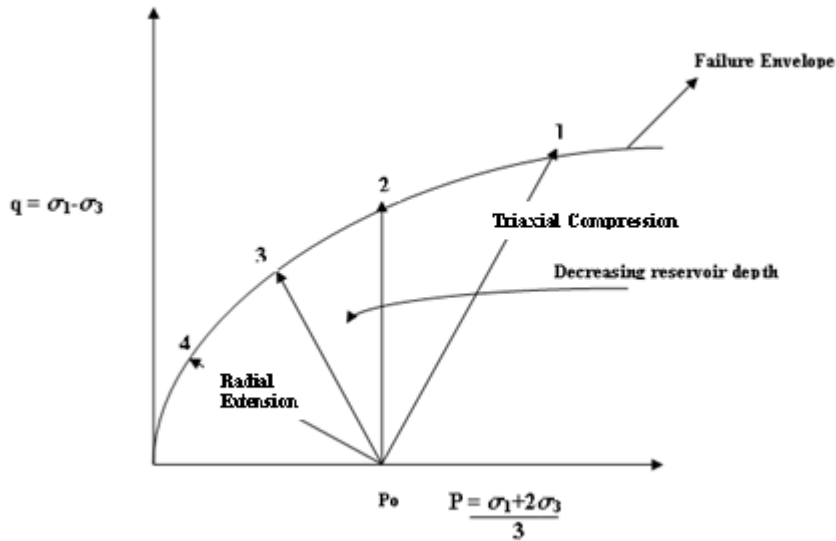


Figure 1.4: Schematic illustration of stress paths followed by Touhidi-Baghini (1998). Path 1 is the stress path representing the thermal expansion in the reservoir. This is a typical drained compression triaxial stress. Path 2 is referred to as the constant mean effective stress path. Path 3 and 4 represent the effects of decreasing confining stress.

1.3 MECHANISM OF SHEAR BAND FORMATION AND DILATION

Deformation bands represent a common type of shear strain localization in unconsolidated sandstones. In porous rock and sediments, brittle deformation is largely experienced by the formation of fault like structure referred to as the deformation bands (Fossen *et al.*, 2007). Deformation bands are usually a few millimeters thick tabular zones of localized strain. Increasing mean stress on sand samples causes it to compact initially and after a certain increase of stress, shear bands are formed in localized planes. This causes an increase of porosity (dilatancy) of the sand sample. These deformation bands show a dominant component of shear displacement. Deformation bands are confined to porous media with high porosities (usually in excess of 15%). Oil sands have high porosities in the range of 30-35% making them ideal for the formation of

deformation shear bands at, before and after shear failure. Li *et al.*, (2002) showed the development of shear bands in unconsolidated sand using Computer Aided Tomography (CAT) scans (Figure 1.5). Wong (2004) observed the development of shear bands in Athabasca oil sands using computer aided tomography (Figure 1.6). The lighter areas in Figure 1.6 indicate shear bands that have higher porosity and permeability. Shearing creates a dual porosity dual permeability system to develop which enhances the productivity due to an increase in permeability.

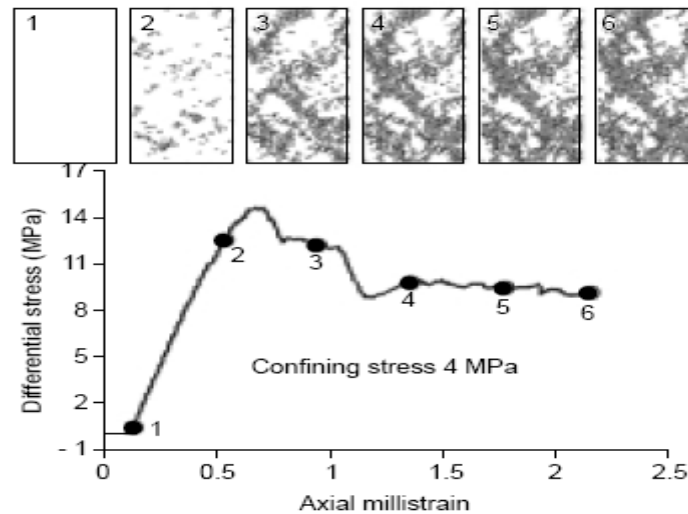


Figure 1.5: Development of shear bands at low confining stress. The CAT scan (computer aided tomography) was taken at different points along the stress-strain curve (marked on the curve). Darker areas in the picture show the formation and growth of shear bands with increasing axial strain (from Li *et al.*, 2002).

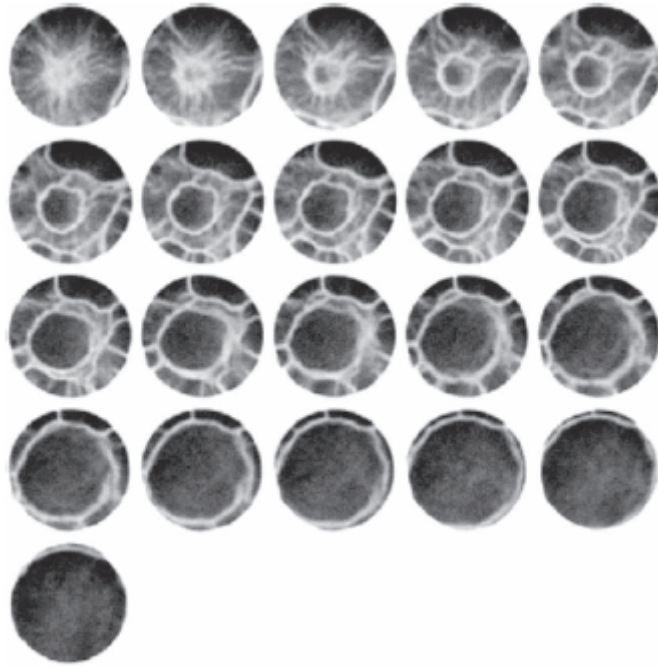


Figure 1.6: Shear bands in sheared Athabasca oil sand (from Wong, 2004)

The lighter areas in Figure 1.6 indicate shear bands that have higher porosity and permeability. Shearing creates a dual porosity dual permeability system to develop which enhances the productivity due to an increase in permeability.

1.4 PERMEABILITY CHANGE OF UNCONSOLIDATED SANDS

Scott *et al.*, (1991) conducted an experimental investigation on the change in permeability due to steam stimulation of using Cold Lake oil sands. Triaxial compression test (1-1.5 MPa (145-220 psi) confining stress) generated an increase of 32% in permeability. Their tests also indicated that for confining stresses greater than 2 MPa (290 psi) no significant dilation was observed. This result was comparable to Zoback *et al.*, (1975) results, who reported that at high confining stress Ottawa sand samples showed a reduction in permeability despite shearing of the sample. Similarly triaxial compression test results from Oldakowski (1994) and Tohidi-Baghini's (1998)

investigation, showed initial compaction followed by shear dilation. Dilation reached a maximum value just before specimen failure or immediately after specimen failure.

Tohidi-Baghini (1998) also observed that strength and volumetric strain of a sand sample was dependent on initial porosity. Higher porosity samples had a lower volumetric strain and were less strong (lower peak stress). Yaich (2008) also observed that sand samples with higher initial porosities had a lower peak stress and showed a dominant compactive behavior with little or no dilation. Sand samples with lower initial porosities showed more dilatancy and higher peak stress before failure. He proposed that samples with lower initial porosity developed wider failure planes that were more localized (due the higher stress drop after failure).

Oldakowski's (1994) sand samples had an initial porosity ranging from 35% to 39%. At a 6% axial strain value he observed a 5.5 % volumetric strain and a permeability increase ranging between 25% and 65%. The value of confining stress in his triaxial compression experiments was a maximum of 530 KPa (77 psi). He also conducted radial extension test, where samples were isotropically loaded to 1000 KPa (145.5 psi) after which the confining pressure was reduced to 10 KPa (14.5 psi) while keeping the axial stress constant. The permeability increase in his experiments was from 75% to 110%.

The average initial porosities in Tohidi-Baghini's (1998) samples ranged from 33% to 35%. Initial permeability of the samples was between 1.5 and 4 Darcy and both horizontal and vertical cores were used in the experiments. These experiments were done at low effective stresses, the initial effective mean stress was 250 kPa (36 psi) and the maximum differential stress was 1100 kPa (160 psi). For triaxial compression tests the permeability increased between 30-50 %. Radial extension (isotropic unloading) test displayed a larger increase in permeability that varied between 50-70%. The vertical core

specimen showed both higher dilation and much higher permeability enhancement than horizontal cores.

1.5 PERMEABILITY CHANGE IN CONSOLIDATED SANDSTONES AND ITS COMPARISON TO UNCONSOLIDATED SANDS

At this point we consider the change in permeability with stress in consolidated rocks and unconsolidated sands. Consolidated rocks such as cemented sandstone usually under go compaction when the stresses are increased and increasing shear stresses usually cause brittle failure of the rock.

Holt (1990) reported experimental results on the stress sensitivity of cemented Jurassic sandstones. Samples were loaded under triaxial compression and extension stress paths at confining pressure from 3.45 MPa (500 psi) to 34.5 MPa (5003 psi). The permeability reduction (about 50 % permeability reduction) took place from 60% to 90% of the peak stress. Ruistuen *et al.*, (1999) studied the stress dependency of Jurassic sandstones obtained from Oseberg field in Norway. Samples were loaded under triaxial stress conditions at confining stresses of 10-18 MPa (1450-2610 psi). Permeability measurements were conducted in the axial (vertical) direction, parallel to the maximum stress direction. The results showed a trend towards permeability reduction (a maximum of 20% decrease) with increasing stress and a sharp decline in permeability at failure. The permeability reduction was attributed to the grain scale splitting (crushing) that occurs due to the tensile failure of the grains.

Morita *et al.*, (1992) reported results on the effects of stress on Berea sandstone samples. The samples were tested in triaxial compression. Generally, the permeability decreased but the axial permeability started increasing immediately before failure at lower confining pressures. The results were attributed to initial compaction and porosity decrease at low stress levels and onset of dilatancy (porosity increase) before failure

(Figure 1.7). Microcracks parallel to the maximum stress direction were held responsible for the increase in permeability and dilatancy. The permeability increase in the axial and radial direction was not more than 10% at peak stress. These results are comparable to the results observed in unconsolidated sands, but permeability increase is much higher in unconsolidated sands.

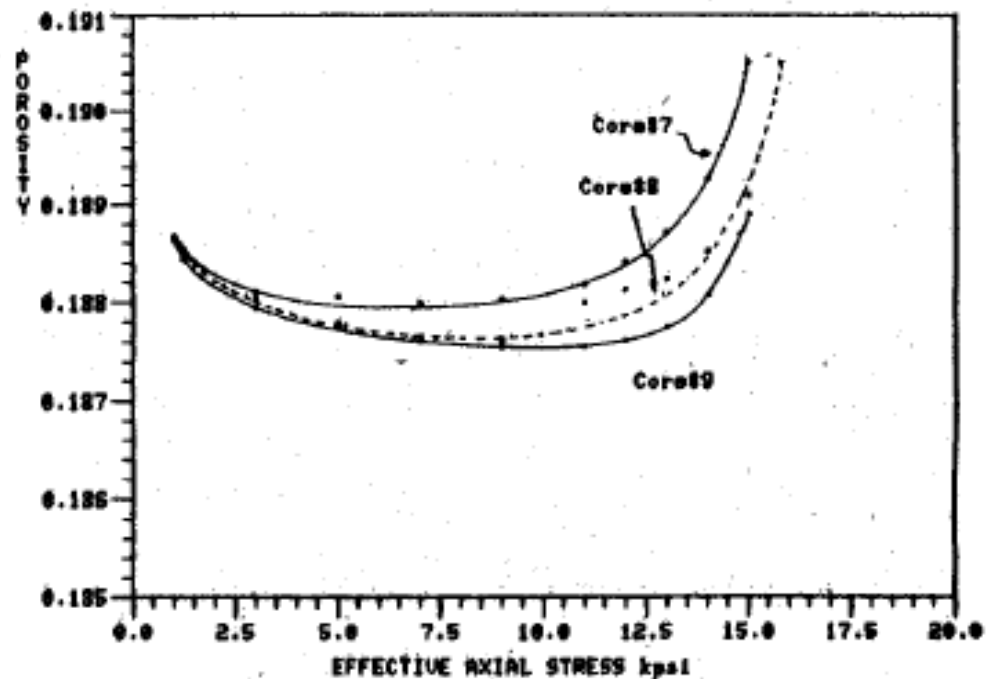


Figure 1.7: Behavior of Porosity in experiments conducted by Morita *et al.*, (1992) (from Morita *et al.*, 1992). Porosity shows a decrease initially with increasing stress and an increase near the peak stress. This Figure is comparable to Figure 1.10 for Ottawa sands which show a similar behavior.

1.6 RELATIVE PERMEABILITY

Relative permeability is a dimensionless quantity that describes how easily one fluid is able to flow in the presence of another fluid in a porous medium. Fluids in porous media are typically referred to as phases, for example oil and water are considered to be two different phases. Relative permeability of a fluid is a function of the fluid saturation

for a given porous medium (Lake, 1989). Relative permeability in oil reservoirs is of prime importance, as it is used in varied applications of reservoir engineering such as in the context of injection of fluids into the reservoir. Relative permeability can help estimate recoverable hydrocarbon reserves, production rates of the fluids present and the displacement efficiency of a displacement process.

Lab scale measurements of the relative permeability are made using steady state, unsteady state, centrifuge and capillary pressure methods. In steady state methods, a fixed ratio of fluids is injected through the sand pack or the core. The injection of the fluids is continued until saturation and pressure gradients stabilize. This technique was pioneered by Morse *et al.*, (1947) and later modified by Osoba *et al.*, (1951). Steady state methods are straightforward and have few uncertainties. The main drawback of this method is the amount of time required (several hours or days in case depending on the core parameters to achieve steady state) to generate a single point on the relative permeability versus saturation curve.

Unsteady state or dynamic displacement methods are much less time consuming. Relative permeability curves can be generated in a single experiment. In unsteady state methods production data from the core is monitored and the relative permeability curves are then generated on the basis of mathematical modeling of the process. The theory behind the dynamic displacement was developed by Buckley and Leverett (1942) and further extended by Welge (1952). Johnson *et al.*, (1959) developed what is known as the Johnson, Bossler and Naumann (JBN) method to calculate individual phase relative permeability from experimental data.

Osoba *et al.*, (1951), Richardson *et al.*, (1952), Owens *et al.*, (1956) and Richardson (1957) have compared the results from unsteady state and steady state

experiments. It has been concluded that comparable results are achieved by both type of experiments. The unsteady state displacement method was used in this research.

1.6.1 Effect of Stress on Relative Permeability in Sandstones and Unconsolidated Sands

Reservoir petrophysical properties including relative permeability are influenced by stresses acting on the reservoir rock. Fluid injection or depletion operations cause a change in pore pressures (altering the rock stresses) that affect the permeability and relative permeability. Knowledge of state of stresses acting on the reservoir is essential to increase the recovery factor from the reservoir.

As discussed in previous sections permeability is affected by stresses acting on a porous media. Changes in absolute permeability also affect the relative permeability. The changes in single phase permeability are well documented as considerable research has been undertaken on the subject of stress sensitivity of permeability. Much less work has been done to analyze the stress sensitivity of relative permeability and the associated phase saturation changes.

Fatt (1952, 1953) was the first to study the effect of stress on the permeability and relative permeability. Experiments simulating overburden pressures of almost 3000 psi were done on consolidated sand stone cores. Gas-oil relative permeability was measured in his experiments. Results from his experiments indicated no significant effect of stress on the relative permeability. Wilson (1956) measured water-oil permeability using the steady state method on cemented sandstone cores. He compared the results from experiments done at 30 psi and 5000 psi overburden pressure and a maximum confining pressure of 5000 psi. Experimental data indicated that the change in effective permeability to oil was proportional to the change in single phase permeability.

Ali *et al.*, (1987) studied the change in relative permeability with changing overburden pressure on Berea Sandstone cores. The initial water saturation in his cores increased from 27% to 32% when overburden stress was increased from 1000 psi to 6000 psi. The increase in initial water saturation obtained after the oil flood was attributed to the increase in capillary forces due to decrease in pore sizes. Residual oil saturation also showed an increase with increasing overburden pressure (Figure 1.8). The increase in residual oil saturation was again attributed to the increased capillary pressure due to pore size reduction. Jones *et al.*, (2001) also observed an increase in S_{or} and a reduction in K_{ro} was observed with applied stress.

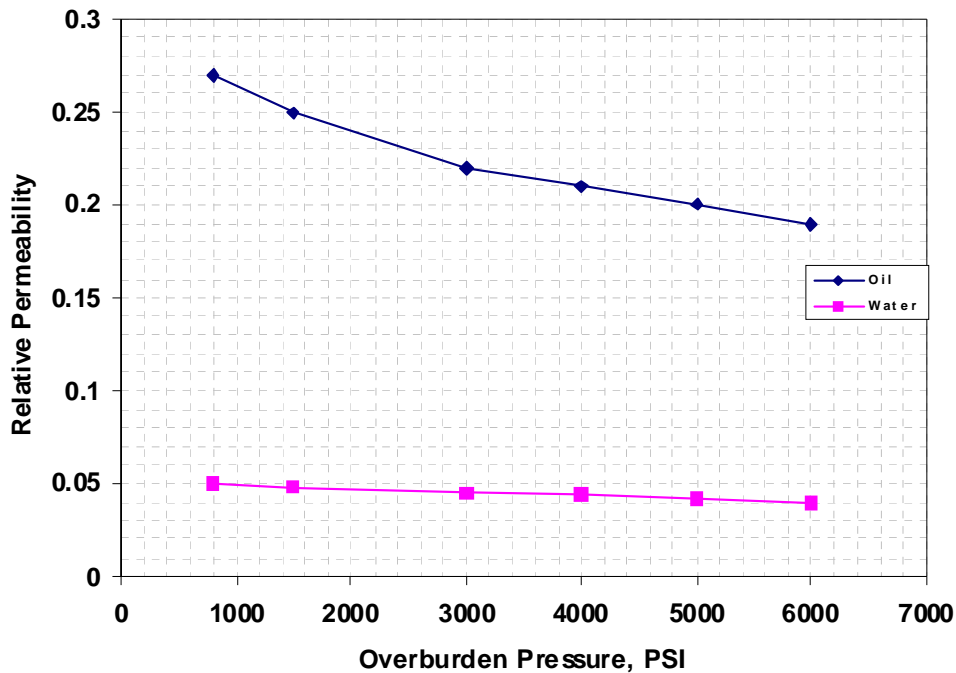


Figure 1.8: Change in relative permeability to oil and water with increasing overburden (from Ali *et al.*, 1987). Reduced relative permeability to oil and a slight decrease in relative permeability to water is observed.

Li (2006) described an improvement in effective permeability resulting from isotropic unloading and shear dilation. Wong *et al.*, (2001) showed that effective

permeability to water (in the presence of immobile bitumen) varies even more significantly than absolute permeability as stresses are imposed on the oil sands. During triaxial compression test, a 50 % increase in effective permeability to water was observed as the volumetric strain increased and the sample experienced dilation. However, he did not perform any two phase flow tests. Figure 1.9 shows the results of experiments done by Wong *et al.*, (2001).

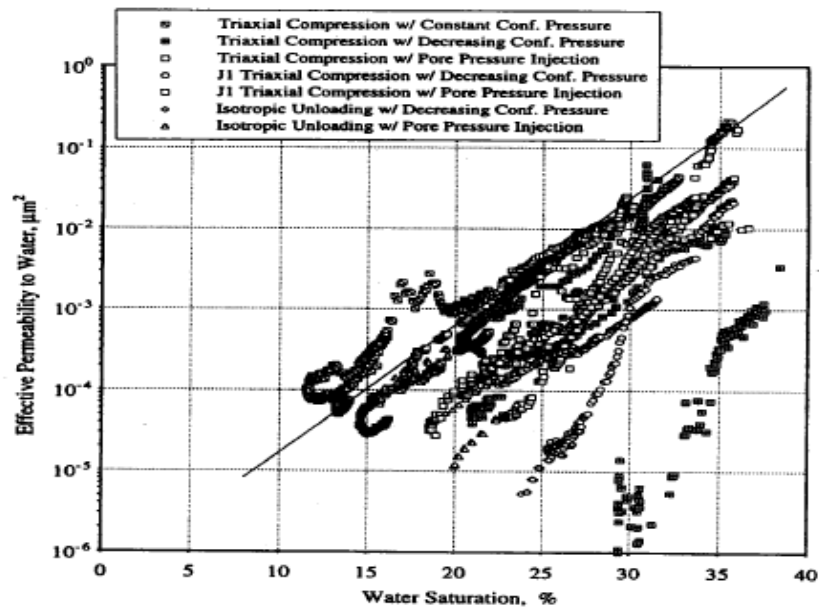


Figure 1.9: Effective permeability to water under isotropic unloading and triaxial compression. Increase in effective permeability is observed in all the tests (from Wong *et al.*, 2001).

Oldakowski (1994) conducted experiments to calculate the effective permeability to water in Athabasca oil sands (bitumen saturated sands) under isotropic unloading tests. He observed that the effective permeability increased up to 50% when the confining stress was reduced from 6 MPa (870 psi) to .1 MPa (14.5 psi). The porosity of his samples varied between 32% and 35%. During his tests he also observed an increase in

water saturation from 6.4% to 17.4 %. Triaxial tests showed initial compaction leading to decreased effective permeability to water, while 100-200% increases in effective permeability were observed due to dilation. But like others Oldakowski (1994) also did not conduct two phase relative permeability experiments.

1.7 RESEARCH OBJECTIVE

The aim of this work was to study the change in relative permeability to oil and water when the sand packs are loaded along paths most likely to be experienced in SAGD. Shear dilatancy in heavy oil reservoirs is thought to be the main cause of permeability enhancement. Since the effect of dilatancy on relative permeability to oil and water and residual oil saturation has not been studied in detail, an experimental study of changes in relative permeability to oil and water and residual oil saturation due to stress change on unconsolidated Ottawa sand was carried out.

A thorough understanding of how shear dilatancy affects the relative permeability to oil and water may lead to development of better simulation models that can reproduce the complex interaction between geomechanics and fluid flow in unconsolidated heavy oil sand reservoirs. A geomechanical model capable of coupling the change in relative permeability and residual oil saturation can lead to more realistic models that can help improve recovery factors from heavy oil reservoirs.

Sand samples made from three different kinds of sands were loaded following the paths of triaxial compression and radial extension. The relative permeability to oil and water and residual oil saturation in the sand packs were studied before and after the shear failure of the sand packs. The tests quantitatively helped identify the improvement or decrease in relative permeability in the sand packs due to compaction or dilation. The experiments also helped identify the trend of change for residual oil saturation during compaction and dilation of sand packs.

CHAPTER 2

Experimental Apparatus and Test Procedures

2.1 EXPERIMENTAL APPARATUS

The experimental setup for this investigation (Figure 2.1) consisted of a triaxial cell, a load frame, a vacuum pump, pressure transducers for measuring the pressure drop across the sample and a glass separator column used to inject oil into the sample. The confining pressure was controlled by a ISCO-1000D syringe pump which also provided for measurement of the specimen volume. Pore fluid was injected with an ISCO LC-5000 syringe pump. Load and displacement transducers were used for the measurement of axial load and displacement. A Labview data acquisition program recorded the analog signals.

2.1.1 Triaxial Cell

The triaxial cell (Figure 2.2) consisted of an outer cylinder and two 2 inch diameter axial loading pistons (rams). The base of the cell, outer cylinder and the top were made of aluminum. The top and bottom rams had conduits for the flow of fluids through the sample. The bottom piston fit into circular groove in the base of the cell, which had a hole for pore fluid flow. Porous plates in the top and bottom piston prevented fines migration from the sand sample. The permeable plates were 1 inch in diameter and had a permeability of 80 Darcy.

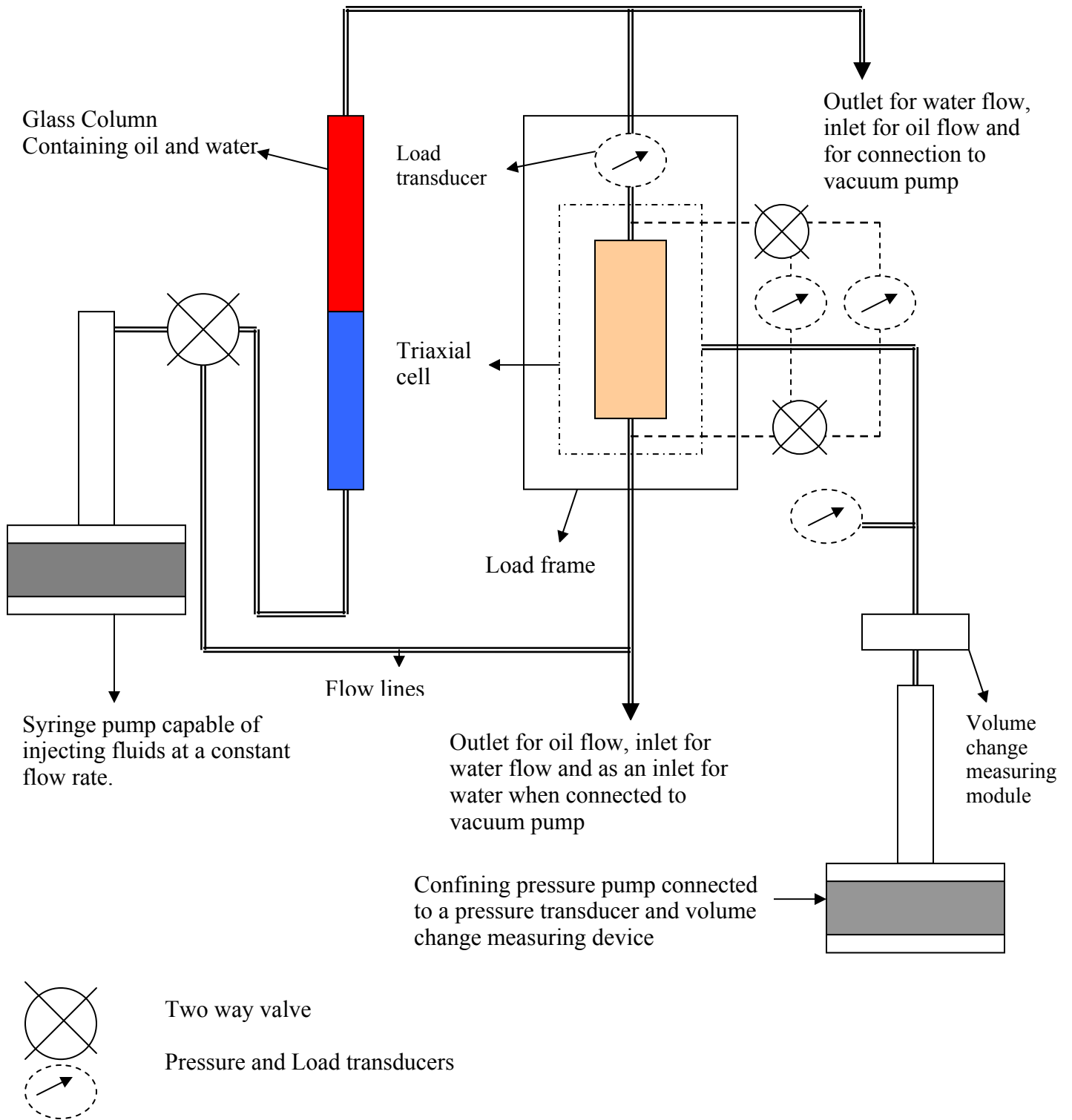


Figure 2.1: Schematic of the apparatus.

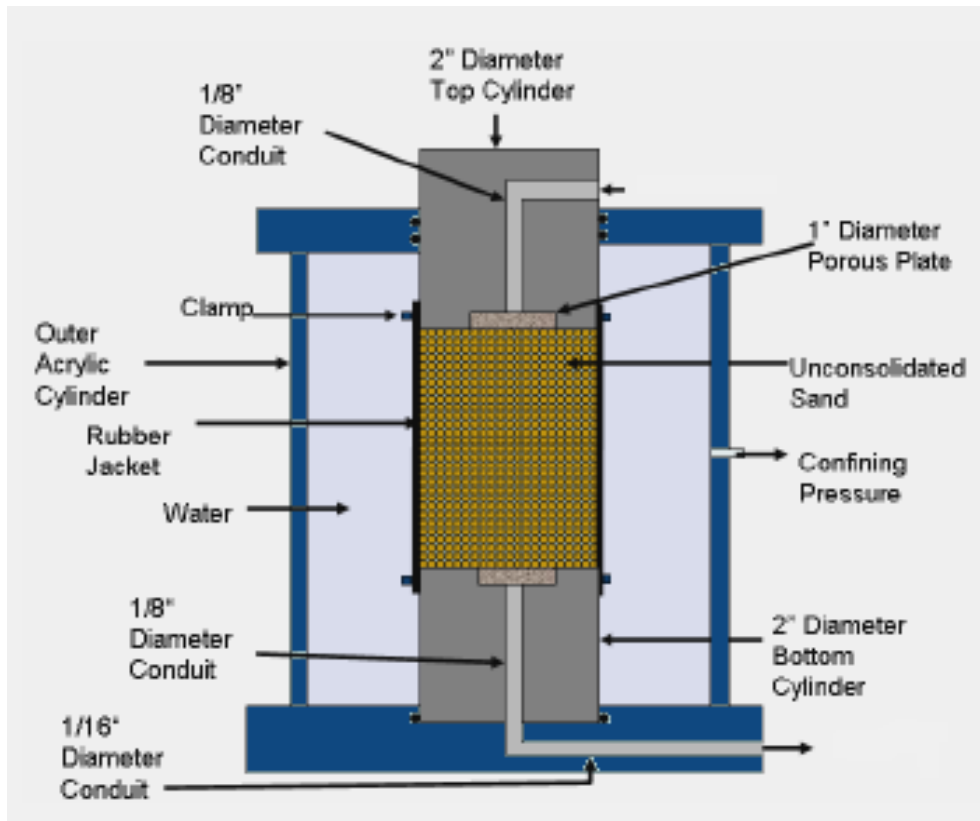


Figure 2.2: Triaxial cell.

2.1.2 Load Frame

The 10 Kpsi load frame (Figure 2.3) was a Humboldt model HM-3000. It consisted of a load motor, a linear displacement transducer, a 1000 psi pressure transducer and a load transducer. The load motor was servo-controlled using the National Instrument's LabVIEW software which also recorded all the data from transducers used in the experiment.

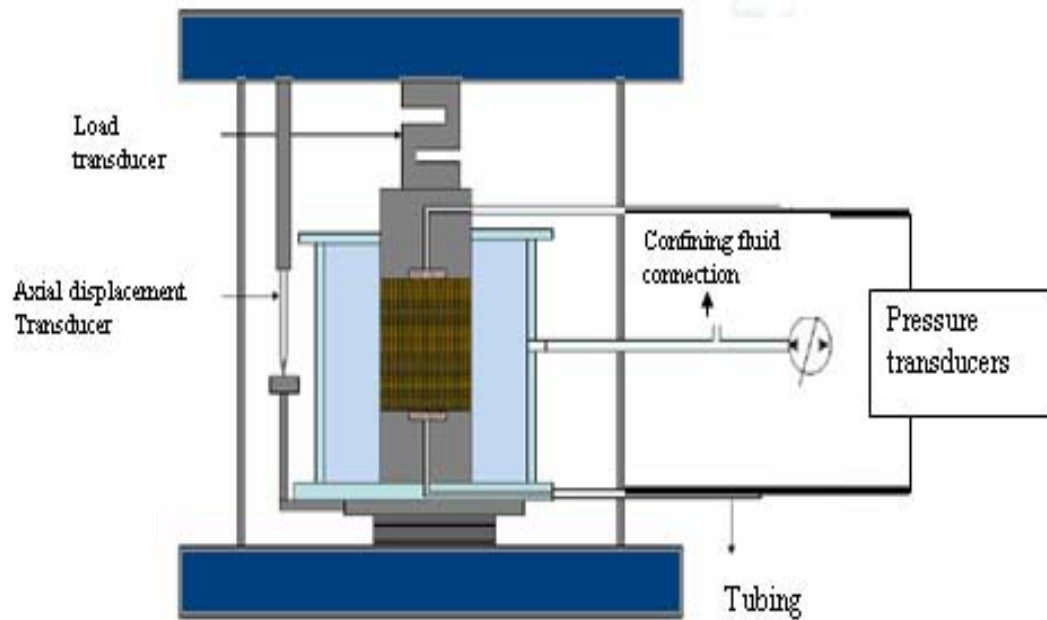


Figure 2.3: Load Frame.

2.1.3 Syringe Pumps and Glass Column

The ISCO-LC 1000 can pump fluid at a constant flow rate or at constant pressure. For applying the confining pressure the pump was operated in a constant pressure mode. The pump is also equipped with a 1000 ml fluid reservoir and is capable of recording the volume of the confining fluid expelled or injected into the triaxial cell. The values of the volume from the pump were fed directly to the LabVIEW program to determine the volumetric strain of the sample.

The pore fluid pump injected fluids at a constant flow rate. The maximum flow rate from this pump was 400 ml/hour. A two way valve at the pump outlet diverted the flow directly into the sample or into the separator column used for injecting oil into the sample. The water from the pump displaced the oil in the glass column, which then

flowed into the sample. The glass column had a capacity of 2000 ml and it was held in a vertical orientation by clamping to a ring stand. Figure 2.4 shows the arrangement used to inject oil in the sample.

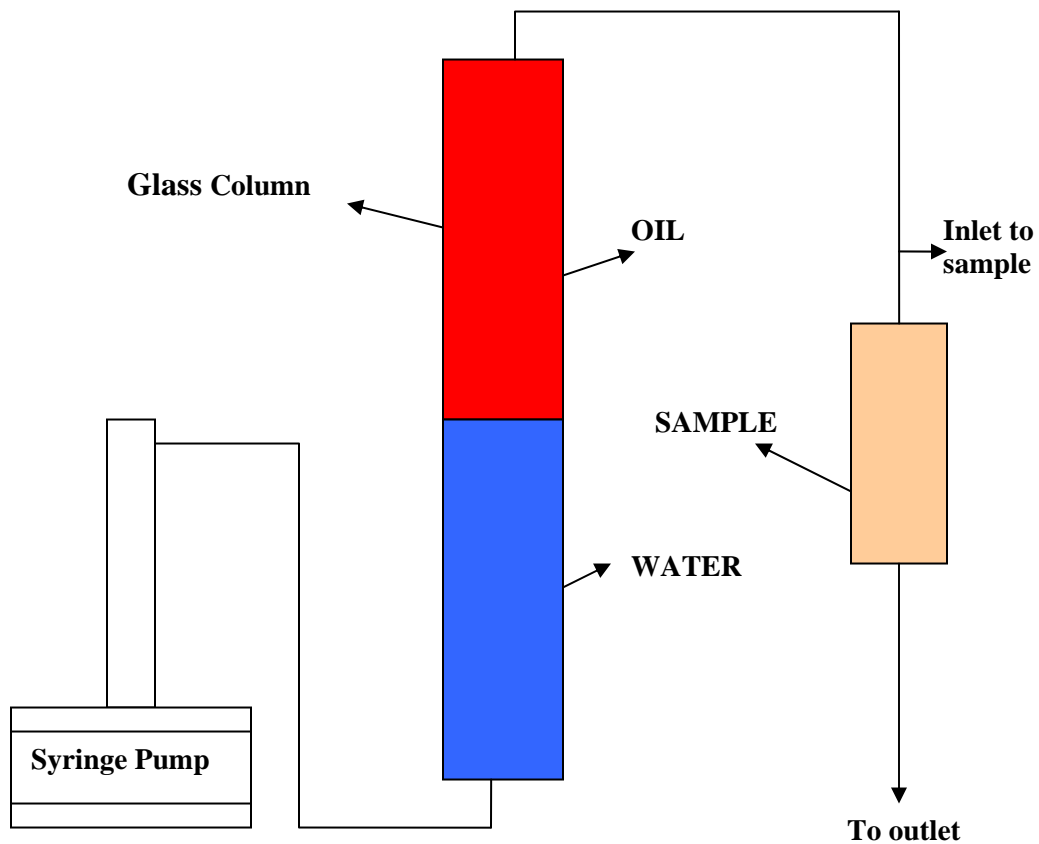


Figure 2.4: Arrangement for injecting Oil into the sample.

2.1.4 Vacuum Pump

A vacuum pump was used in the experimental setup to purge the sample of the air and achieve a uniform water saturation in the sample at the beginning of the experiment. The sample was usually vacuumed for 15 minutes and then the inlet was connected to a water reservoir.

2.1.5 Pressure Transducers

Two Validyne pressure transducers were used to measure the pressure drop across the sample. One transducer had a full scale range of 3.2 psi and was used to measure the small pressure in case of water flow. The other transducer had a maximum range of 50 psi and was used to measure the higher pressure drops for oil flow across the sample.

The transducers were calibrated and checked often with calibration equipment. The transducers were connected in a parallel arrangement with two way valves, which allowed the use of either of the pressure transducers during the experiment.

A bypass was also connected across the transducer to bleed the pressure or allow fluid flow while purging the system of air (Figure 2.5). At the start of each experimental run and while switching to another transducer, the transducer were zeroed by opening the by pass valve.

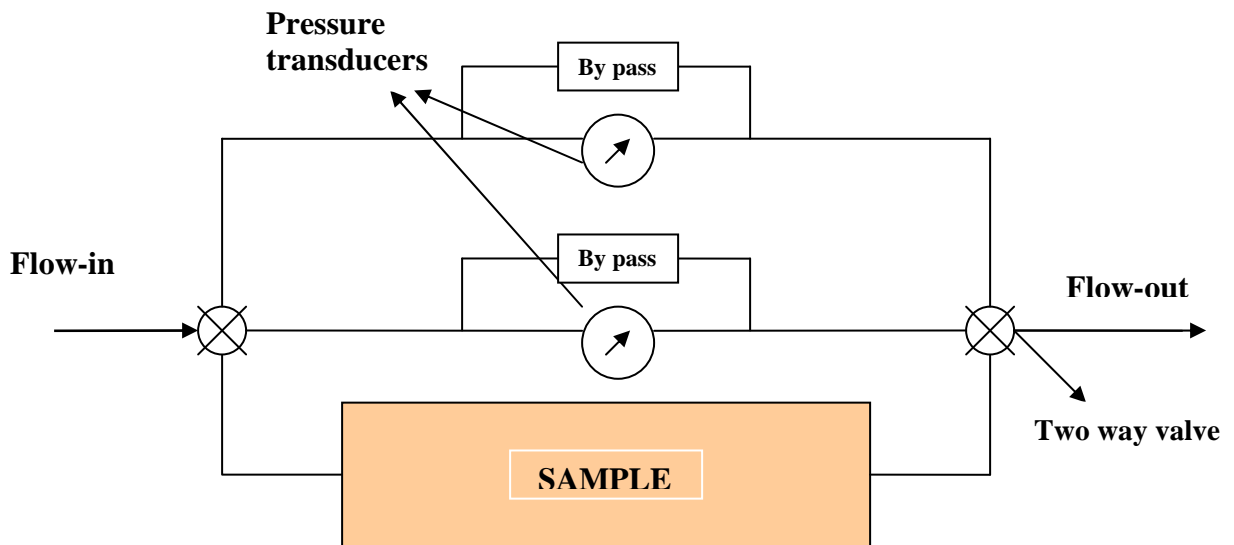


Figure 2.5: Arrangement of pressure transducers.

2.1.6 Mass Balance

A mass balance was used to measure the weight of the sand that was used to make the sample. The mass of the sand was later used to calculate the porosity of the sample.

2.1.7 Pore Fluids

Dow Corning 200 silicone oil (DC-200) and water were the two pore fluids used in the experiments. DC-200 had a dynamic viscosity of 50 cp and it also does not show any reactivity with the sand.

2.2 SAND PROPERTIES AND GRAIN SIZE DISTRIBUTION

Ottawa sand with two different grain size distributions were used to create the three sand samples used in the study (Figure 2.6). These sands are commercially available from U.S Silica, Ottawa, IL, with each of them well sorted and having a uniform grain size distribution. Sands F-35 (Medium Ottawa) and F-95 (Lower Fine Ottawa) were sub angular. The Medium Ottawa (MO) had a median grain size of approximately 400 microns while the Lower Fine Ottawa (LF) had a median grain diameter of a little over 100 microns. The Lower Amalgamated Ottawa (LA) was created by mixing 40% by weight Medium and 60% Lower Fine Ottawa and had a median grain size of about 260 microns (refer to Appendix A for detailed grain size analysis of sands). Figure 2.7 shows SEM images of the sands, indicating their relative grain diameter difference.

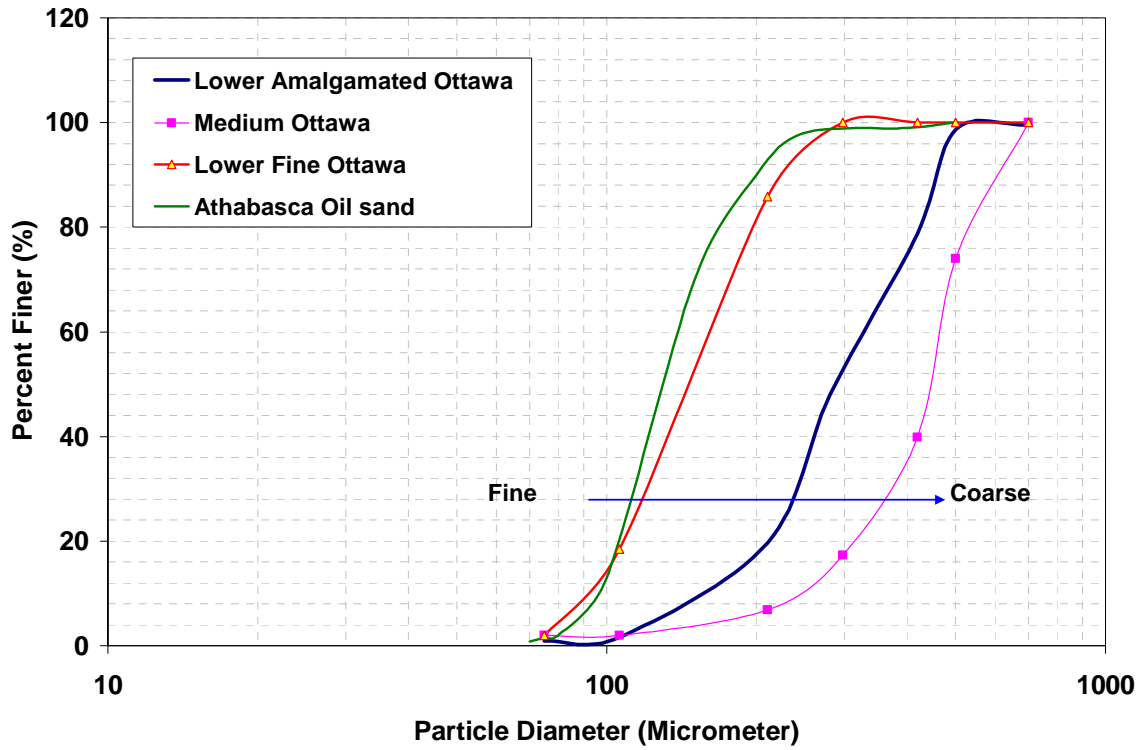


Figure 2.6: Grain size distribution of the sands used in the experiment. The coarsest sand is the Medium Ottawa while the finest is Lower Fine Ottawa. Athabasca oil sand has a grain size distribution similar to that of Lower Fine Ottawa (Yaich, 2008).

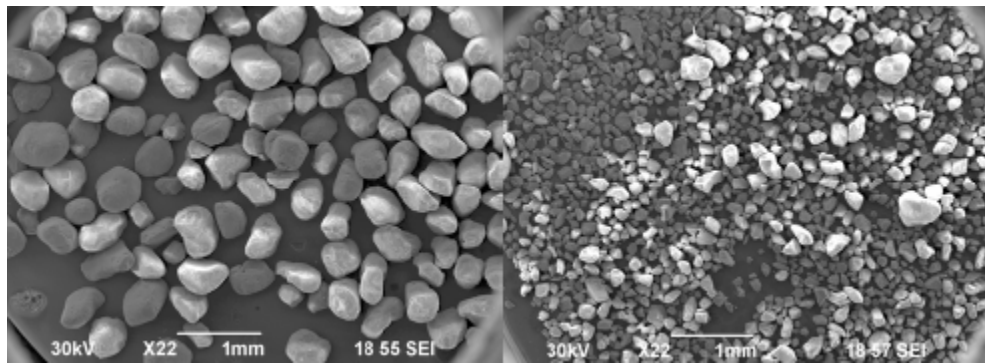


Figure 2.7: SEM images (from Yaich, 2008) of Medium Ottawa (Left) and Lower Fine (Right) Ottawa sand.

2.3 POROSITY MEASUREMENT

Porosity (ϕ) of the sand samples was determined as

$$\phi = \frac{V_b - V_g}{V_b} \quad (2.1)$$

where

V_b = bulk volume of the sample, and

V_g = grain volume of the sand in the sample.

The bulk volume of the sand sample was calculated from the dimensions of the sand pack as

$$V_b = \frac{\pi D^2 L}{4} \quad (2.2)$$

where

L = length of the sample, and

D = diameter of the sample.

The grain volume was determined as

$$V_g = \frac{\text{mass of sand}}{\text{density of sand}} \quad (2.3)$$

A quartz density of 2.65 grams/cc was used for the calculations.

2.4 PERMEABILITY MEASUREMENT

Permeability was estimated based on Darcy's law and the flow-pump method (Richardson *et al.*, 1952):

$$K = \frac{Q\mu L}{A\Delta P} \quad (2.4)$$

where

K= permeability of the sample,

A= area of the sample,

L= length of the sample,

ΔP = pressure drop across the sample,

μ = viscosity of the fluid flowing through the sample, and

Q= flow rate at the outlet of the sample.

The syringe pump was used to maintain a constant water flow rate, Q, through the sand sample before and during deformation. The pressure drop across the sample, ΔP , was measured by using either of the two pressure transducers connected across the sample. Before the start of the experiment the pressure transducers were zeroed by opening the bypass valves connected across each transducer. Finally, the bypass valve was closed to measure the pressure drop across the sample. The system was allowed to stabilize so that a steady reading of the pressure could be obtained. Corrections for back pressure were also made in the experiments. The pressure drop in the apparatus was also accounted for by running tests without a sample between the end platens. The end platens were assembled face to face with all the other fittings and tubings still connected. Water and oil were then flowed through the assembly to determine the pressure drop in the apparatus. The values of pressure drop obtained from the end platens test was subtracted from the values of pressure drop obtained in later tests in which a sand sample was present between the end platens.

The sample was isotropically loaded to the initial stress conditions by increasing the axial and confining pressure simultaneously. Tap water was used as the confining fluid throughout the course of the tests.

During deformation the cross sectional area and length of the sample changed. Since these parameters can affect the permeability calculation (Equation 2.5), length and area were updated throughout the experiment. Change in length of the sample is directly measured using displacement transducers attached to the loading ram. The new area of the sample was calculated as

$$A_{smp} = \frac{V_o(1 - \varepsilon_v)}{L_o(1 - \varepsilon_a)} \quad (2.5)$$

where

L_o = original length of the sample,

ε_a = axial strain,

ε_v = volumetric strain, and

V_o = original volume of the sample.

2.5 VOLUMETRIC STRAIN CALCULATIONS

The elastic definition of volumetric strain (ε_v) is the sum of volumetric (Equation 2.6) in the three principal directions, given by

$$\varepsilon_v = \varepsilon_{xx} + \varepsilon_{yy} + \varepsilon_{zz} \quad (2.6)$$

where

ε_{xx} = normal strain in the x-direction,

ε_{yy} = normal strain in the y-direction, and

ε_{zz} = normal strain in the z-direction.

The relation between volumetric strain and stress for an elastic material is given by

$$\varepsilon_v = \frac{(1-2\nu)}{E}(\sigma_{xx} + \sigma_{yy} + \sigma_{zz}) \quad (2.7)$$

where

E = Young's modulus,

ν = Poisson's ratio,

σ_{zz} = axial stress,

σ_{xx} = maximum horizontal stress, and

σ_{yy} = minimum horizontal stress.

For Cylindrical sand samples $\sigma_{xx} = \sigma_{yy} = \sigma_{confining}$, so equation 2.7 can be rewritten as

$$\varepsilon_v = \frac{(1-2\nu)}{E}(\sigma_{axial} + 2\sigma_{conf}) \quad (2.8)$$

The normal response for an elastic material under all-around compression is volume reduction. Dilatancy is a non elastic behavior caused by localized porosity increased caused by grain rearrangement and shear.

Volumetric strain was calculated by measuring the change in volume of the confining fluid in the triaxial cell. Yaich (2008) derived the equation for volumetric strain assuming that some of the volume will be displaced because of the top ram entering the cell, and some due to dilation of the sample itself as

$$\varepsilon_v = -\frac{V_{disp} - V_{in}}{V_{initial}} \quad (2.9)$$

where

V_{disp} = volume of fluid displaced from cell,

V_{in} = volume of ram that goes into the cell, and

$V_{initial}$ = initial volume of the sample.

The accuracy of the volumetric strain measurements was validated using an incompressible rubber samples at 50 psi confining pressure. Volumetric strains of less than .2% were observed at about a 20% axial strain.

Calculating the volumetric strain for the radial extension tests was more complicated than calculating the volumetric strain in triaxial compression tests. A change in confining fluid pressure in the radial extension tests lead to volume changes due to the water compressibility and confining chamber deformation. An aluminum sample of the same dimensions as the sand sample (3 inches in length and 2 inches in diameter) was used to determine the volume change due to the compressibility of the system when the confining pressure is changing. The sample was isotropically loaded to 200 psi. The axial stress was then kept constant while the radial stress is decreased to 0 psi. In the calibration tests the change in volume and radial stress showed a linear relationship down to a 40 psi. Below 40 psi the relation between volume change and confining pressure can be described as logarithmic (Figure 2.8). Thus the expression for volumetric strain was written as

$$\epsilon_v = -\frac{V_{disp} - V_{stress} - V_{in}}{V_{initial}} \quad (2.10)$$

where the additional term V_{stress} denotes the volume change due to the change in confining stress.

As pointed out by Yaich (2008) the volumetric change caused by deformation of the aluminum sample and compressibility of the water is small. The volumetric strain due to the change in confining stress in this investigation is much smaller in comparison to work of Elyas (2008) possibly because the triaxial cell made of polyarcylic was replaced with an aluminum one, a different set of O rings were used and the possibility of air bubbles being present in the confining fluid (water).

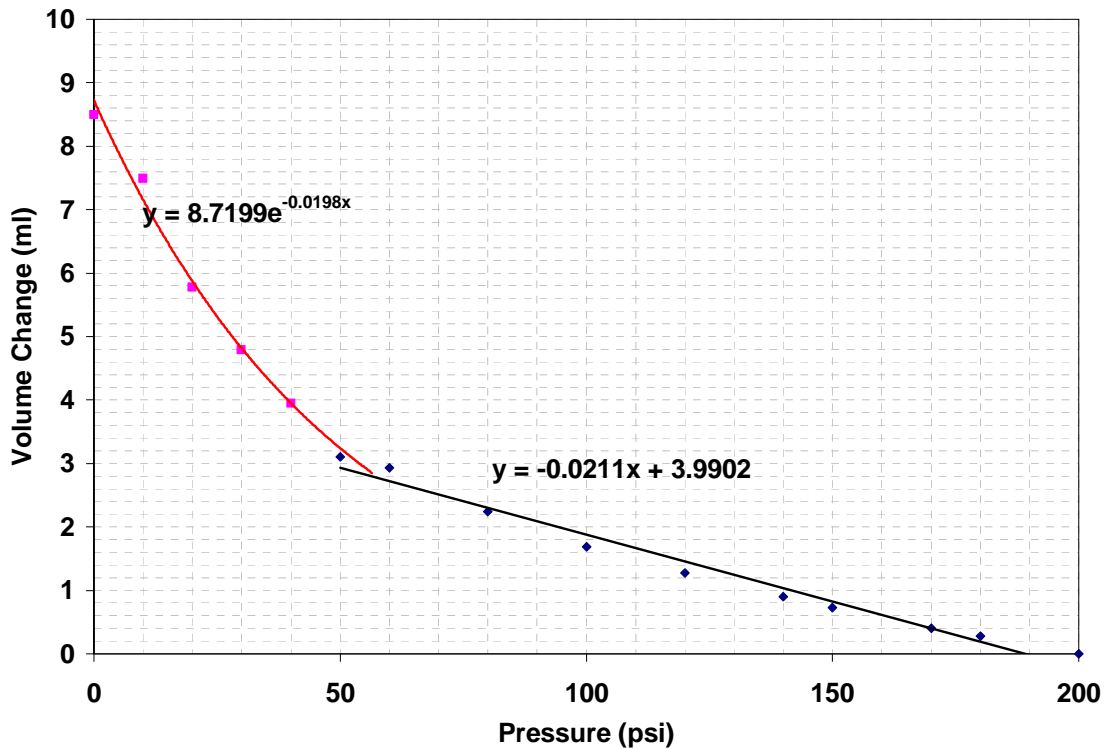


Figure 2.8: Volume change due to decreasing confining pressure for an aluminum sample initially loaded isotropically to 200 psi.

2.6 SAMPLE PERMEABILITY AND ITS RELATION TO GRAIN SIZE

The sand packs created for investigation had initial permeabilities that were strongly dependent on the grain size. Samples made from Lower Fine Ottawa (201 micron mean grain diameter) had the lowest permeability (7 Darcy), Medium Ottawa (435 micron mean grain diameter) had the highest permeability (35 Darcy) and Lower Amalgamated Ottawa (300 micron mean grain diameter) had an intermediate permeability (20 Darcy) (Figure 2.9). Figure 2.10 shows that initial porosity did not control the initial permeability.

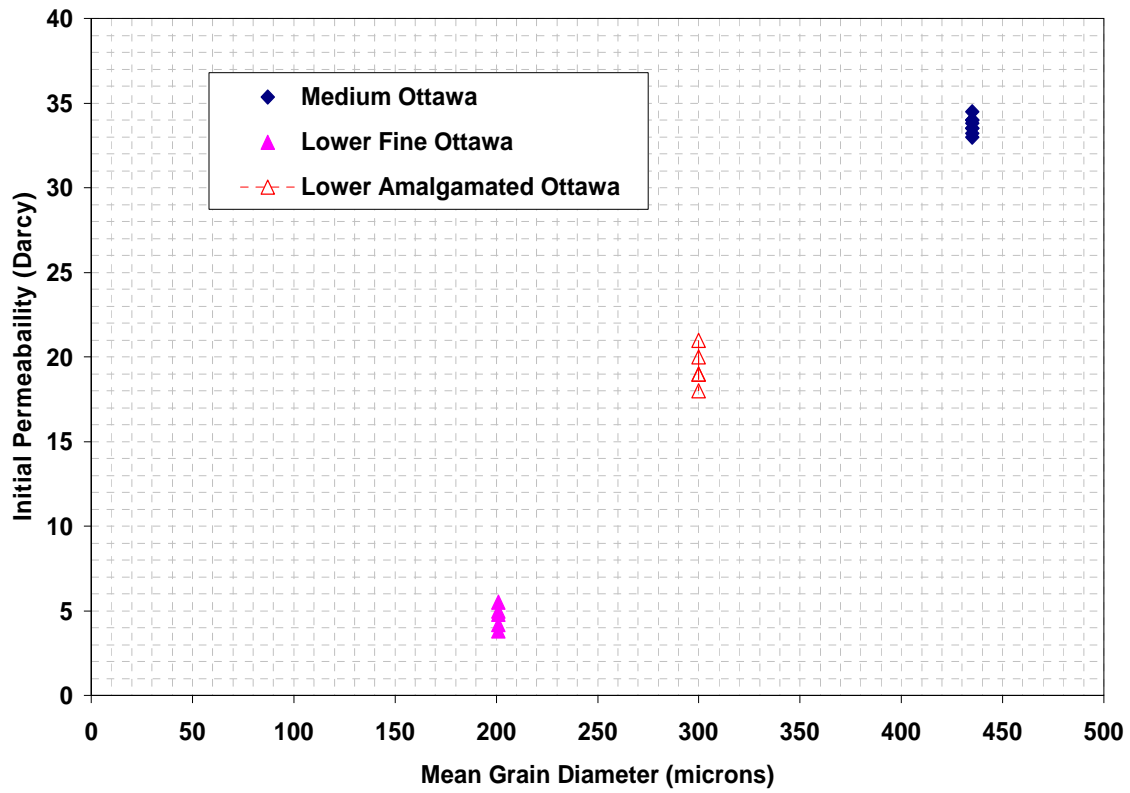


Figure 2.9: Initial permeability as a function of mean grain size diameter. Mean grain diameter determines the permeability of the sand sample.

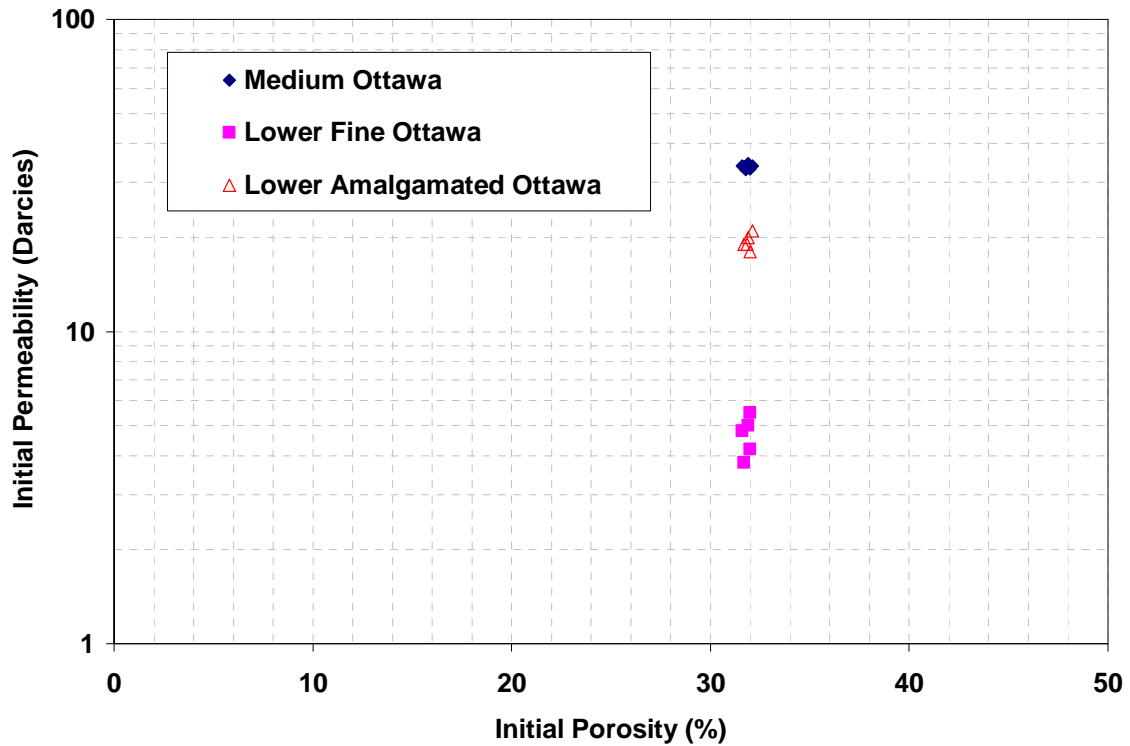


Figure 2.10: Initial porosity versus permeability.

The Kozeny-Carman equation (Carman, 1937) usually provides a good estimate of permeability in porous material. Kozeny-Carman introduced the notion of hydraulic radius along with porosity in their equation. They also considered the effect of flow tortuosity on the permeability but stated that porosity remained to be one of the influential factors in determining the permeability of unconsolidated sands. The basic form of Kozeny-Carman equation is

$$k = \frac{d^2 \phi^3}{36 \gamma \tau (1 - \phi^2)} \quad (2.11)$$

where

k = permeability,

d = diameter of the sand grains,

ϕ = porosity of the sample, and

$\gamma \tau$ = shape and tortuosity factor.

The value of $\gamma \tau$ is usually taken to be 5 for unconsolidated sands having uniform spherical particles. However, in order to obtain a reasonable fit (best fit) to the measured permeability values, the value of $\gamma \tau$ needs to be estimated using trial and error until the best fit is achieved. In this case a value of $\gamma \tau = 9.75$ was used to obtain a good fit for the measured values for permeability (Figure 2.11).

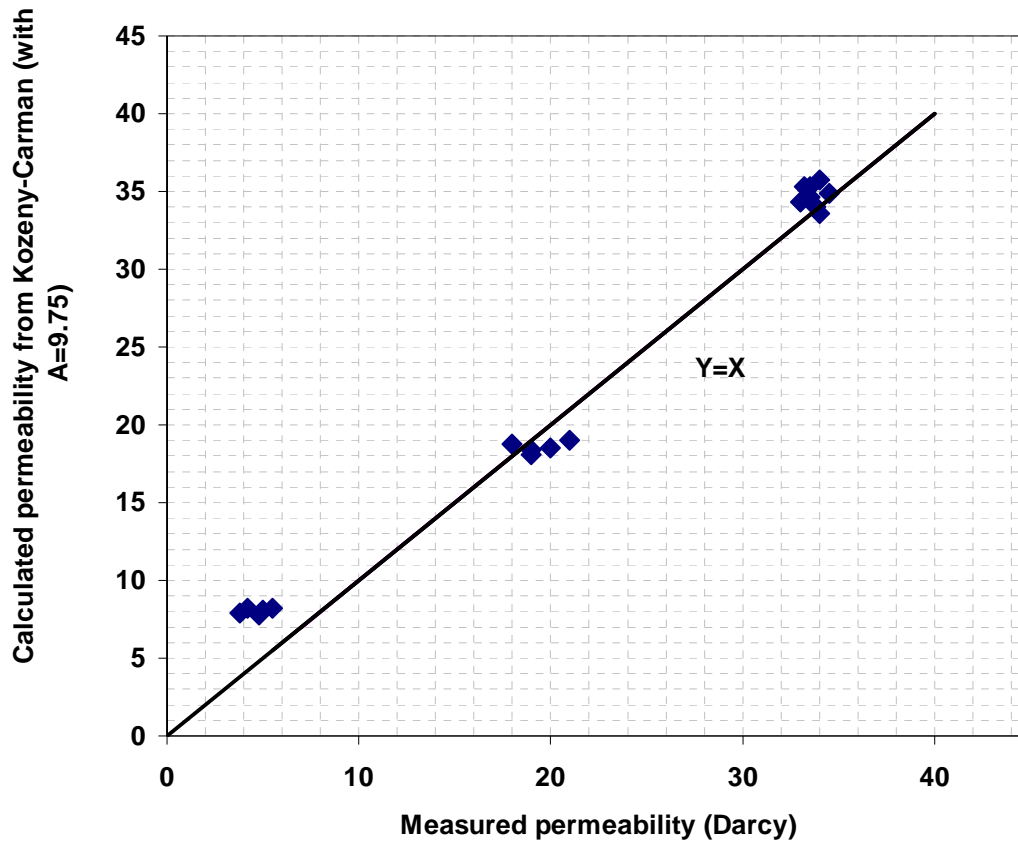


Figure 2.11: Calculated versus measured initial permeability with $A=9.75$ (Kozeny-Carman equation). The black line represents the line $Y=X$ in the graph.

2.7 PROCEDURES

2.7.1 Sample Preparation

The techniques commonly employed to make a sand specimen are wet tamping, dry tamping, water pluviation, wet vibration and slurry deposition (Yaich, 2008). Uniformity of a sand specimen is related to the repeatability of the test, which is an important factor in this investigation. As the method of sample preparation dictates the void ratio of the sample, pore volume and ultimately the strength of the sample. Sample

preparation method effects can be considered a kind of stress history. Therefore, using techniques that involve considerable human activity or effort to make the sample might cause considerable experimental error. Human error in sample preparation might cause non-uniformity to be introduced in the samples which will affect experimental results.

Based on the results of Oldakowski (1994), Tohidi-Baghini (1998) and Yaich (2008), wet vibration was chosen as the method of sample preparation in this investigation. A rubber jacket was securely fastened to the bottom ram using a hose clamp and the assembly was placed on the vibrating table. With the vibrating table switched on, water was poured into the jacket and sand was poured into the jacket until the sand layer was approximately 1/2 inches thick. The sample was left to vibrate for 3-5 minutes on the vibrating table after which a new layer of sand was later poured into the jacket. To make sure that the sand was completely immersed in water, a small layer of water was maintained on top of the sand surface. The process was repeated until the sample length was 3 inches. It took approximately 30 minutes to make a sample three inches in length and two inches in diameter. The samples made by wet vibration had narrow ranges of initial porosities (Figure 2.12). It is apparent that the porosity was not significantly affected by the mean grain size.

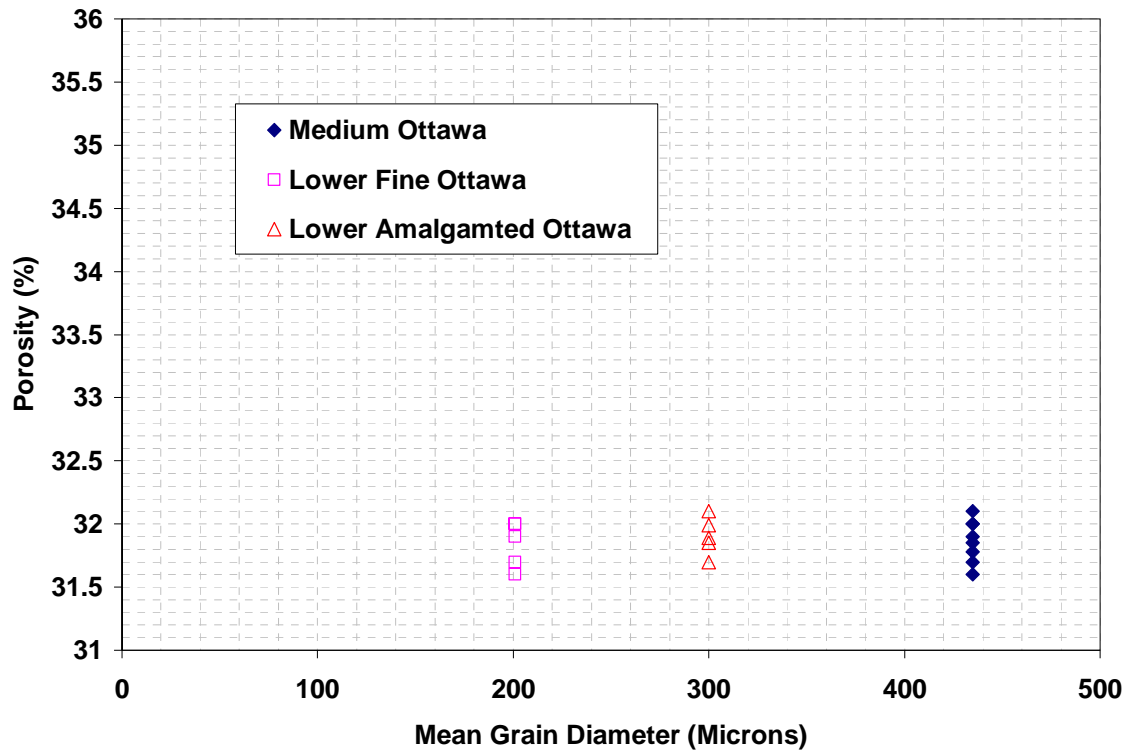


Figure 2.12: Porosity values obtained by wet vibration. Uniform porosities can be obtained by using wet vibration.

2.7.2 Sample Saturation

After the sample was made, the top ram was inserted into the rubber jacket and a hose clamp was tightened around the ram to prevent confining fluid from leaking into the sample. The triaxial cell was then assembled, the pore fluid outlet (Figure 2.9) was connected to the vacuum pump and the inlet sealed to evacuate the air from the sample. The vacuum was applied for 10 to 15 minutes, after which the inlet was connected to a water reservoir. The water was sucked through the water reservoir and flowed through the sample still connected to the vacuum pump. The vacuum was later disconnected with the inlet still attached to the water reservoir.

2.7.3 End Point Permeability and Relative Permeability (oil)

Water saturated sand samples were deformed to a specific value of axial strain and were then flooded with oil. The oil flooding was continued until all the mobile water had been flushed out of the sand sample. The residual water saturation remaining in the sample represents the initial water saturation (S_{wi}). The steady state S_{wi} is assumed to be achieved when 99% of the effluent from the sample is oil. Darcy's law was used to calculate the effective permeability to the oil phase at steady state has been achieved

$$K_o = \frac{Q_o \mu_o L}{A \Delta P} \quad (2.12)$$

where

K_o = oil permeability,

μ_o = oil viscosity,

Q_o = oil flow rate,

ΔP = pressure drop (steady state), and

A = cross sectional area of the sample.

The relative permeability to oil is found by normalizing K_o by the absolute permeability, K (Johnson *et al.*, 1959) as

$$K_{ro} = \frac{K_o}{K} \quad (2.13)$$

Where

K_{ro} = relative permeability to oil.

2.7.4 End Point Permeability and Relative Permeability (water)

After reaching steady state flooding the sample with oil, the sample is flooded with water until a steady state is again achieved (99% of the effluent is water). The end point water permeability can be calculated as

$$K_w = \frac{Q_w \mu_w L}{A \Delta P} \quad (2.14)$$

where

K_w = water permeability,

μ_w = water viscosity,

Q_w = water flow rate,

ΔP = pressure drop (steady state), and

A = cross sectional area of the sample.

The relative permeability to oil is found by normalizing K_w by the absolute permeability, K (Johnson *et al.*, 1959) as

$$K_{rw} = \frac{K_w}{K} \quad (2.15)$$

K_{rw} = relative permeability to oil.

2.7.5 Phase Saturations

Phase saturation at the end of a flood can be calculated by doing a mass balance. The volume of water recovered during an oil flood represents the volume of oil that was injected into the pore space of the sample. Subsequently the volume of oil recovered during a water flood along with the initial water saturation represented the volume of water that now occupies the pore space in the sample. The pore volume of the sample is

the product of specimen bulk volume and porosity. The initial water saturation (S_{wi}) is thus calculated as

$$S_{wi} = 1 - \frac{V_w}{V_p} \quad (2.16)$$

And the residual oil saturation (S_{or}) is given by

$$S_{or} = \frac{V_w - V_o}{V_p} \quad (2.17)$$

where

V_p = pore volume,

V_w = volume of water collected during oil flood, and

V_o = volume of oil collected during water flood.

For determining the phase saturations accurately the dead volume of the apparatus was subtracted from the volume of oil and water collected (Table 2.1).

Conduit Dimension		Volume (cm ³)
Diameter (inches)	Length (cm)	-
1/8	20.5	10.7
1/16	7	.8
Tubing	9.54	3

Table 2.1: Dead volume of the apparatus.

CHAPTER 3

Results and Discussion

Using the procedures described in chapter 2, deformation induced permeability and relative permeability changes were assessed for forty different sand samples using triaxial compression and radial extension stress paths. In the triaxial compression tests (50 psi confining stress) the sands showed an initial decrease in absolute and relative permeability as the sample compacted, after which there was an increase in absolute and relative permeability as the sample dilated during failure. Radial extension tests (200 psi constant axial stress) showed a greater enhancement in permeability values than the triaxial compression tests as these tests were dilatant from the very beginning of the deformation. Compaction during the triaxial tests showed an increase in residual oil saturation while dilation caused the residual oil saturation to decrease.

CT scans of the failed sand packs indicated that deformation caused localized shear bands of higher porosity that are probably the conduits for enhanced flow (increased absolute permeability) in the experiments.

3.1 TRIAXIAL COMPRESSION TESTS

3.1.1 Stress-Strain Behavior

Representative stress-strain curves for the triaxial tests at 50 psi confining stress are shown in Figure 3.1 for each sand type. A complete set of figures documenting all tests used in the study can be found in Appendix B (Figure B1, B2 and B3). The stress-strain curves in Figure 3.1 show a roughly linear initial stress-strain behavior followed by plastic yielding with strain softening after the peak stress. The cross-sectional area of the samples changed during deformation because of the high strains achieved. Stress values

were corrected for this area change, without which the stress-strain curves would show strain hardening.

The Lower Fine Ottawa samples showed a higher value of peak stress (230 psi) as compared to Lower Amalgamated Ottawa (200 psi) and Medium Ottawa (185 psi) samples. The post failure stress drop can be attributed to the development of shear bands causing the weakening of the sample. According to Desrues and Viggiani (2004), shear banding responsible for dilatancy usually starts at or before peak stress. Continuing deformation after failure encourages further growth of shear bands across the sample (CT images of failed sand packs in later section of this chapter show the pattern of shear bands developed). These deformation bands represent a common type of strain localization in unconsolidated sands are referred to as deformation bands (Fossen et al, 2007). Deformation bands are usually millimeters thick tabular zones of localized shear strain.

The stress-strain behavior of the samples with 200 psi confining stress was similar to the samples tested at 50 psi confining pressure. Initially an increase in differential stress was seen followed by a pressure drop due to failure of the sample (Figure 3.2). However, the Lower Fine Ottawa samples at 200 psi confining pressure had a much higher strength (720 psi peak stress) as compared to samples at 50 psi confining pressure (230 psi peak stress).

Lower Fine Ottawa, Lower Amalgamated Ottawa and Medium Ottawa had loading Young's Moduli values (calculated from the slope of the stress-strain curves) of 16000 psi, 14000 psi and 10000 psi, respectively, for triaxial compression tests with 50 psi confining stress, indicating a correlation between finer grain size and higher stiffness. Lower Fine Ottawa specimens in triaxial compression with 200 psi confining stress had a Young's modulus of 23000 psi as compared to 16000 psi, demonstrating the increase in

sample stiffness with confining stress. Ozgurel et al. (2005) and Ata et al. (1999) observed a similar trend of increasing stiffness and strength with decreasing grain size.

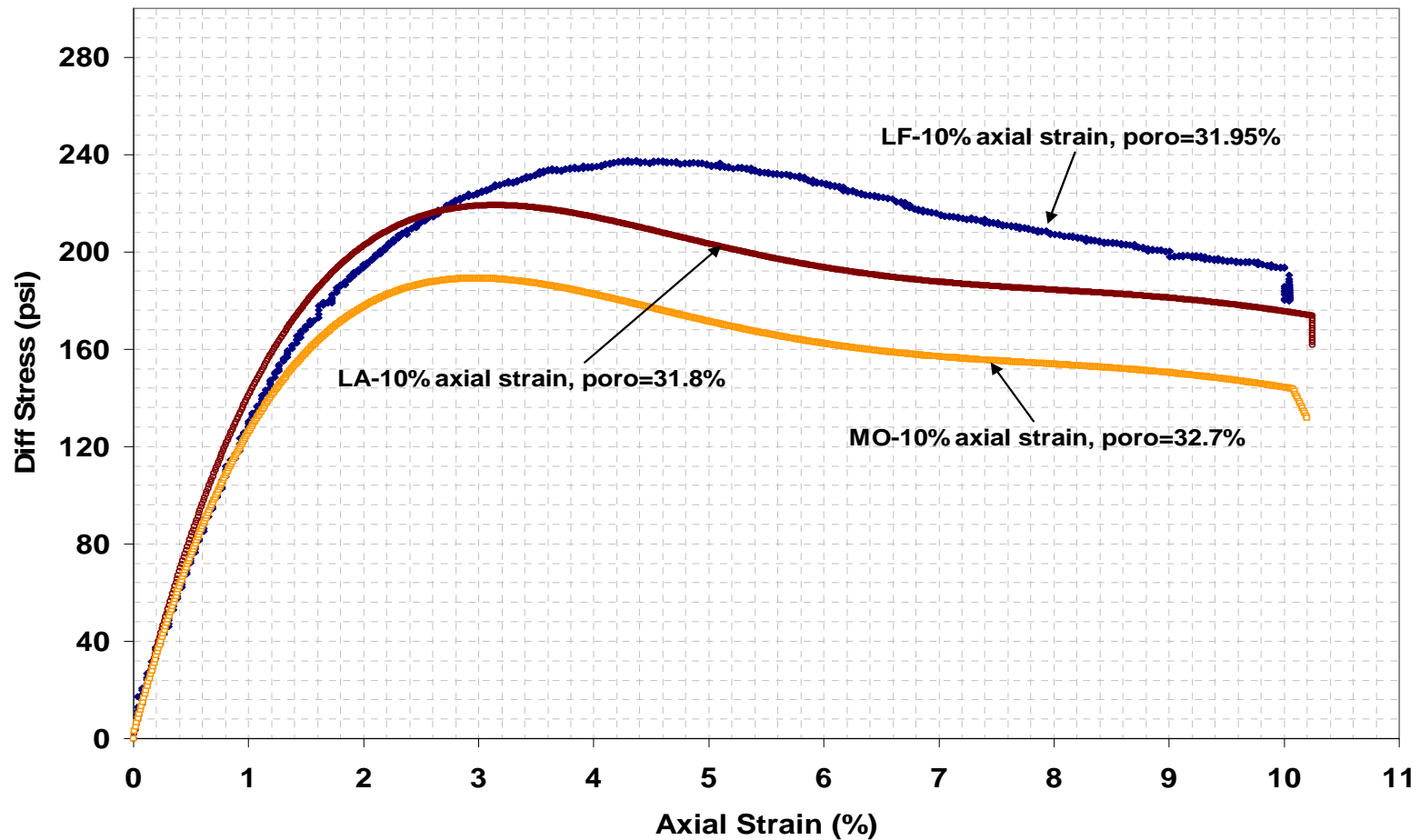


Figure 3.1: Stress strain curves in triaxial compression for the sand samples tested with 50 psi confining stress (LF-Lower Fine Ottawa, LA-Lower Amalgamated Ottawa, MO-Medium Ottawa).

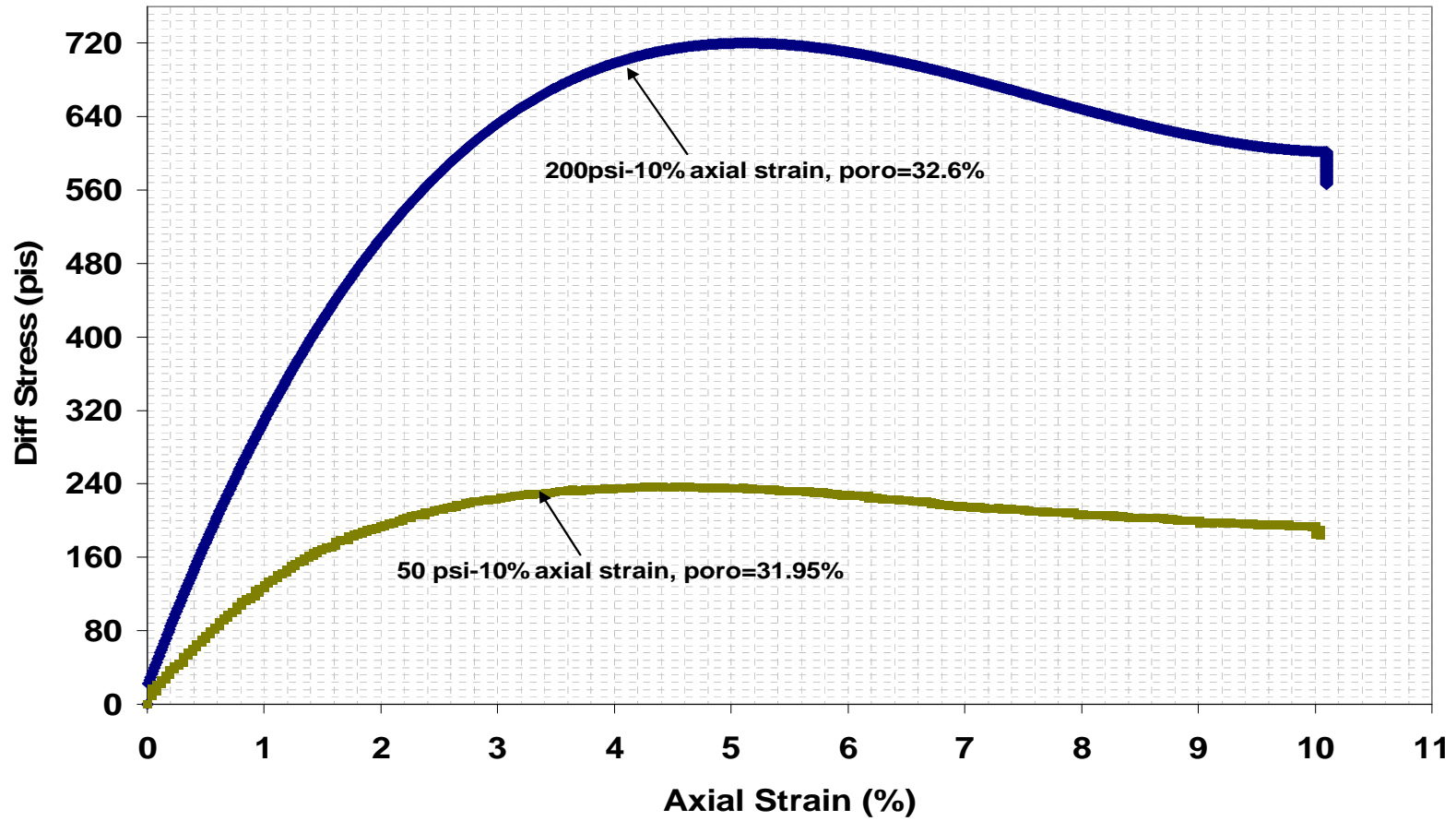


Figure 3.2: Stress strain curves in triaxial compression for the Lower Fine Ottawa samples tested with constant 50 and 200 psi confining stress.

3.1.2 Volumetric Strain

Volumetric strain measurements at 50 psi confining stress showed a limited compaction followed by dilation. Figure 3.3 shows the volumetric strain behavior with changing axial strain. A positive value of volumetric strain indicates compaction while a negative value of volumetric strain denotes dilation.

Volumetric strain in triaxial compression tests can also be explained in terms of the mean and deviatoric stresses on the sample. Increasing mean effective stress at the start of the tests caused the sample to compact initially. As the axial load and deviatoric stress on the specimen increased, shear distortion of the sample caused dilation and an increase in volume of the specimen.

The volumetric strain for Lower Fine Ottawa had a maximum value of 5.5% at 10 % axial strain. However, the volumetric strain of Lower Amalgamated Ottawa and Medium Ottawa (3.5% at 10% axial strain) was less as compared to the Lower Fine Ottawa specimens which showed a higher tendency for dilation, but the volumetric strain at 10% axial strain for Medium Ottawa and Lower Amalgamated Ottawa samples had similar values. The humps in the volumetric strain curve are due to the constant volume change in the triaxial cell. The confining pressure pump injected or withdrew water continuously (every few seconds) from the triaxial cell to maintain constant confining pressure during the experiment. The injected volume was some times more than required to maintain the desired value of confining pressure, which is then immediately withdrawn by the pump. For volumetric strain curves covering all the experiments used in this study, refer to Appendix B (Figure B4, B5 and B6).

Yaich (2008) found porosity to influence the volumetric strain measurements. In his investigation, higher porosity samples showed a more compactive behavior as compared to lower porosity samples. Samples used in this investigation all had similar porosities (31.6 and 32.5%) so porosity was not investigated with regard to its influence on deformation. However, it was observed that increasing the confining stress to 200 psi increased the peak compactive volumetric strain delayed diatancy to almost 5% axial strain (Figure 3.3).

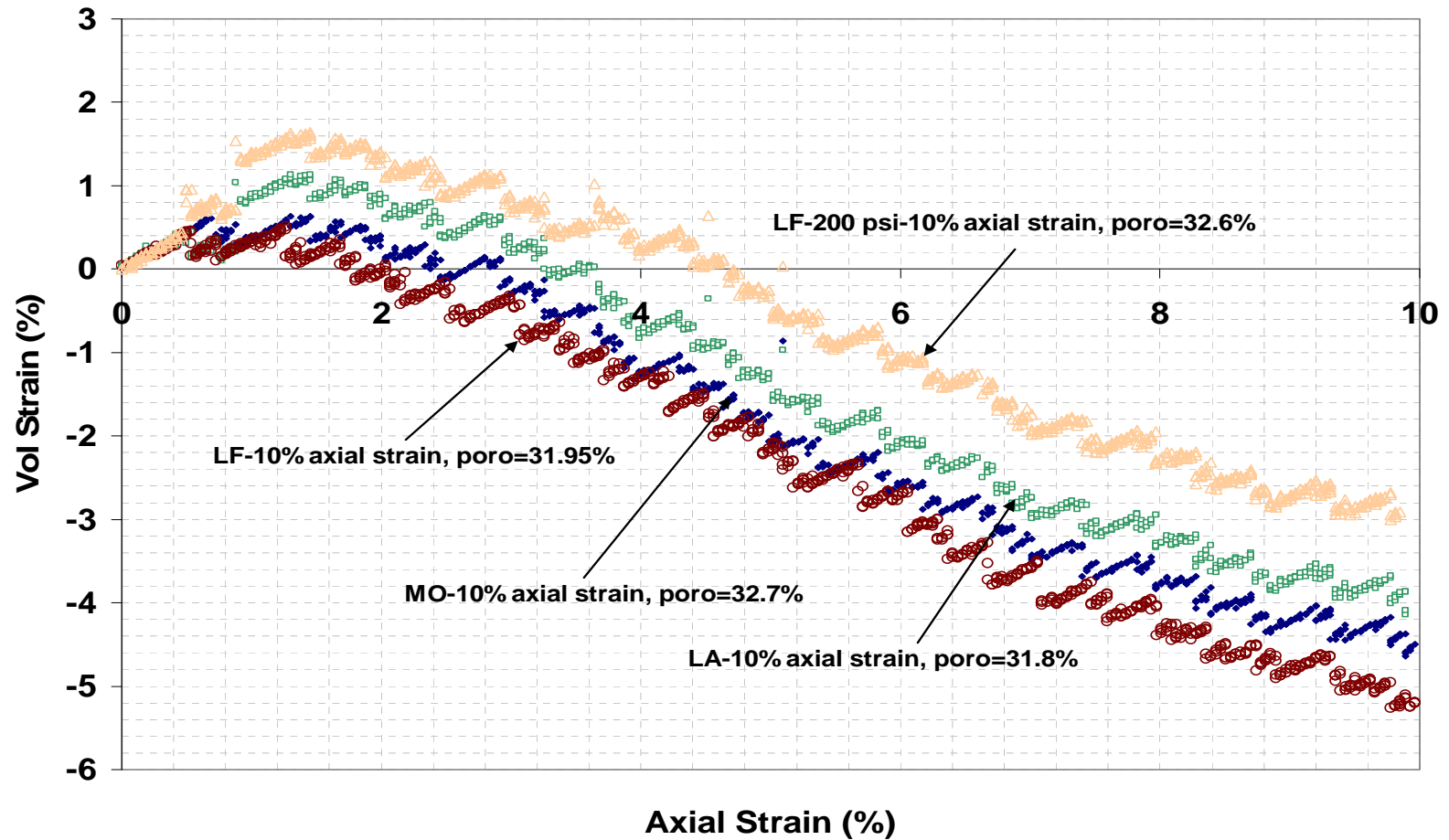


Figure 3.3: Volumetric strain for triaxial compression tests done with 50 psi confining pressure (LF-Lower Fine Ottawa, LA-Lower Amalgamated Ottawa, MO-Medium Ottawa).

3.1.3 Absolute Permeability

Absolute permeability measurements were made at 0%, 1%, 2%, 3%, 5%, and 10% axial strain for all sand types (Table 3.1 and Figure 3.4). A different sample was used for each axial strain value – no repeat flow measurements were made using the same sample but at different axial strain. For the 50 psi confining cases, the permeability decreased up to about 3% axial strain. At higher axial strain, when the sample experienced dilatant volumetric strain, the permeability increased. When looking at normalized permeability change (Figure 3.5), all sand types followed very similar behavior. Compaction caused a maximum reduction in permeability of about 25% at 2% axial strain, and the permeability rose to as much as 10% greater than the original value by 10% axial strain. The increase in permeability can be related to the onset of dilatancy. The formation of shear bands and the rearrangement of sand grains lead to an increase in pore throat size and an enhancement of the interconnectivity of pores. Raising the confining stress to 200 psi completely suppressed permeability enhancement seen in the 50 psi confining cases, such that at 10% axial strain, the higher confining stress case was at 30% overall permeability reduction. Higher confining stress is indicative of higher burial depths, suggesting there exists a depth limit below which shear dilation will not enhance permeability. However, it should be noted that the only permeability assessed in this study was the axial permeability. Lateral (or radial) permeability could show a different behavior.

Sand Type	Lower Fine Ottawa		Lower Amalgamated Ottawa		Medium Ottawa		Lower Fine Ottawa (200 psi confining stress)		
	Strain (%)	Porosity (%)	Permeability (D)	Porosity (%)	Permeability (D)	Porosity (%)	Permeability (D)	Porosity (%)	Permeability (D)
0		32.04	6.2	31.7	20	32.57	35	32.6	4.2
1		31.8	5.5	31.8	18	32.4	32.4	–	–
2		32	4.6	32.3	16.5	32.1	30	32.2	3.5
3		32.3	4.85	32.2	15.2	32.235	27.5	–	–
5		32.1	6.3	32.6	21.5	31.5	36	32.35	3.1
10		31.95	7	31.8	22.9	32.7	38	32.5	2.9

Table 3.1: Initial porosity and permeability of the different sand samples during triaxial compression with 50 and 200 psi constant confining stress and increasing values of axial strain.

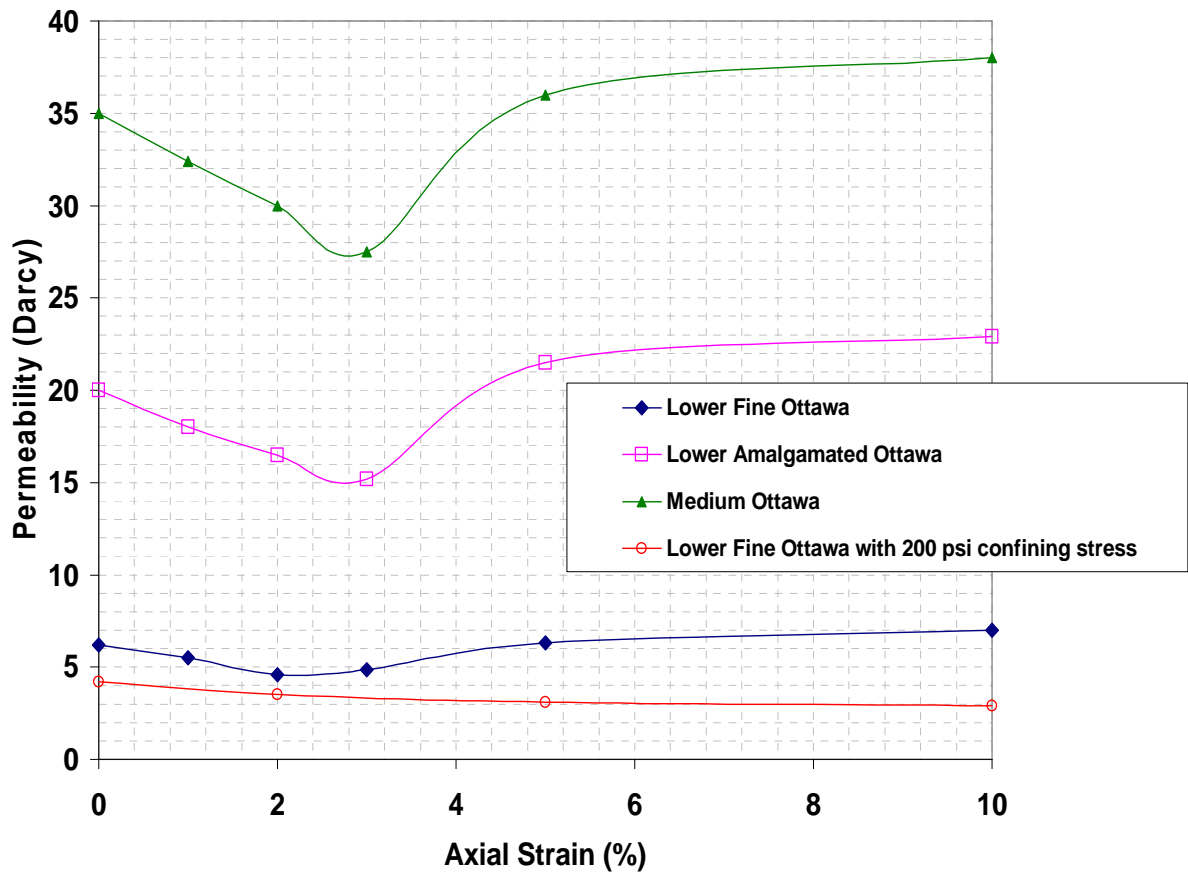


Figure 3.4: Permeability of sand samples in triaxial compression with 50 and 200 psi confining stress.

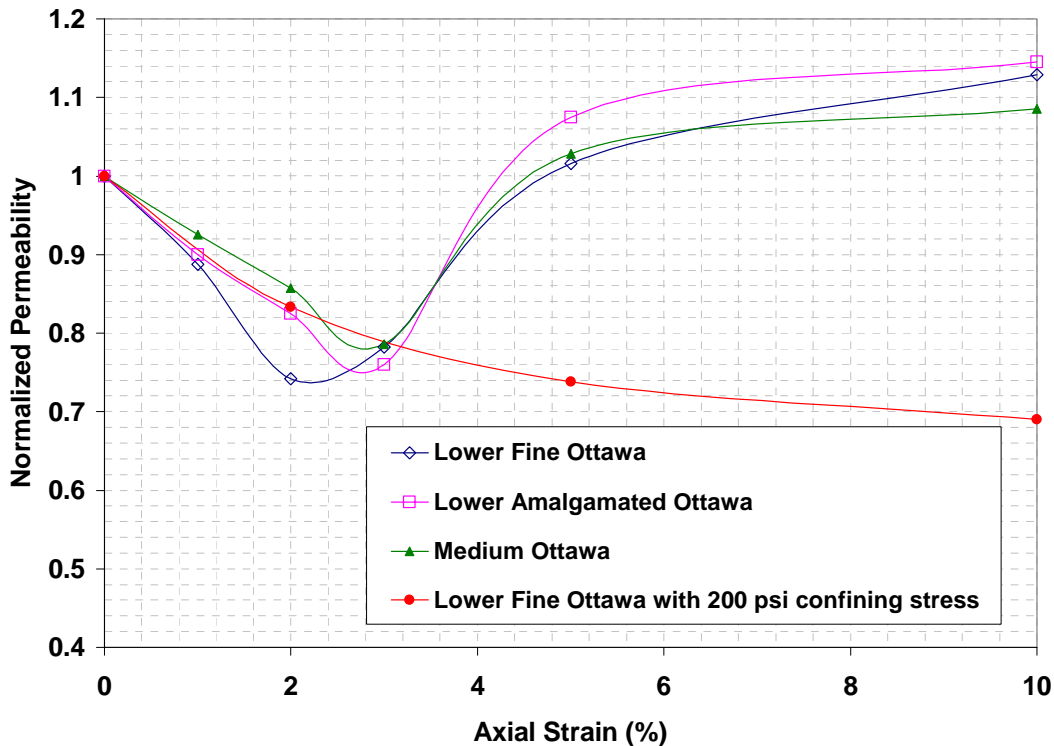


Figure 3.5: Normalized permeability of sand samples in triaxial compression with 50 and 200 psi confining stress.

3.1.4 Relative Permeability

The trend followed by relative permeability was similar to that of absolute permeability of the samples (decreasing relative permeability during the initial compaction and increase during post-failure dilation), but the magnitude of the variations was greater for the relative permeabilities. Measurements of end point K_{ro} and K_{rw} were carried out at initial water saturation and residual oil saturation respectively. Samples saturated with water were stressed to a reference axial strain, flooded with oil to initial water saturation, and then water flooded until residual oil saturation was achieved. All experiments were repeated at least once to demonstrate reproducibility. The decrease in end point K_{ro} (Figure 3.6 and Table 3.2) during compactive volumetric strain was greatest

for the finest grain (Lower Fine Ottawa) sand at 25% (at 2% axial strain). The coarsest sample (Medium Ottawa) showed the least reduction of 14% respectively (at 3% axial strain). Upon dilation, the maximum increase was 10-12% for all the sands (Figure 3.6). At higher confining stress (200 psi), K_{ro} only decreased throughout the entire loading curve.

The decrease in K_{ro} and K_{rw} during compaction can be attributed to a reduction in pore size and increased tortuosity of the flow paths. Dilation on the other hand induced an increase in permeability, relative permeability and a reduction in capillary pressure. The changes observed for dilation are consistent with increased pore connectivity and pore throat sizes as well as with formation of shear bands. Oil and water may channel through the deformation bands resulting in the increased relative permeability to each phase.

The end point K_{rw} showed a different dependence on grain size than K_{ro} . Whereas the finest grain sample (Lower Fine Ottawa) had the greatest K_{ro} decrease during compactive behavior, the coarsest sample showed the strongest loss of K_{rw} (Table 3.3 and Fig. 3.7). During dilation, K_{rw} increased the most for the Lower Fine Ottawa sample as compared to its initial value, whereas the final K_{rw} in the Medium Ottawa sample was only slightly higher than the undeformed value (Figure 3.7). As with K_{ro} , K_{rw} uniformly decreased throughout loading at the higher confining stress (200 psi).

Axial Strain (%)	Lower Fine Ottawa		Lower Amalgamated Ottawa		Medium Ottawa		Lower Fine Ottawa (200 psi confining stress)
	Initial Exp	Rep Exp	Initial Exp	Rep Exp	Initial Exp	Rep Exp	
0	0.54	0.6	0.57	0.53	0.676	0.7	0.725
1	0.49	0.45	0.52	0.51	0.635	0.66	-
2	0.42	0.45	0.463	0.48	0.605	0.62	.7
3	0.53	0.49	0.4	0.43	0.54	0.49	-
5	0.59	0.63	0.615	0.59	0.725	0.7547	.66
10	0.61	0.62	0.7	0.67	0.79	0.77	0.63

Table 3.2: K_{r0} values and their comparison to values from repeated experiments (triaxial compression with 50 psi and 200 psi confining stress).

Axial Strain (%)	Lower Fine Ottawa		Lower Amalgamated Ottawa		Medium Ottawa		Lower Fine Ottawa (200 psi confining stress)
	Initial Exp	Rep Exp	Initial Exp	Rep Exp	Initial Exp	Rep Exp	
0	0.09	0.085	0.08	0.11	0.25	0.23	.18
1	0.0856	0.09	0.07	0.0856	0.19	0.18	-
2	0.075	0.082	0.05	0.09	0.18	0.15	.145
3	0.07	0.078	0.06	0.08	0.16	0.145	-
5	0.12	0.1	0.15	0.13	0.15	0.17	.134
10	0.13	0.15	0.14	0.135	0.2	0.25	0.118

Table 3.3: K_{rw} values and their comparison to values from repeated experiments (triaxial compression with 50 psi and 200 psi confining stress).

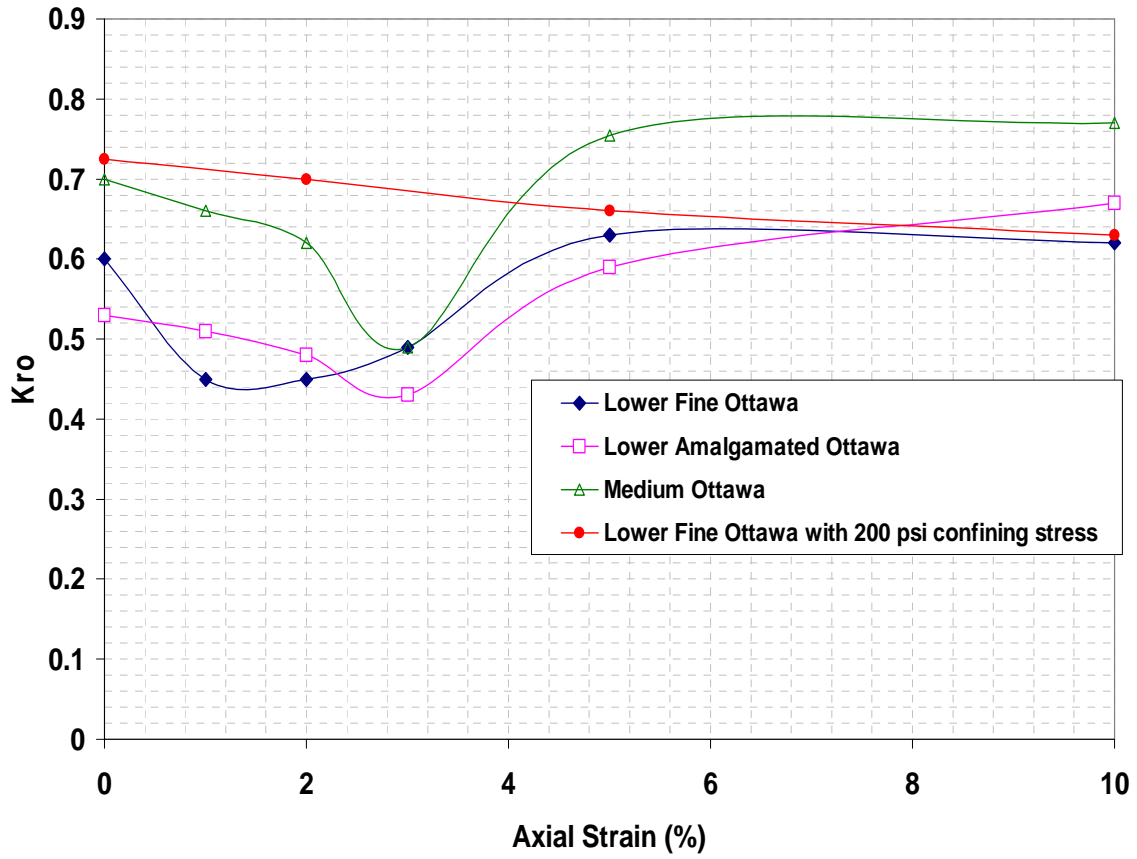


Figure 3.6: End point relative permeability to oil during triaxial compression with 50 and 200 psi confining stress. Lower Fine Ottawa had a lower end point relative permeability as compared to the other two sands.

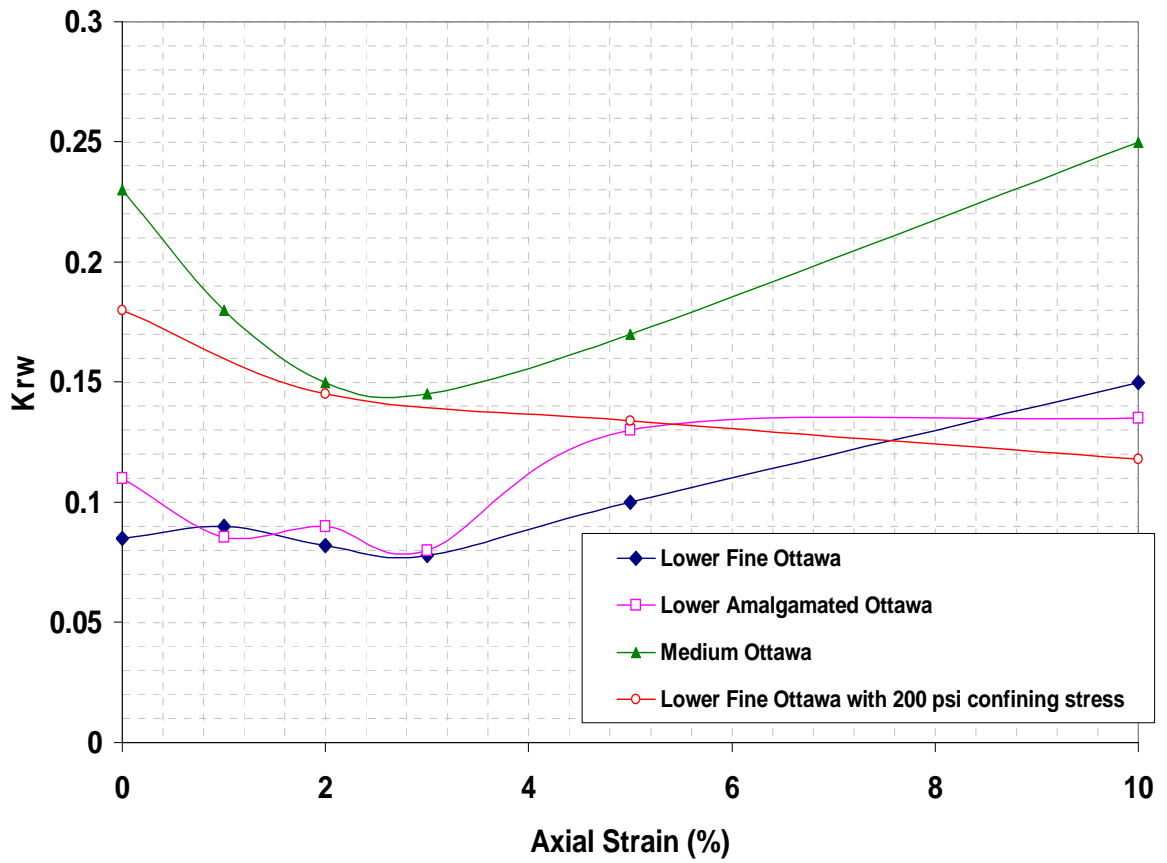


Figure 3.7: End point relative permeability to water in triaxial compression with 50 and 200 psi confining stress.

3.1.5 Residual Oil Saturation

Experimental measurements indicated increased S_{or} during compaction and a decreased S_{or} during dilation (Table 3.4 and Figure 3.8). A maximum 35% increase in residual oil saturation was observed during compaction for the coarsest sample. The Lower Fine Ottawa specimens compacted up to a 2% axial strain resulting in maximum residual oil saturation at 2% strain (an increase of 18% increase). Medium Ottawa and Lower Amalgamated Ottawa samples compacted up to an axial strain of 3% resulting in a maximum residual saturation at 3% axial strain of 35% and 30% respectively. During dilation, at 10% axial strain, the Lower Fine Ottawa samples showed a decrease of 21% in residual oil saturation and Lower Amalgamated Ottawa and Medium Ottawa specimens showed a 10% decrease in S_{or} .

Residual oil saturation affects the final recovery from a reservoir. The lower the residual oil saturation, the higher the ultimate recovery. The experimental results here suggest that dilatant shear deformation decreases residual oil saturation and thus lead to improved oil recovery. Factors affecting residual oil saturation in unconsolidated sand are particle size, pore size distribution, heterogeneity in pore sizes caused by stress, pore throat size change and the change in capillary forces associated with changes in pore geometry. One other factor would be the pores available for flow at a certain stress condition, as some of the pores might become dead end pores which only trap the fluid. Capillary entrapment describes the trapping of oil globules in the capillary network of the porous media. Capillary effects are stronger in assemblies with smaller pore throat radii. As the pores become smaller the capillary forces increase. Dilatancy increases pore and pore throat size, reducing the capillary pressure and allowing more oil to be drained easily by water.

Compression at 200 psi confining also caused an increase in residual oil saturation. At a 10 % axial strain S_{or} increased by 32%, compared to a reduction in S_{or} of 21% in sand samples deformed at 50 psi confining stress.

Axial Strain (%)	Lower Fine Ottawa		Lower Amalgamated Ottawa		Medium Ottawa		Lower Fine Ottawa (200 psi confining stress)
	Initial Exp	Rep Exp	Initial Exp	Rep Exp	Initial Exp	Rep Exp	
0	0.22	0.23	0.23	0.24	0.26	0.23	.2
1	0.23	0.27	0.24	0.27	0.29	0.26	-
2	0.26	0.29	0.27	0.29	0.288	0.28	.22
3	0.20	0.21	0.35	0.34	0.33	0.295	-
5	0.16	0.25	0.23	0.25	0.24	0.21	.24
10	0.13	0.18	0.22	0.18	0.20	0.17	0.28

Table 3.4: Residual oil saturation for the triaxial compression tests performed with 50 psi and 200 psi confining stress.

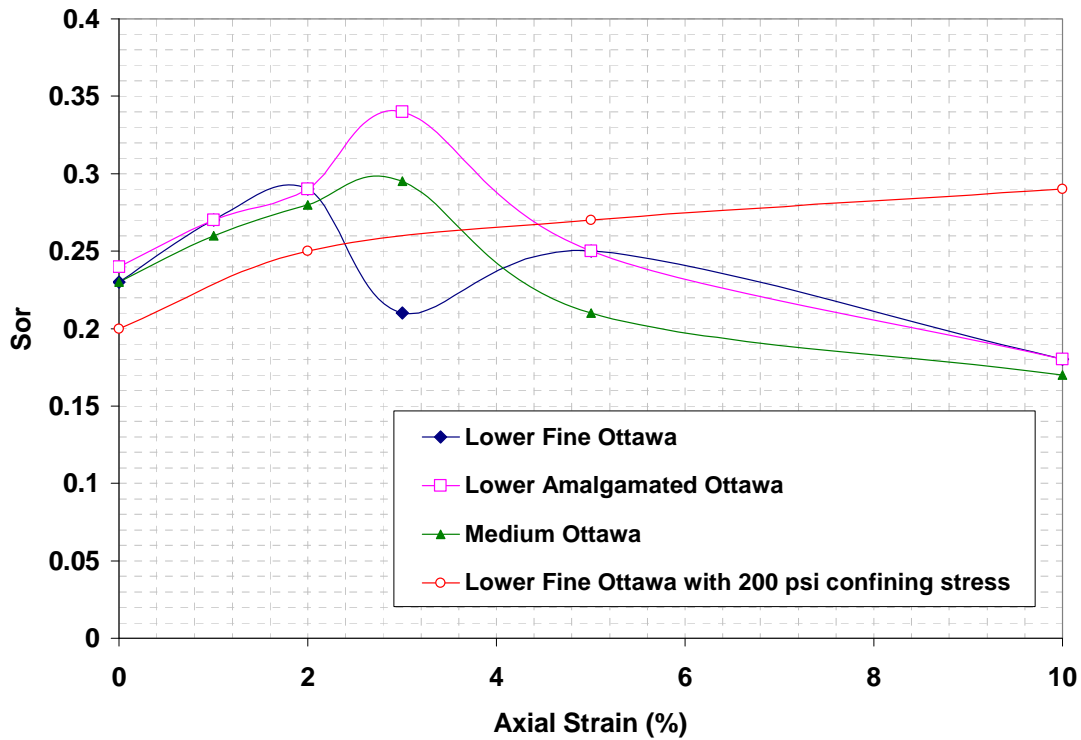


Figure 3.8: Residual oil saturation trend for the triaxial compression tests with 50 and 200 psi confining stress.

3.1.6 Initial Water Saturation

The initial water saturation decreased during compaction and increased during dilation (Figure 3.9). During the compactive loading phase, water from the smaller deformed pores is squeezed out into the larger pores where it can be drained by the displacing oil (this will only happen if the capillary pressure increase is not high enough to trap the water in the pores). S_{wi} is higher in Lower Fine sands than in the coarser Lower Amalgamated Ottawa and Medium Ottawa Sands. The smaller pore diameter pores and pore throats have a higher tendency to retain water due to higher capillary force in case of Lower Fine Ottawa. This explains the observed trend for the difference in initial water

saturation. Initial water saturation for the triaxial tests at 200 psi confining stress increased with increasing axial strain without the initial decrease seen at 50 psi.

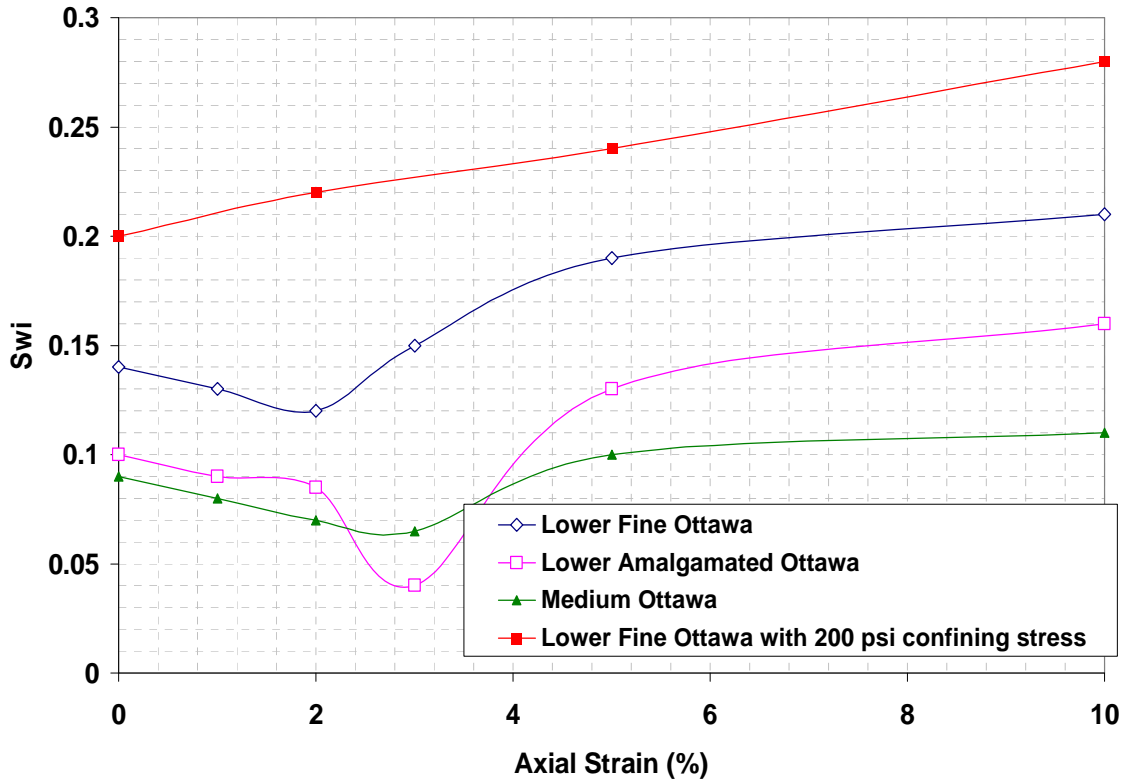


Figure 3.9: Initial water saturation for the triaxial compression tests with 50 psi and 200 psi confining stress.

3.1.7 Corey Type Curves for Relative Permeability

Relative permeability curves can be plotted from the experimentally measured end point values using the following Corey type equations

$$K'_{rw}(S_w) = K_{rw}(S_{or}) \left(\frac{S_w - S_{wi}}{1 - S_{wi} - S_{or}} \right)^{3.5} \quad (3.1)$$

$$K_{rw}'(S_w) = K_{ro}(S_{wi}) \left(\frac{1 - S_w - S_{wi}}{1 - S_{wi} - S_{or}} \right)^3 \quad (3.2)$$

S_{or} = residual oil saturation,

S_{wi} = initial water saturation,

K_{ro} = end point relative permeability to oil,

K_{rw} = end point relative permeability to water,

K_{rw}' = relative permeability to water, and

K_{ro}' = relative permeability to oil.

Figure 3.10 for Lower Fine Ottawa specimens shows that compaction (2% strain) and dilation (5% strain) affect the K_{ro} in opposite manners. However Lower Fine Ottawa showed the greatest shift in relative permeability curves from compaction (2% axial strain) to dilation (5% and 10% axial strain). Figure 3.11 and 3.12 show the oil-water relative permeability curves for Lower Amalgamated Ottawa and Medium Ottawa specimens, the relative permeability curves showed a similar trend to the oil relative permeability curves for Lower Fine Ottawa.

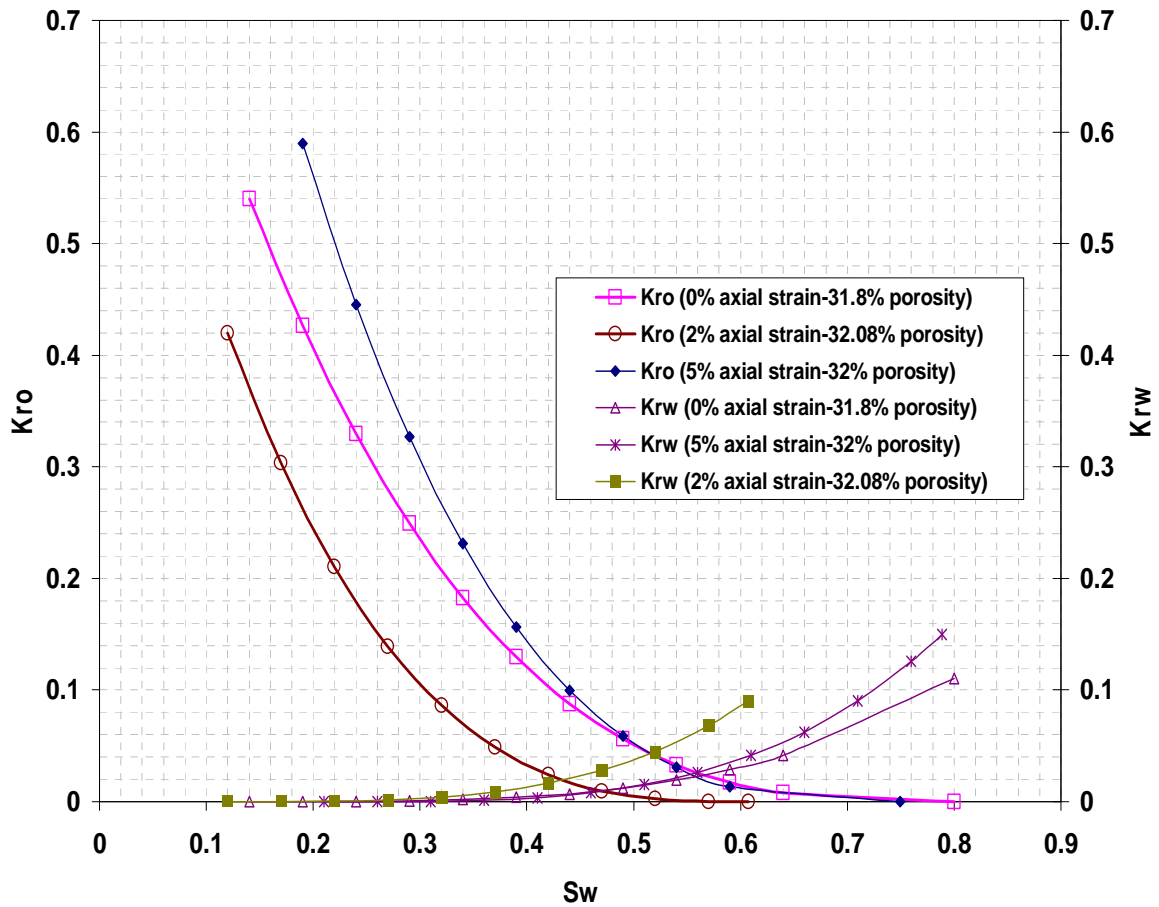


Figure 3.10: Relative permeability curves for Lower Fine Ottawa samples at 2%, 5% and 0% axial strain. The relative permeability curves are plotted using end point K_{ro} and K_{rw} derived from triaxial compression tests at 50 psi confining stress. The K_{ro} curves moved downwards for compaction (2% axial strain, indicating a reduction in K_{ro}) and upwards for dilation (5% axial strain, indicating an increase in relative permeability to oil). The end point K_{rw} increased but the curves do not show a clearly defined trend.

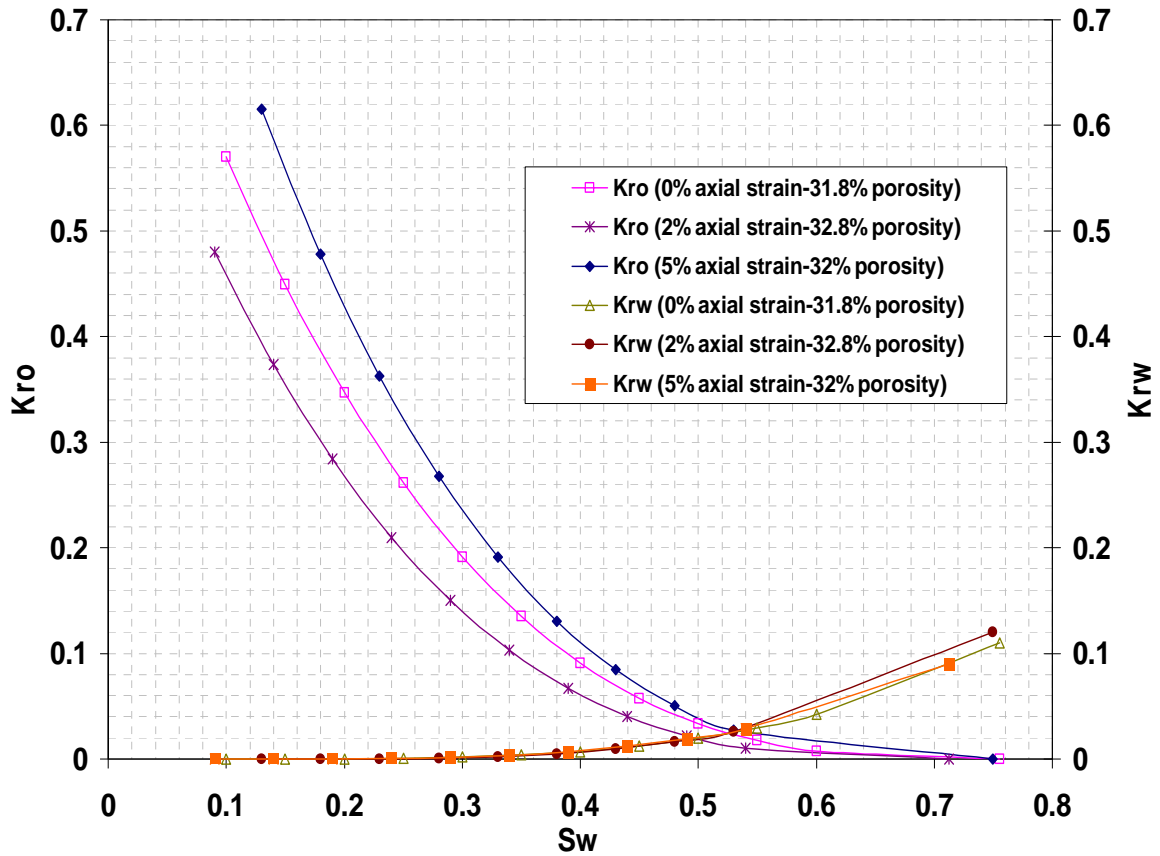


Figure 3.11: Relative permeability curves for Lower Amalgamated Ottawa samples at 2%, 5% and 10% axial strain. The relative permeability curves are plotted using end point K_{ro} and K_{rw} derived from triaxial compression tests with 50 psi confining stress. The K_{ro} curves moved downwards (decrease in K_{ro}) for compaction (2% axial strain) and upwards (increase in K_{ro}) for dilation (5% axial strain). The end point K_{rw} increased but the curves do not show a clearly defined trend.

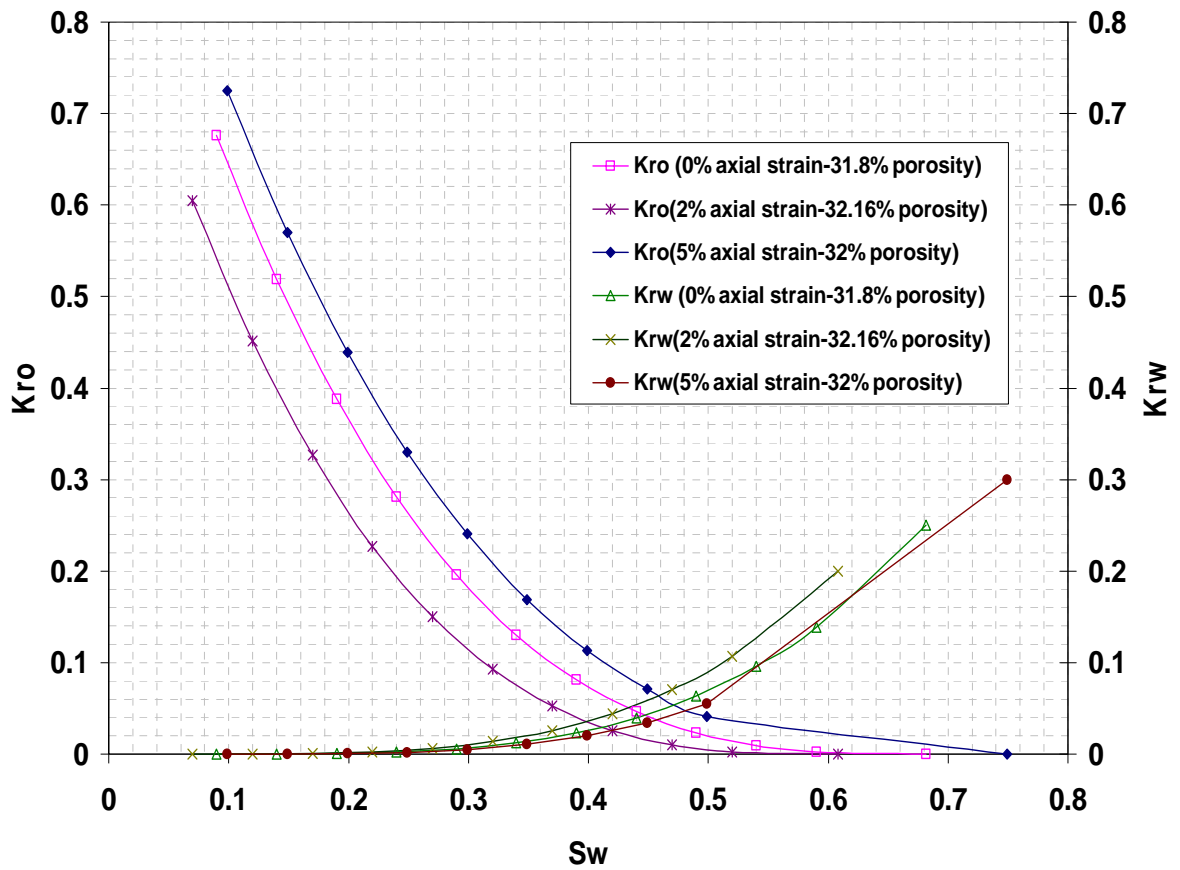


Figure 3.12: Relative permeability curves for Medium Ottawa specimens at 2%, 5% and 10% axial strain. The relative permeability curves are plotted using end point K_{ro} and K_{rw} derived from triaxial compression tests with 50 psi confining stress. The oil relative permeability curves moved downwards (decrease in K_{ro}) for compaction (2% axial strain) and upwards (increase in K_{ro}) for dilation (5% axial strain). The end point K_{rw} increased but the curves do not show a clearly defined trend.

3.2 RADIAL EXTENSION TESTS

3.2.1 Stress-Strain Behavior

Radial extension tests represent a path of mean decreasing stress, which is the path very similar to that expected in SAGD operations. The sand samples were loaded isotropically to 200 psi and the confining stress was decreased to achieve the desired value of the axial strain while keeping the axial stress constant at 200 psi.

The stress–strain behavior for the sand samples was similar to each other and is not dependent on the grain size and the sand type (Figure 3.13). The samples exhibited a sharp increasing differential stress as the confining stress was reduced and reached the peak stress, after which the differential decreased due to sample failure. The peak stress varied between 100-160 psi for the sand samples and is reached between 2-4% axial strain. The stress-strain behavior for the samples (Figure 3.14) tested at 500 psi axial stress (with a peak stress of 370 psi) was similar to the samples tested at a 200 psi constant axial stress (with a peak stress of 160 psi).

The large bumps in the stress-strain plots (Figures 3.13 and 3.14) were a result of operating the confining stress pumps under pressure control and using 20 psi confining stress drop increments for the radial extension tests. The axial stress was independently controlled by the load frame and was set to servo-control to maintain a constant load, but the ram couldn't move fast enough to keep up with the quick change in confining stress driven by the confining stress pump. Consequently, while the confining stress was lowered, the axial strain remained almost constant, causing the axial stress to drop (Appendix B, Figure B7, B8, B9 and B10). This resulted in a drop of differential stress as well , as the axial stress dropped more than the confining stress for each step.

Young's Modulus for the radial extension test was calculated using the following equations,

$$-\frac{d\sigma_c}{d\varepsilon_{axial}} = \frac{E}{2\nu} \quad (3.3)$$

and

$$-\frac{d\sigma_c}{d\varepsilon_v} = \frac{E}{2(1-2\nu)}, \quad (3.4)$$

where

$\frac{d\sigma_c}{d\varepsilon_{axial}}$ = slope of the confining pressure versus axial strain curve and

$-\frac{d\sigma_c}{d\varepsilon_v}$ = slope of confining pressure versus volumetric strain curve.

The radial extension tests resulted in lower strength (100 to 160 peak differential stress) and similar modulus (12600 to 21000 psi) as compared to the triaxial tests at 40 psi confining stress. Poisson's ratio for the Lower Fine, Lower Amalgamated Ottawa and Medium Ottawa was 0.30, 0.25 and 0.21, respectively. The stress-strain curves (up to axial strains of 2%, 5% and 10%) for Lower Fine Ottawa, Lower Amalgamated Ottawa and Medium Ottawa samples can be found in Appendix B (Figure B11, B12 and B13).

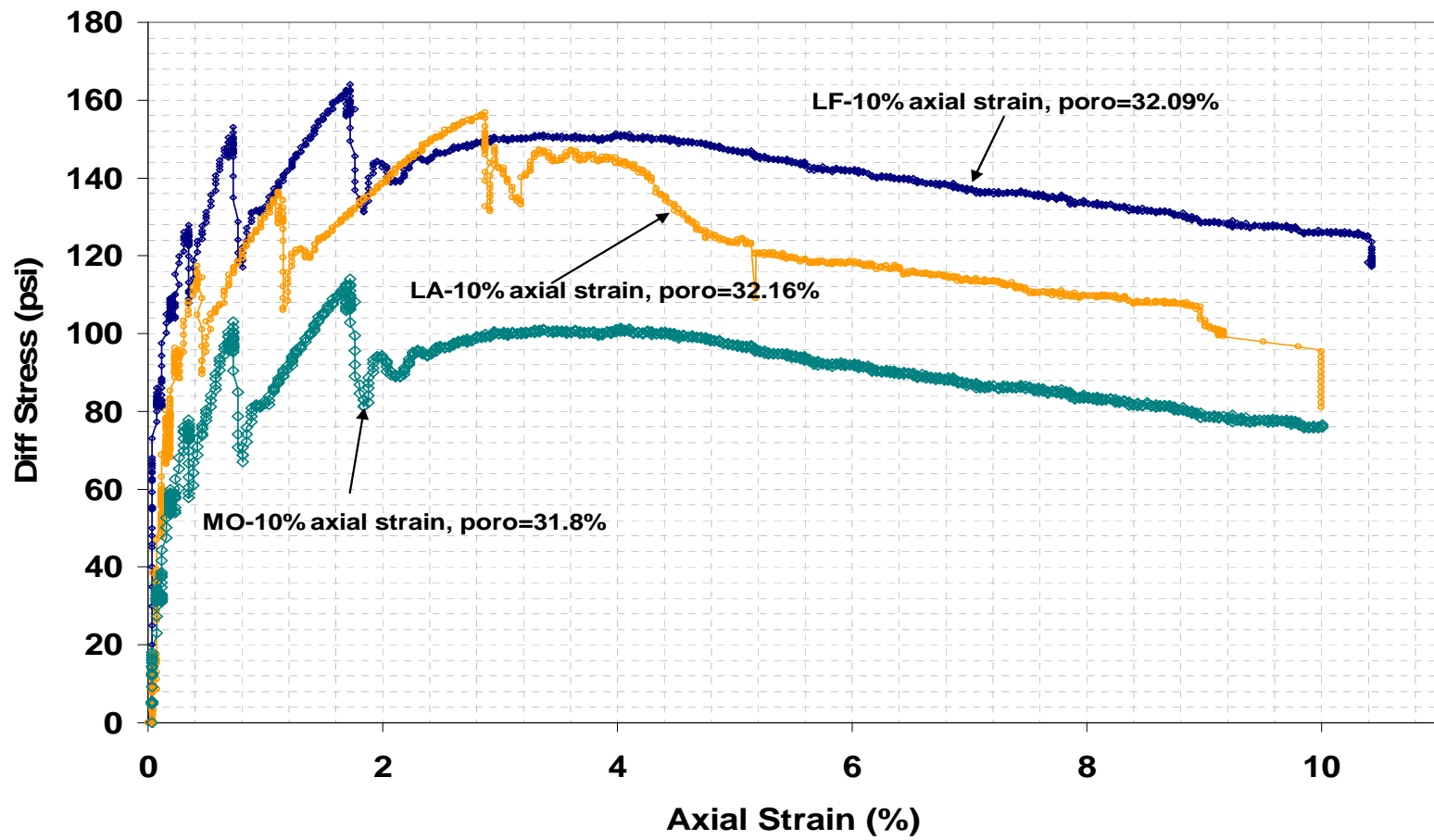


Figure 3.13: Stress-strain curves for radial extension tests with constant axial stress of 200 psi and decreasing radial stress (LF-Lower Fine Ottawa, LA-Lower Amalgamated Ottawa, MO-Medium Ottawa).

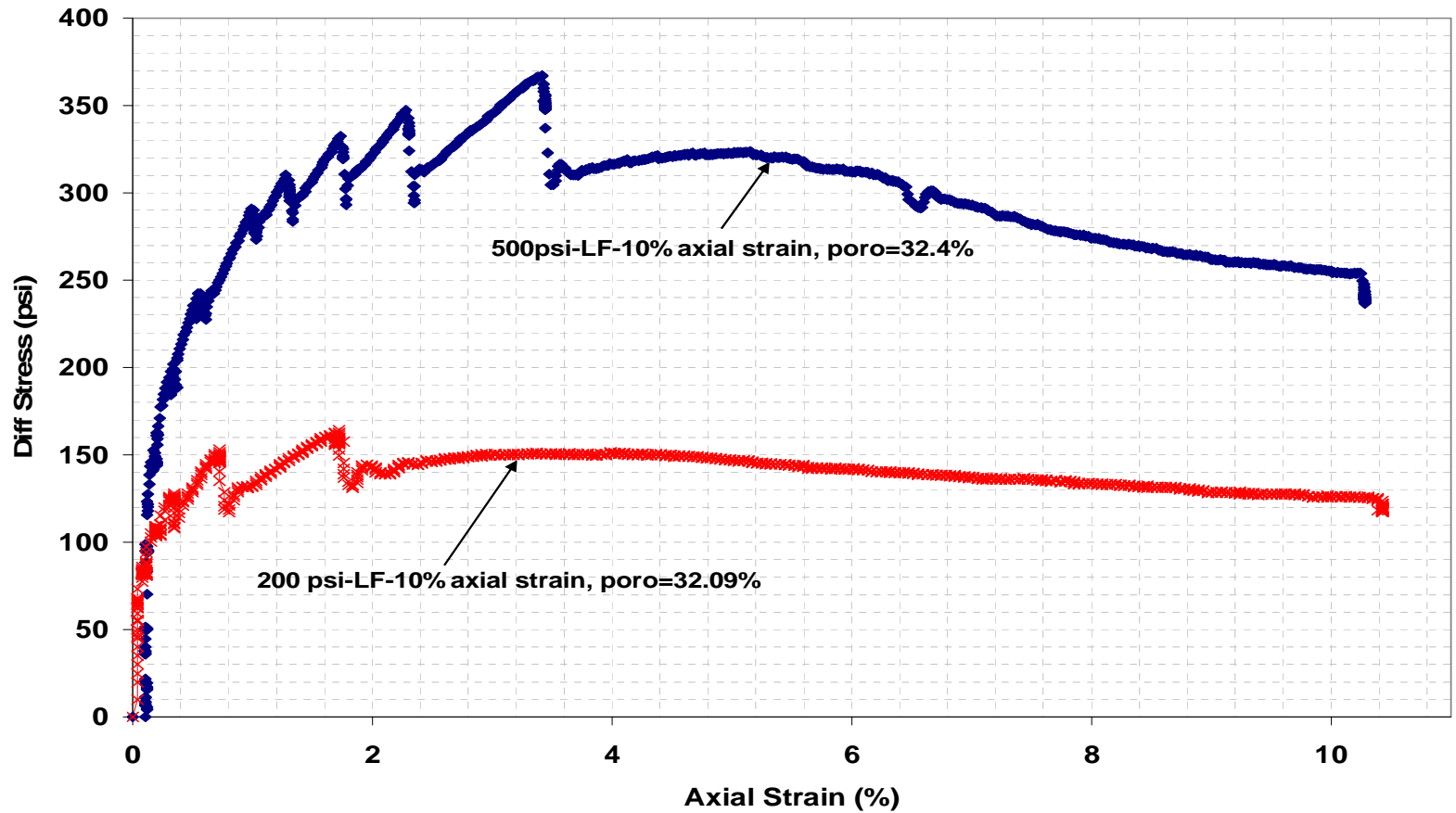


Figure 3.14: Stress-strain curves for radial extension tests (Lower Fine Ottawa) with constant axial stress of 200 and 500 psi and decreasing radial stress.

3.2.2 Volumetric Strain

In the radial extension tests, the decreasing confining pressure resulted in sample dilation from the start of the deformation (Figure 3.15). To achieve an axial strain of about 10%, the confining pressure was reduced to 40 or 50 psi, depending on the type of sand. Lower Fine Ottawa samples showed the highest values of volumetric strain with a maximum of -10%, Lower Amalgamated Ottawa had a maximum of -8.8% and Medium Ottawa specimens had a value of -7.9% volumetric strain at an axial strain of 10%. For volumetric strain curves covering all the experiments used in this study, refer to Appendix B (Figure B14, B15 and B16).

The volumetric strain up to a 5% axial strain is the same for both the 200 psi and 500 psi cases. After 5% axial strain, the volumetric strain in the 500 psi case flattens out while it continues to dilate for the 200 psi case. This indicates that the higher confining stress limits the dilation, but does not prevent it.

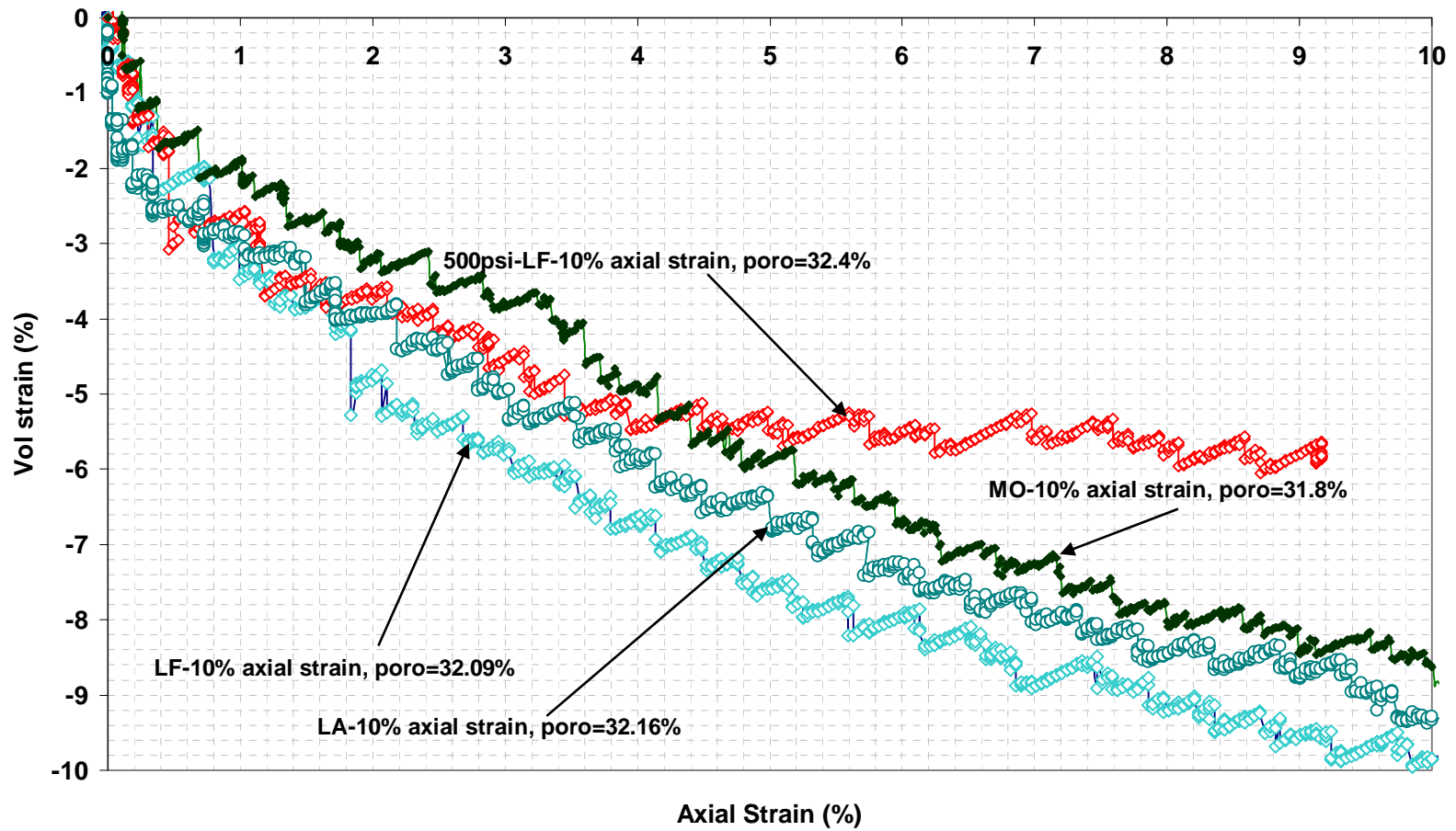


Figure 3.15: Volumetric strain curves for radial extension tests with constant axial stress of 200 and 500 psi and decreasing confining stress (LF-Lower Fine Ottawa, LA-Lower Amalgamated Ottawa, MO-Medium Ottawa).

3.2.3 Permeability

The radial extension tests started at a lower initial permeability (Figure 3.15) than the triaxial tests because of the higher isotropic stress (200 psi versus 50 psi for the triaxial tests). Sample deformation showed a monotonic absolute permeability increase at all values of axial strain. At an axial strain of 10%, the permeability enhancement varied from 14% to 50% (Figure 3.16) with the greatest enhancement occurring for the finest grain size sample. The higher dilation experienced in radial extension tests is the probable cause for the greater permeability enhancement as compared to the triaxial compression tests (Table 3.5).

For 500 psi axial stress case, a 33% increase in permeability was observed in comparison to 53% increase with 200 psi axial stress for the same grain size sample (Lower Fine Ottawa). These results are comparable to the results from Oldakowski (1998), who observed a lesser increase in permeability when sand samples were unloaded from higher isotropic stress conditions by reducing the confining pressure. However, unlike the triaxial tests, where increased confining stress prevented permeability enhancement, even though dilatant volumetric strain was observed, the higher stress radial extension test still had increased permeability with deformation.

Sand Type	Lower Fine Ottawa		Lower Amalgamated Ottawa		Medium Ottawa		Lower Fine Ottawa (500 psi axial stress)		
	Strain (%)	Porosity (%)	Permeability (D)	Porosity (%)	Permeability (D)	Porosity (%)	Permeability (D)	Porosity (%)	Permeability (D)
0		32.6	5.6	32.8	19	31.7	30	32.7	4.5
2		31.75	6.8	32.34	22.3	32.8	31.5	32.2	5
5		32.3	7.7	32.45	23.8	32.62	33	32	5.6
10		32.09	8.45	31.8	25.72	32.16	35.92	32.4	6.1

Table 3.5: Porosity and permeability of sand samples with a 200 and 500 psi constant axial stress and decreasing confining stress.

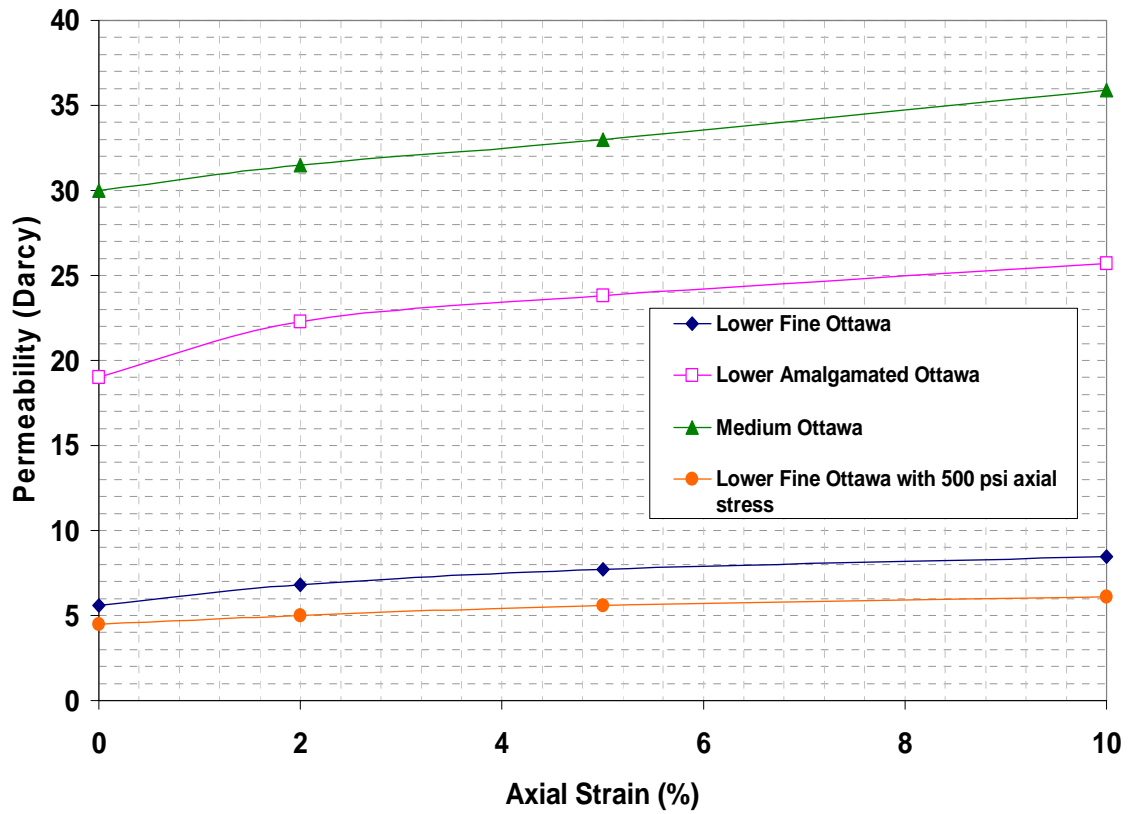


Figure 3.15: Permeability of different sand samples tested at different values of axial strain with a constant 200 and 500 psi axial stress. Increasing axial strain values denote a decreasing confining stress and increasing permeability.

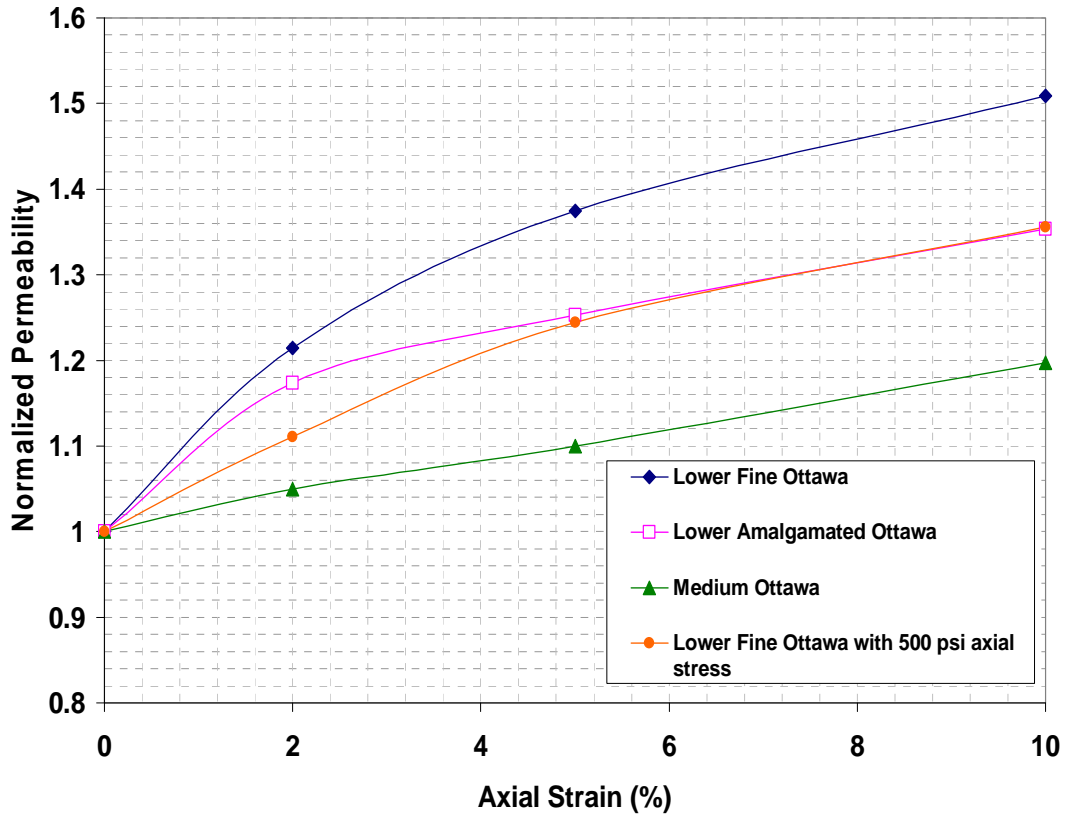


Figure 3.16: Normalized permeability of different sand samples tested at different values of strain with a constant 200 and 500 psi axial stress. Increasing axial strain values denote a decreasing confining stress and increasing permeability.

3.2.4 Relative Permeability

Relative permeability followed similar trend to absolute permeability (increase due to dilation). At a value of 10% axial strain, the Lower Fine Ottawa, Lower Amalgamated Ottawa and Medium Ottawa samples showed improvements of 37%, 28% and 30%, respectively, in the end point K_{ro} (Table 3.6 and Fig. 3.17). The end point K_{rw} (Table 3.7 and Figure 3.18) also showed a maximum increase of 30%.

For samples with 500 psi axial stress a 21% increase in end point K_{ro} and 35 % increase in end point K_{rw} was observed at 10% axial strain (Table 3.7 and Figure 3.18), which is lower than the samples tested with 200 psi axial stress.

Radial extension tests showed higher improvement in end point relative permeability as compared to triaxial compression tests, since the specimens dilated from the beginning and lead to a higher volumetric strain and absolute permeability improvement.

Axial Strain (%)	Lower Fine Ottawa		Lower Amalgamated Ottawa		Medium Ottawa		Lower Fine Ottawa (500 psi axial stress)
	Initial Exp	Rep Exp	Initial Exp	Rep Exp	Initial Exp	Rep Exp	
0	0.58	0.6	0.51	0.53	0.59	0.55	.55
2	0.66	0.61	0.60	0.62	0.68	0.64	.6
5	0.745	0.76	0.69	0.66	0.70	0.69	.66
10	0.79	0.75	0.72	0.68	0.76	0.72	.68

Table 3.6: K_{ro} in the radial extension tests with a constant 200 and 500 psi axial load and decreasing radial stress. The table also contains the values for the repeated experiments for comparison with the values obtained from initial experiments.

Axial Strain (%)	Lower Fine Ottawa		Lower Amalgamated Ottawa		Medium Ottawa		Lower Fine Ottawa (500 psi axial stress)
	Initial Exp	Rep Exp	Initial Exp	Rep Exp	Initial Exp	Rep Exp	
0	.14	0.16	0.16	0.13	0.12	0.17	.1
2	0.18	0.17	0.18	0.15	0.15	0.19	.12
5	0.25	0.23	0.21	0.19	0.24	0.28	.14
10	0.28	0.29	0.215	0.20	0.26	0.29	.145

Table 3.7: K_{rw} in the radial extension tests with a constant 200 and 500 psi axial load. The table also contains the values for the repeated experiments for comparison with the values obtained from initial experiments.

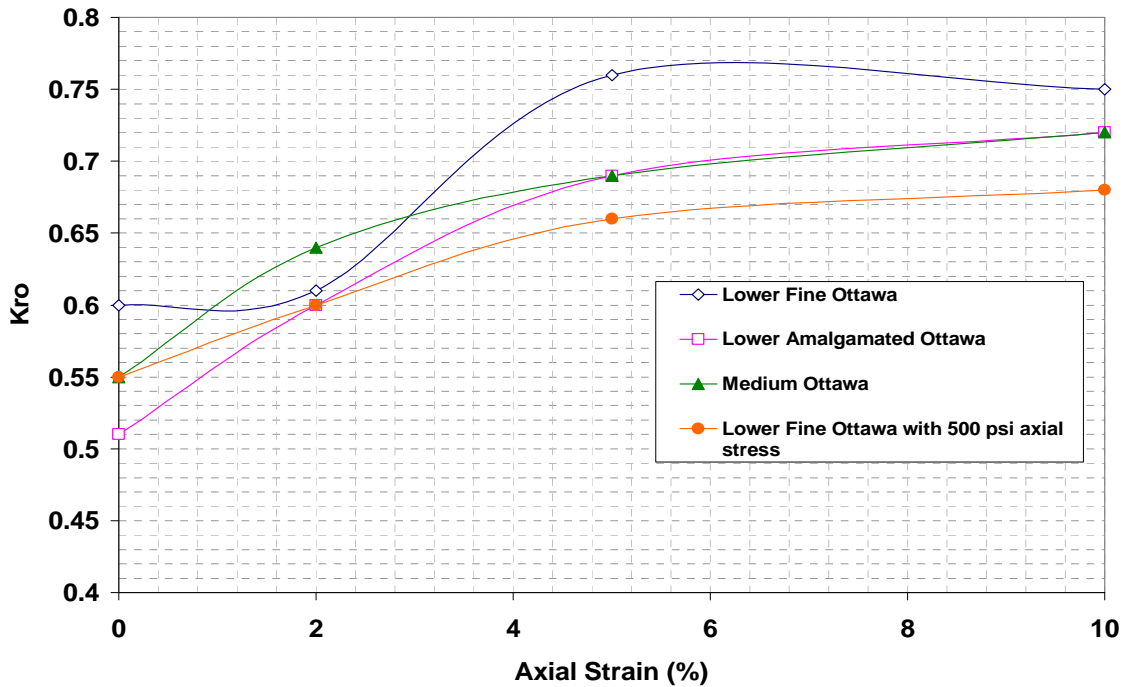


Figure 3.17: Comparison of end point relative permeability to oil in the three sands at a constant axial stress of 200 and 500 psi. All the sands show an increase in end point relative permeability to oil.

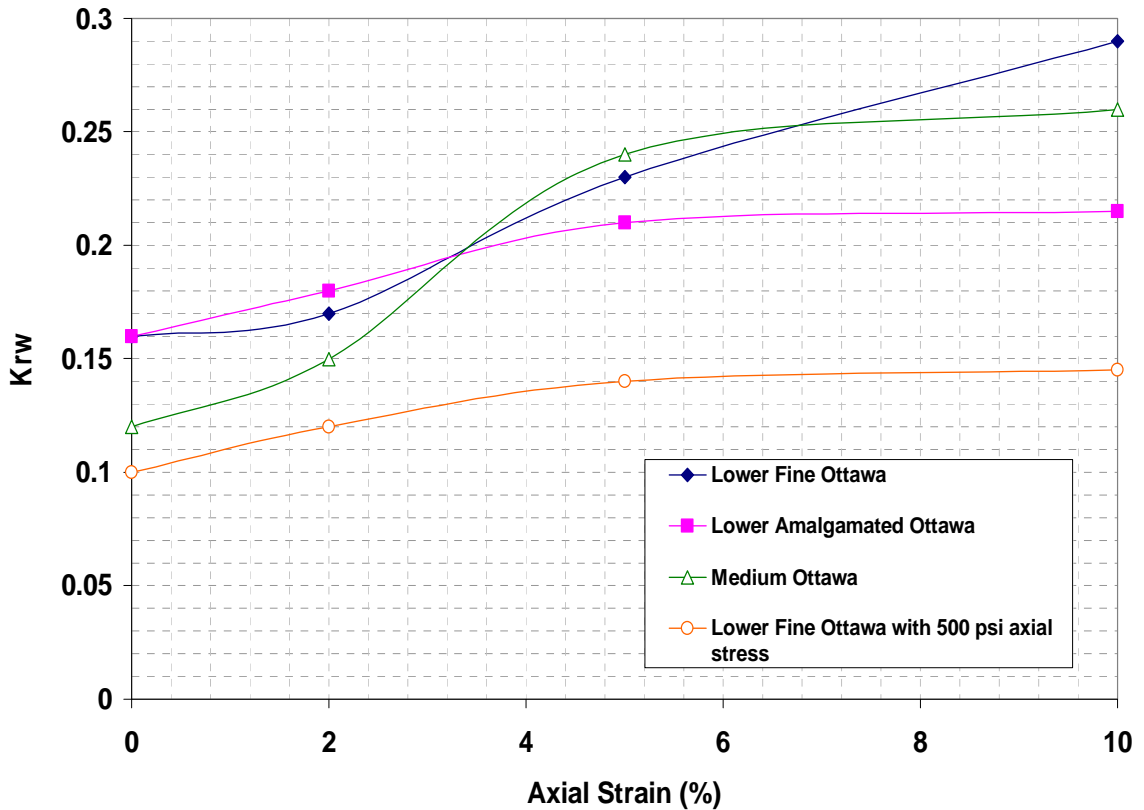


Figure 3.18: Comparison of end point relative permeability to water in the three sands at a constant axial stress of 200 and 500 psi. All the sands show an increase in end point relative permeability to water.

3.2.5 Residual Oil Saturation

In the radial extension tests, the residual oil saturation decreased with increasing axial strain (Table 3.8 and Figure 3.19). Lower Fine Ottawa samples showed the greatest decrease in residual oil saturation (about 50%) while Lower Amalgamated Ottawa and Medium Ottawa specimens showed a maximum of 40% decrease in residual oil saturation. Decreasing residual oil saturation can be attributed pore size increase which reduces the capillary forces and makes it easier for the water to displace oil, thereby

leading to lower residual oil saturation. Similarly, oil filled shear bands have lower capillary pressure and trap less oil than the pores.

The greater reduction in residual oil saturation for the radial extension tests than for the triaxial compression tests can be attributed to the decreasing mean stress path and higher dilation.

Axial Strain (%)	Lower Fine Ottawa		Lower Amalgamated Ottawa		Medium Ottawa		Lower Fine Ottawa (500 psi axial stress)
	Initial Exp	Rep Exp	Initial Exp	Rep Exp	Initial Exp	Rep Exp	
0	.28	0.227	0.23	0.24	0.32	0.26	.29
2	0.20	0.18	0.17	0.20	0.24	0.22	.22
5	0.14	0.156	0.15	0.12	0.19	0.174	.19
10	0.13	0.16	0.13	0.115	0.18	0.15	.175

Table 3.8: Residual oil saturation for the three types of sands with decreasing confining pressure and constant axial stress of 200 psi.

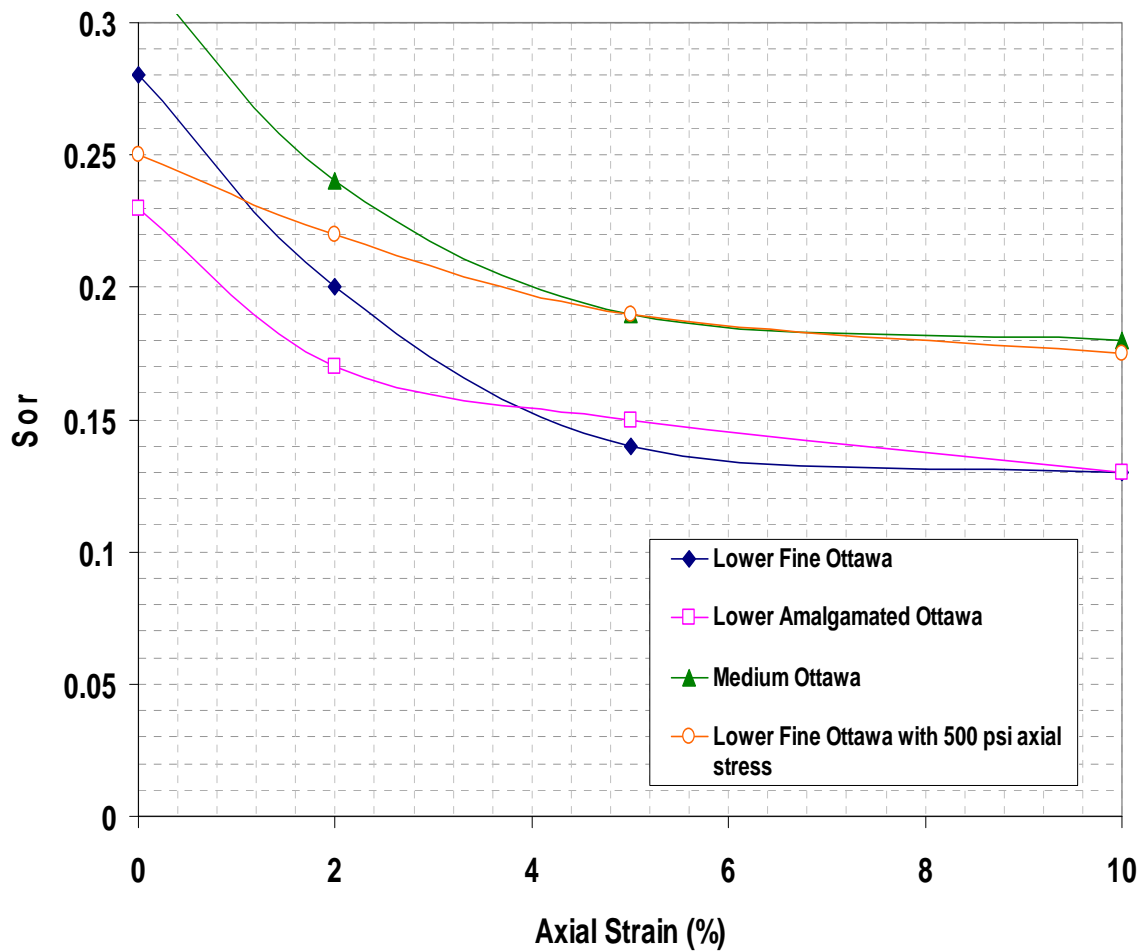


Figure 3.19: Change in residual oil saturation with increasing axial strain in radial extension tests with decreasing confining pressure and a constant 200 psi axial stress.

3.2.6 Initial Water Saturation

The initial water saturation in the sand packs showed (Figure 3.20) an increase (about 30%) as the sand samples dilated, which can be attributed to increased pore sizes and porosity, causing more water to be required to line the pores. Moreover, oil might force its way through the shear bands (preferential flow of water or oil through shear bands due to high permeability) ignoring some of the areas in the sand pack, where water

can remain trapped. The combined effect of oil channeling and increased pore size cause S_{wi} to be higher.

For 500 psi axial stress samples exhibited an increase of 20% as compared to 30% for Lower Fine Ottawa specimens at 200 psi axial stress.

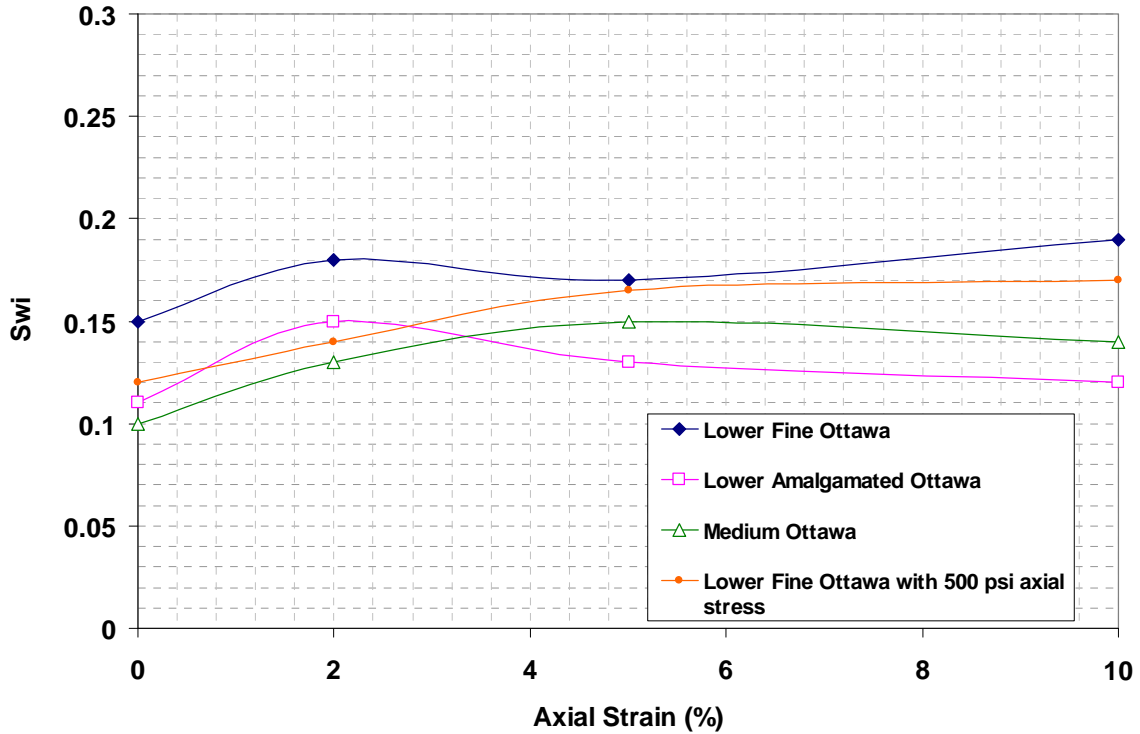


Figure 3.20: Change in initial water saturation during the radial extension tests with decreasing confining stress and constant axial stress of 200 and 500 psi.

3.2.7 Corey Type Relative Permeability Curves

Using the Corey's equations (Equation 3.1 and 3.2) the relative permeability curves were plotted (Figure 3.21, 3.22 and 3.23). The K_{ro} curve consistently shifted upwards at increasing values of strain, indicating that the K_{ro} increased at all the values of water saturation.

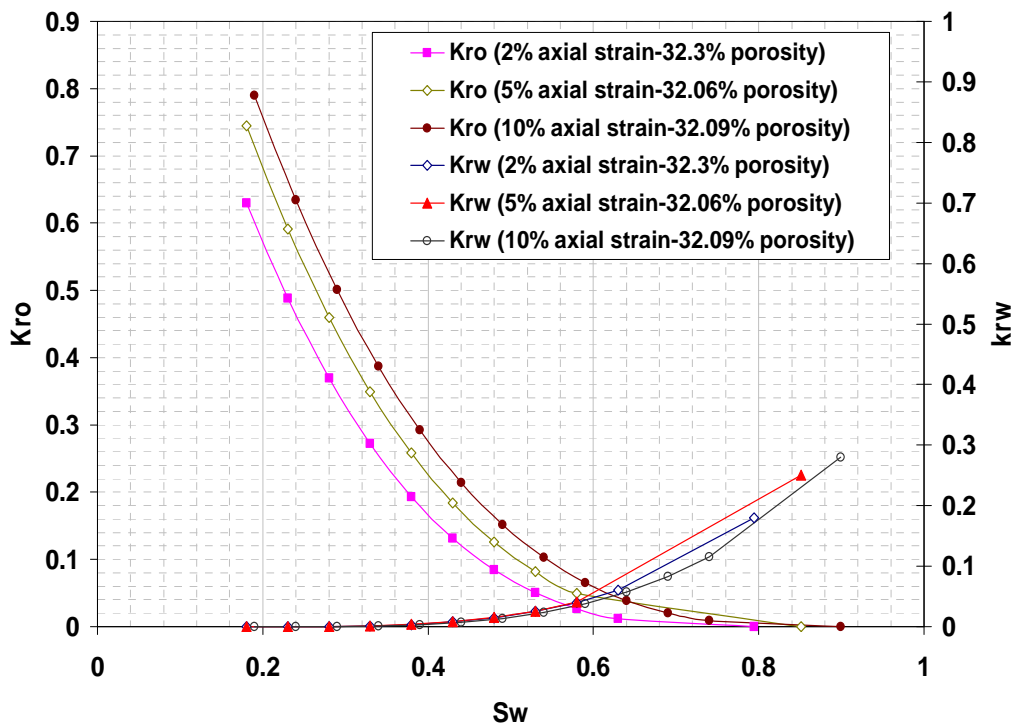


Figure 3.21: Relative permeability curves for oil and water for Lower Fine Ottawa in radial extension tests with 200 psi axial stress. The K_{ro} curves show a clear shift upwards with increasing strain, indicating an increase in K_{ro} at any given water saturation. While K_{rw} curves do not show a well defined trend.

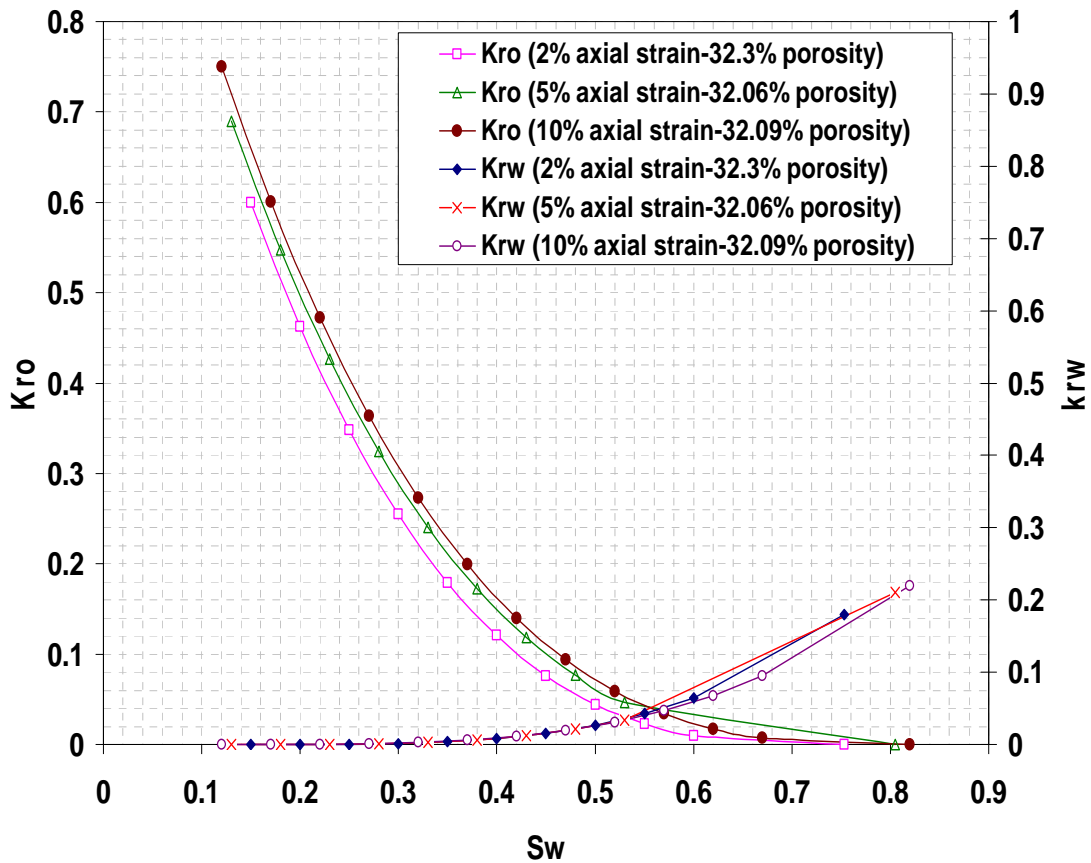


Figure 3.22: Relative permeability curves for oil and water for Lower Amalgamated Ottawa in radial extension tests with 200 psi axial stress. The K_{ro} curves show a clear shift upwards with increasing strain, indicating an increase in K_{ro} at any given water saturation. But the shift is less as compared to Lower Fine Ottawa. The K_{rw} curves show a downward shift with increasing strain, but it not a well defined or a considerable change.

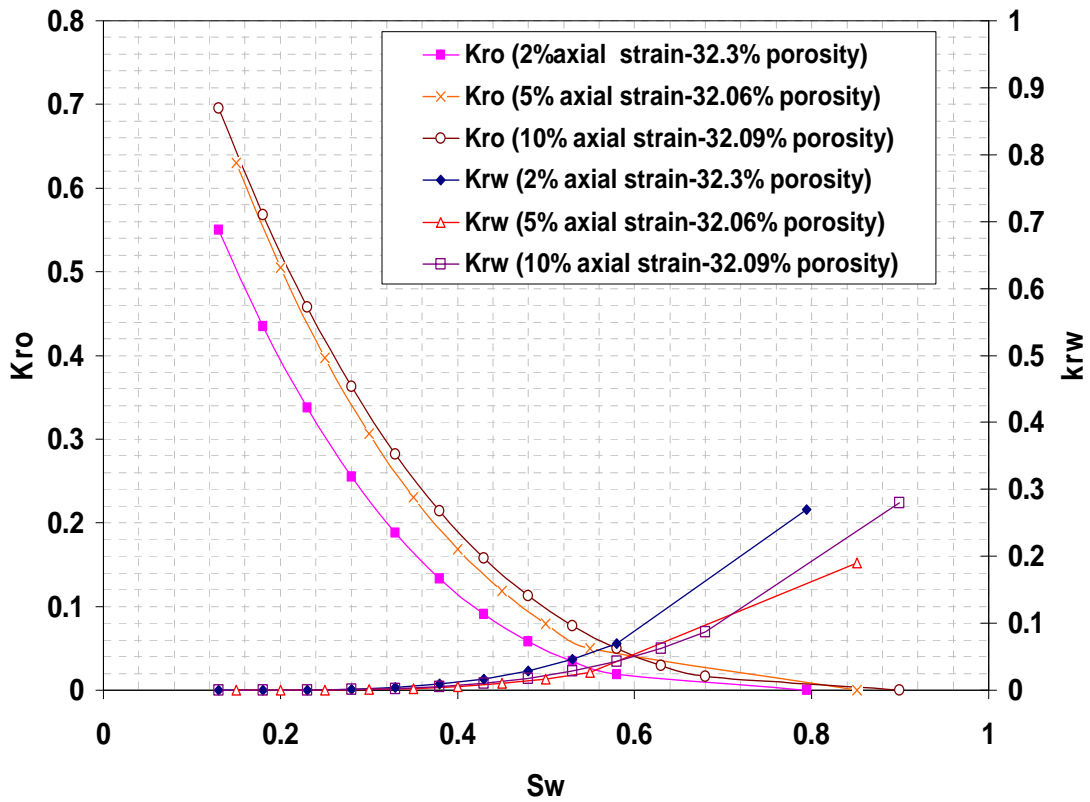


Figure 3.23: Relative permeability curves for oil and water for Medium Ottawa in radial extension tests with 200 psi axial stress. The K_{ro} curves show a clear shift upwards with increasing strain, indicating an increase in K_{ro} at any given water saturation. But the shift is less as compared to Lower Fine Ottawa. The K_{rw} curves show a downward shift with increasing strain, but it not a well defined or a considerable change.

3.3 CAT SCAN IMAGES OF THE SAND PACKS AND POROSITY ANALYSIS

CT scans taken at a 10% axial strain were taken with the sample still under stress. However, because of the size and the steel in the load frame, the triaxial cell had to be removed to be scanned. The axial shortening of the sample was maintained constant by using a clamping system attached to the upper ram. The confining pressure was preserved by closing the valve between the pump and the cell before disconnecting. The scanner used in this investigation is a medical CAT scanner modified for scanning cores and imaging flow experiments. All the sand packs were imaged using the same scanner resolution and using the same color spectrum range so that a comparison between the images could be done.

Similar deformation patterns were observed (from the images) for the triaxial compression tests (Figure 3.24 and 3.25) and the radial extension tests (Figures 3.26 and 3.27). A conical shear band propagated from the base and top of the samples, narrowing in radius toward the middle of the sample. In the middle of the sample, radial shear bands emanated from the core. Moving away from the sample center, the number of radial bands decreased and ultimately merged into a conical shear features. Darker colors (in grey scale) in the images indicated lower density and consequently higher porosity. The shear bands from the radial extension loading path had a greater width and darker color (in grey scale) than those observed in triaxial compression test samples. This observation was consistent with the greater improvements observed in absolute and relative permeability for the radial extension tests than those in the triaxial compression tests. .

Some of the CT images from the radial and triaxial compression tests were analyzed to determine specimen porosity in the shear deformation bands develop in the sand packs. The sand pack is composed of a sand matrix and pores filled with water. The

porosity change along a traverse across a horizontal slice of the sample was calculated using the attenuation coefficient (CT number) of the water, sample sand matrix and the CT numbers along the traverse (Tian *et al.*, 2000):

$$CT_m^w = (1 - \phi)CT_R + \phi * CT_w \quad (3.5)$$

$$\phi = \frac{CT_m^w - CT_R}{CT_w - CT_R} \quad (3.6)$$

CT_R = attenuation coefficient of rock matrix,

CT_w = attenuation coefficient of water, and

CT_m^w = attenuation coefficient of the sand sample fully saturated with water.

CT_R is calculated (equation 3.5) by using the initial porosity of the sample (calculated at the start of the experiment) and CT_m^w (attenuation coefficient of the undisturbed sand sample). The calculated value of CT_R is then used in equation 3.6 for calculation of porosity at along a traverse in the image slice. A MATLAB code was used to obtain the CT numbers across the chosen traverse across the sample.

Figure 3.28 and 3.29 shows the variation of porosity across the traverse shown in yellow on the image for radial extension tests with constant 500 psi axial stress. The porosity was plotted against a distance index. This distance index denoted the distance from one edge of the sample image slice to the other. Humps in the porosity graph are clearly correlated to the points where the traverse intersects the high porosity deformation bands and also to the humps seen in the CT number plot. The variation in porosity is dependent on the CT numbers. The lower the CT numbers the higher the porosity and vice versa. The bigger humps in the CT number plot were due to the aluminum outer cylinder and water between the sand sample and the outer aluminum cylinder. Results for Radial extension tests with 500 psi constant axial stress show a maximum increase of

55% in porosity. Figure 3.30 shows the porosity variations for a set of slices taken from the middle to the bottom of the sample for triaxial compression test with 200 psi constant confining stress. It is evident from the plots that the center of the samples had lesser improvement in porosity (the other case in some slices was that the area surrounding the shear bands compacted resulting in porosity decline); where as shear bands show a larger increase in porosity. These shear bands are responsible for the increase in permeability and porosity observed in the flow experiments. However, it may be the case that the areas surrounding the shear bands compact to a greater degree overcoming the effect of increased porosity in shear bands, resulting in an overall permeability decrease in sand specimens (tests in triaxial compression with 200 psi confining stress).

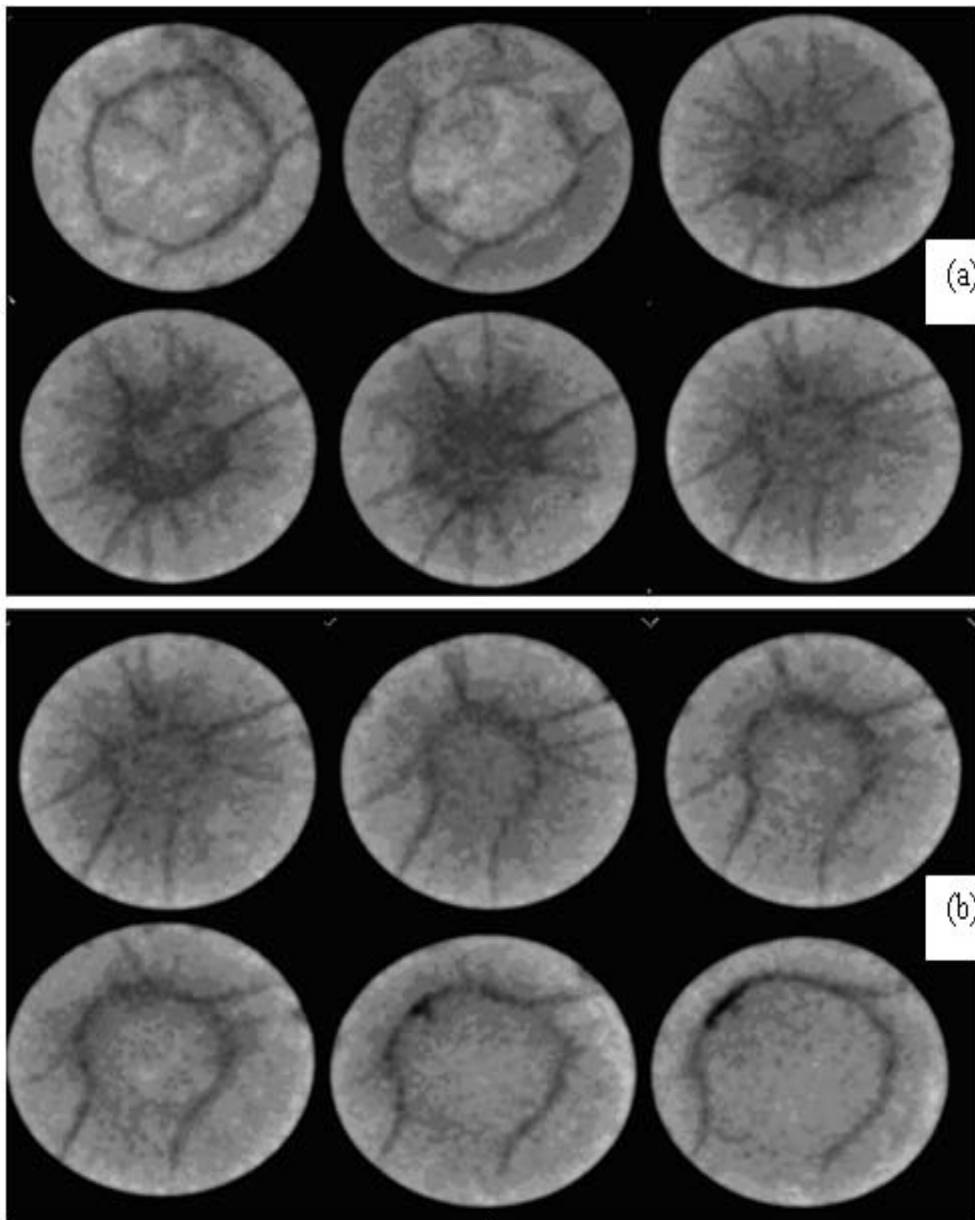


Figure 3.24: Images from the triaxial compression tests on Lower Fine Ottawa with constant 50 psi confining pressure. (a)The pictures show the change in fracture pattern when moving from top of the sample to the middle of the sand sample. (b) The pictures show the change in fracture pattern when moving from middle of the sample to the bottom of the sand sample.

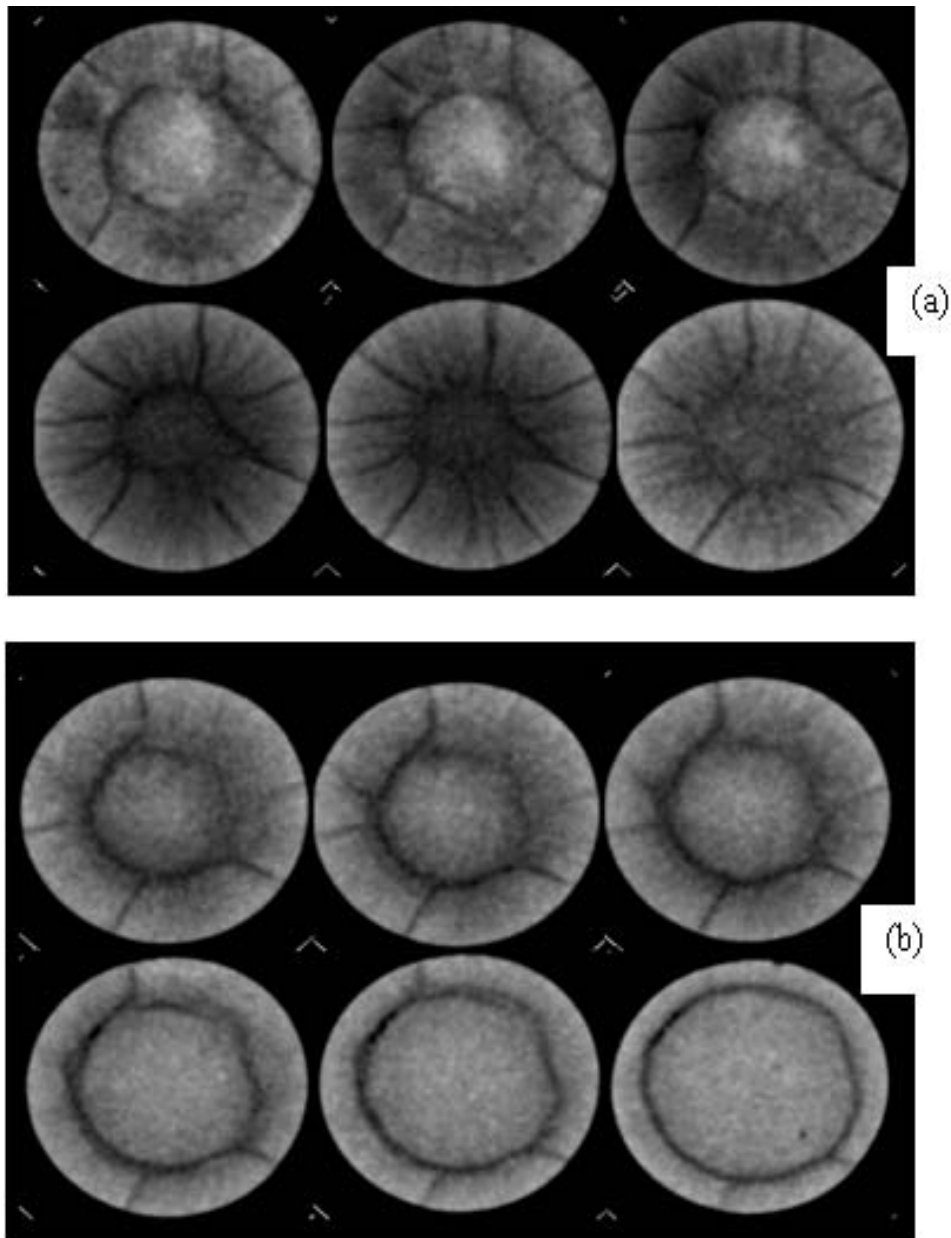


Figure 3.25: Images from the triaxial compression tests on Lower Fine Ottawa with constant 200 psi confining pressure. (a) The pictures show the change in fracture pattern when moving from top of the sample to the middle of the sand sample. (b) The pictures show the change in fracture pattern when moving from middle of the sample to the bottom of the sand sample.

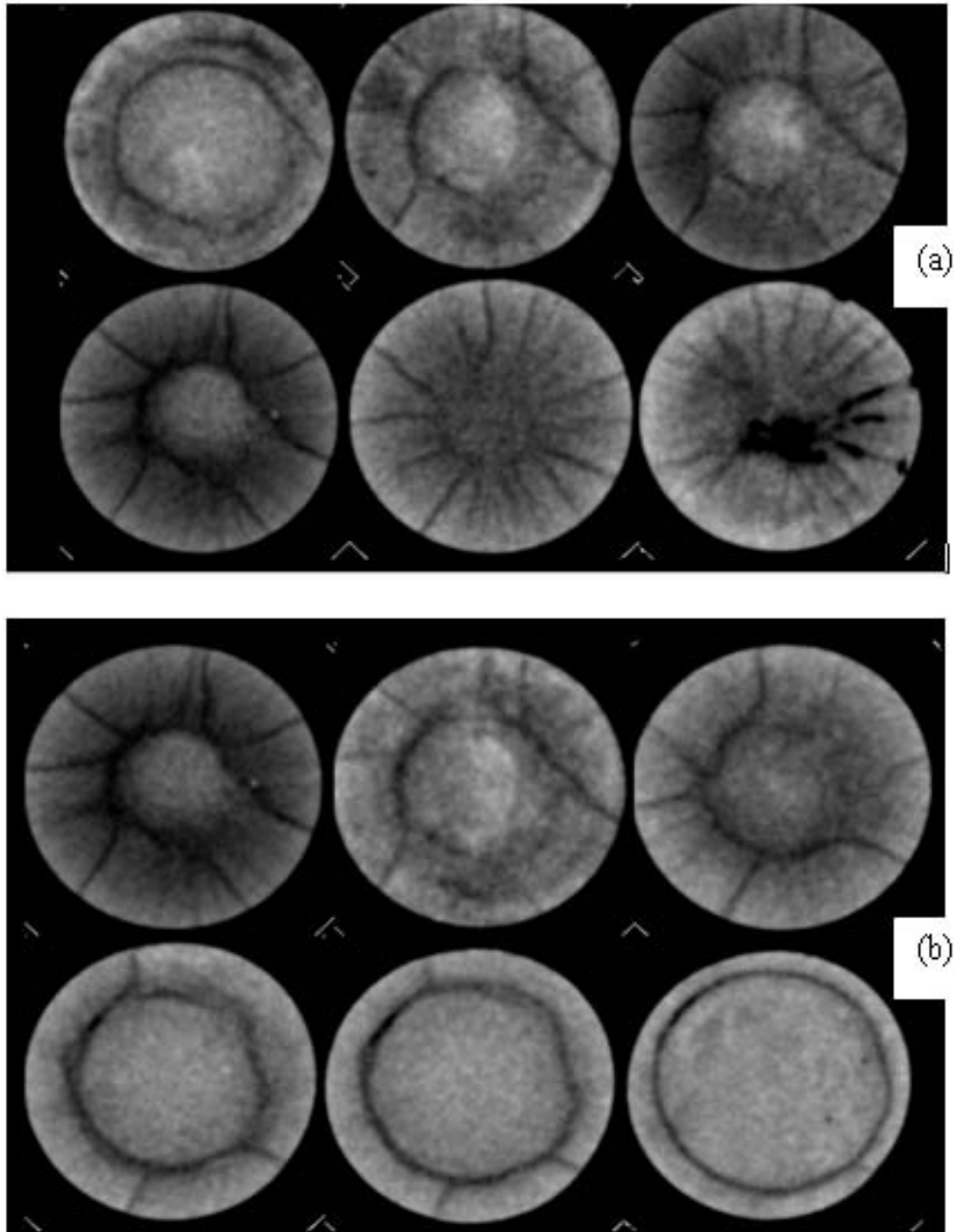


Figure 3.26: Images from the radial extension tests on Lower Fine Ottawa with constant 200 psi axial stress and decreasing confining stress. (a) The pictures show the change in fracture pattern when moving from top of the sample to the middle of the sand sample. Fractures are wider than the fractures which develop in triaxial compression tests. (b) The pictures show the change in fracture pattern when moving from top of the sample to the middle of the sand sample. Fractures are wider than the fractures which develop in triaxial compression tests.

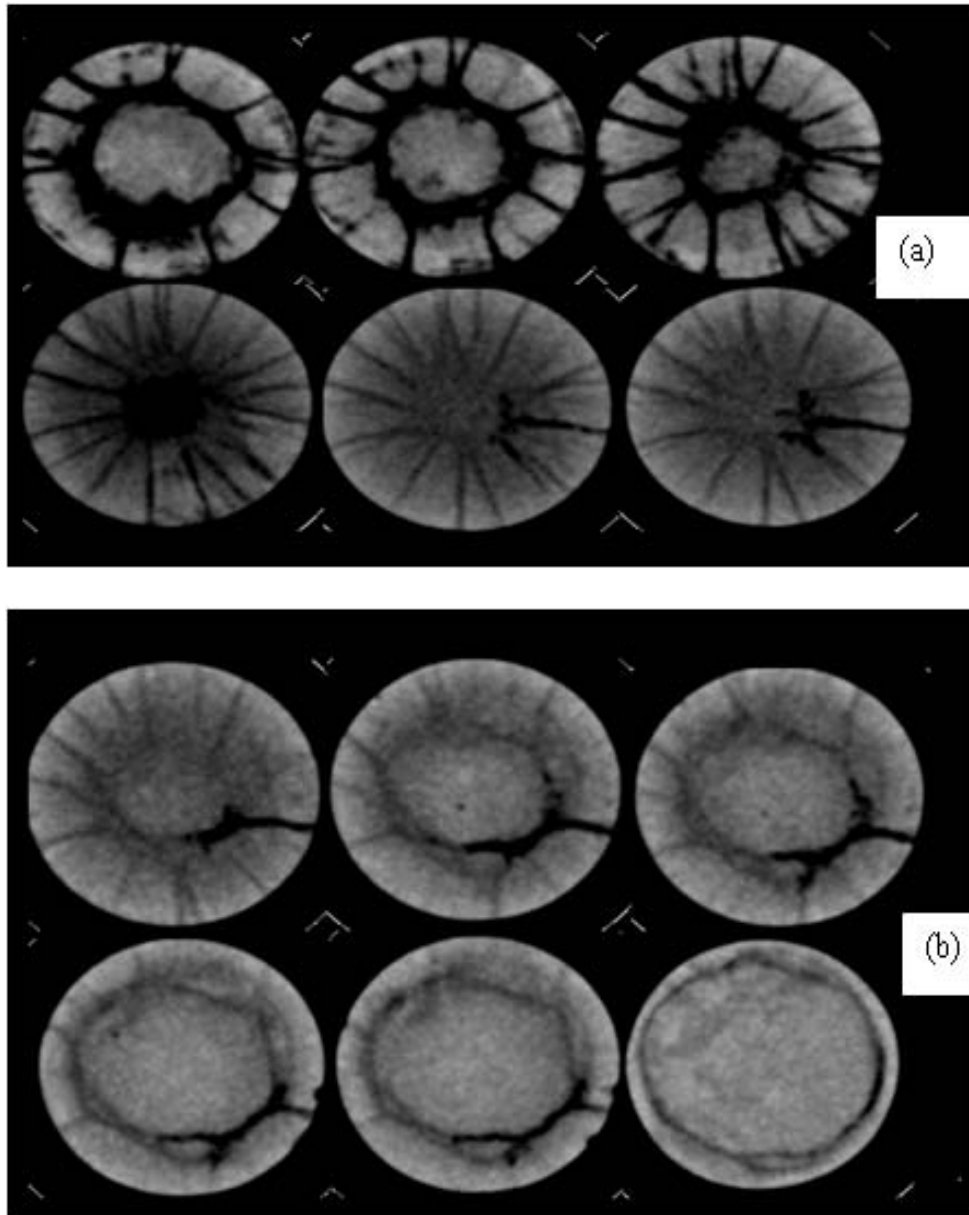


Figure 3.27: Images from the radial extension tests on Lower Fine Ottawa with constant 500 psi axial stress and decreasing confining stress. (a) The pictures show the change in fracture pattern when moving from top of the sample to the middle of the sand sample. Fractures are wider than the fractures which develop in triaxial compression tests. (b) The pictures show the change in fracture pattern when moving from middle of the sample to the bottom of the sand sample. Fractures are wider than the fractures which develop in triaxial compression.

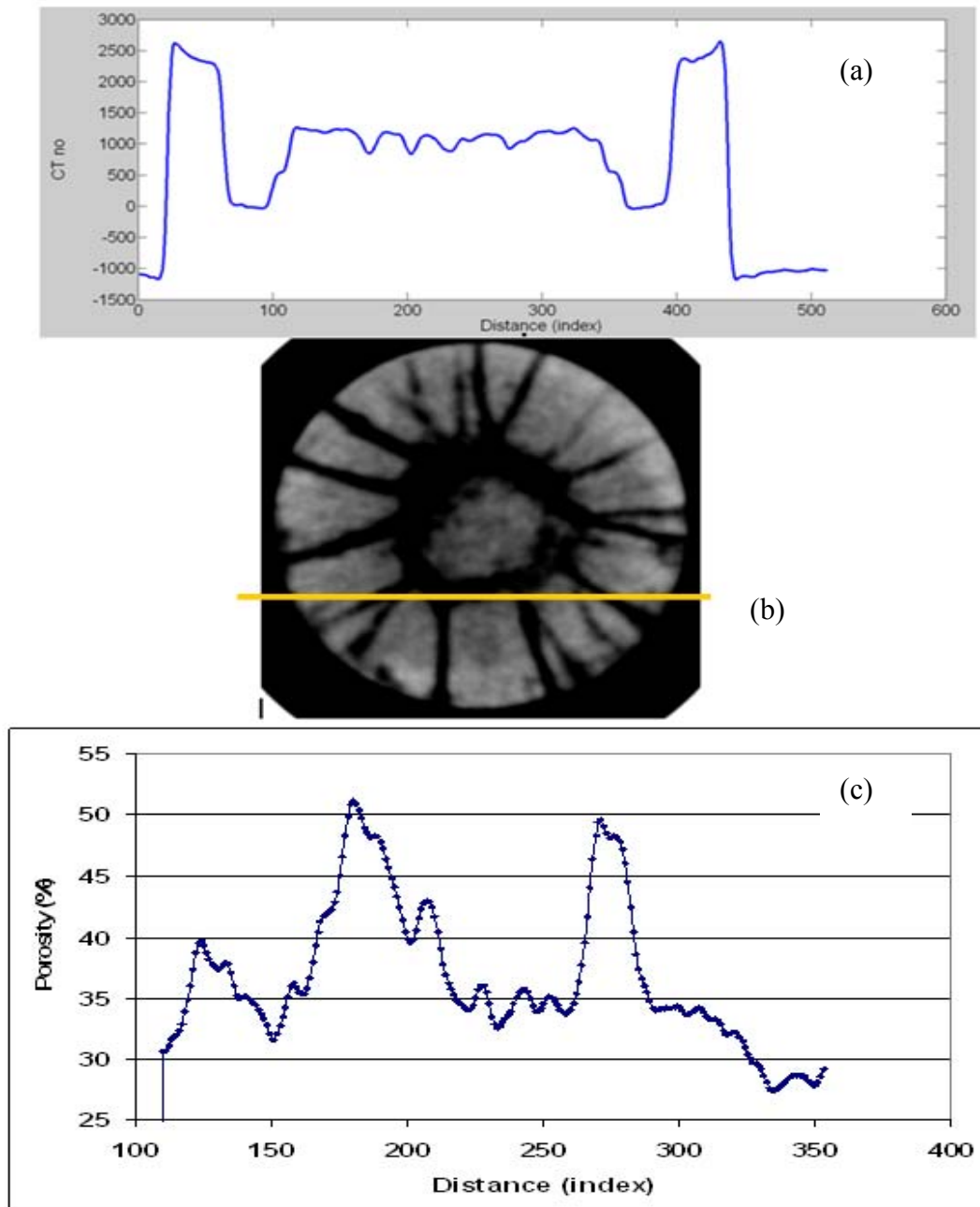


Figure 3.28: Radial extension test with 500 psi constant axial stress (image slice taken from the middle of the sample) (a) CT number variation along the traverse. (b) Image of the slice along with the traverse (yellow line). (c) Porosity analysis for a slice from the middle of the sample. The humps in porosity curve denote the porosity of the deformation bands.

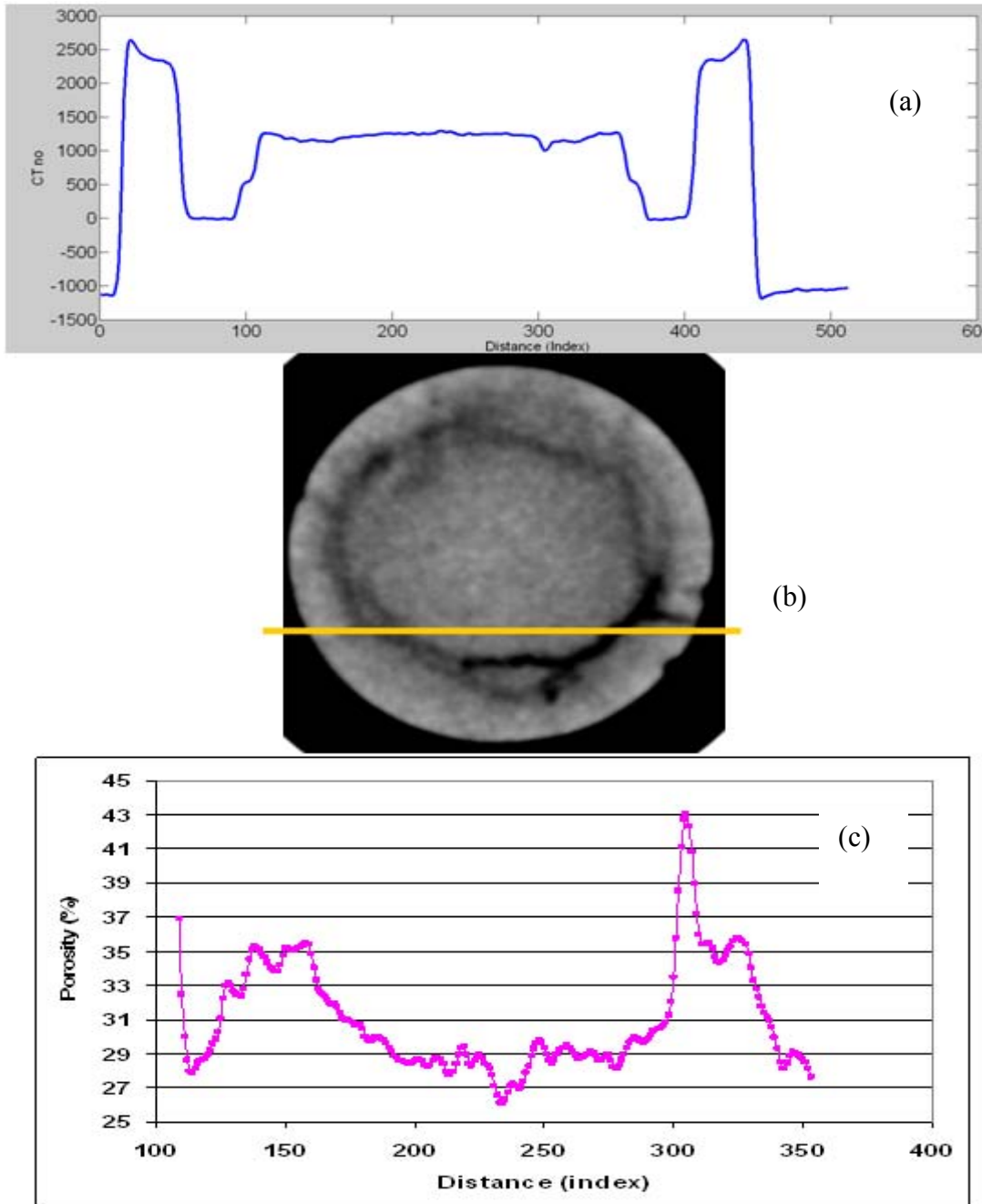


Figure 3.29: Radial extension test with 500 psi constant axial stress (image slice taken from the bottom of the sample) (a) CT number variation along the traverse. (b) Image of the slice along with the traverse (yellow line). (c) Porosity analysis for a slice from the middle of the sample. The humps in porosity curve denote the porosity of the deformation bands.

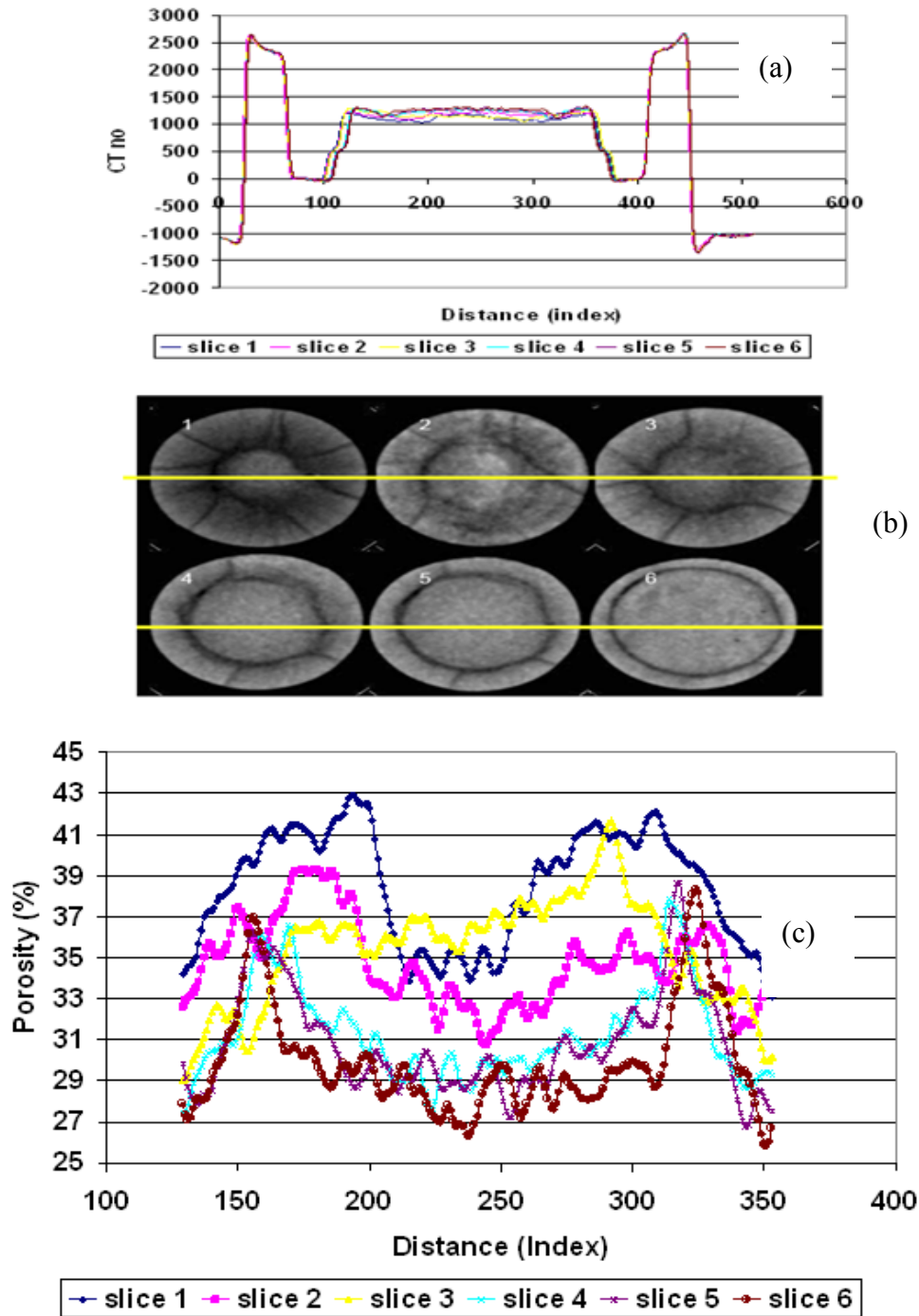


Figure 3.30: Triaxial compression test with 200 psi constant confining stress (a) CT number variation along the traverse for the slices. (b) Image of the slices along with the traverse (yellow line). (c) Porosity analysis for a slice from the middle of the sample. The humps in porosity curve denote the porosity of the deformation bands.

CHAPTER 4

Summary and Conclusions

Laboratory deformation of uncemented sand samples at low confining stress showed advantageous increases in absolute and relative permeabilities caused by localized shearing under dilatant volumetric strain conditions. In addition, associated residual oil saturation reduction caused by dilatant behavior would also be beneficial for recovery operations, indicating shear deformation could result in improved oil recovery factors.

Absolute permeability measurements during triaxial loading at 50 psi confining stress showed decreasing permeability until about 2-3% axial strain, after which volumetric strain became dilatant and absolute permeabilities increased at most by 20%. End point K_{ro} showed a maximum of 25% decrease during compaction and a 12% increase during dilation. S_{or} increased (18%) during compaction and decreased (21%) during dilation. Interestingly, the permeability and relative permeability enhancement seen at 50 psi in the triaxial tests was suppressed by increasing the confining stress to 200 psi, even though dilatant volumetric strain was still achieved for the higher confining stress.

Radial extension tests performed with a constant axial stress of 200 psi showed dilatant volumetric strain from the very beginning of deformation, and absolute permeability was immediately enhanced, reaching peak enhancements of 50% over initial values. End point K_{ro} showed a maximum of 40% increase and S_{or} also showed a decrease of 40% at 10% axial strain. The permeability enhancement seen at 200 psi axial

stress in the radial extension test was higher as compared to the tests done with 500 psi axial stress.

CT scans of the deformed sand samples indicated localized shear deformation along discrete, high porosity bands with radial symmetry. The porosity in the deformation bands was as much as 50% higher than the less deformed surrounding sand pack.

4.1 FIELD APPLICATIONS

In shallow unconsolidated sand reservoirs, an increase in the horizontal stresses can be experienced due to the thermal expansion of the reservoir. The increase in the horizontal stresses may be more than the decrease in the vertical stresses (due to increase in pore pressure). Thus, the geotechnical response of the sand reservoir under these conditions would be similar to the triaxial compression tests where a path of mean increasing stress is followed. Triaxial compression tests showed a decrease of up to 25% in K_{ro} and an increase in S_{or} (about 35%). In a loose sand reservoir under going compaction an increase in S_{or} and a decrease in relative permeability can be expected, leading to lower recovery factors from that reservoir.

Path of decreasing mean stress is followed during steam injection into loose sand reservoirs and is similar to the radial extension test. Decrease in residual oil saturation in radial extension tests is as much as 40% at 10% axial strain. A lower residual oil saturation can be expected in reservoirs which experience dilation due to steam injection, resulting in a higher recovery factor. Radial extension tests also show an increase in relative permeability values (up to 50%) which can also help improve recovery.

A thorough understanding of how shear dilatancy affects the relative permeability to oil and water may lead to development of better simulation models that can reproduce the complex interaction between geomechanics and fluid flow in unconsolidated heavy

oil sand reservoirs. A geomechanical model capable of coupling the change in relative permeability and residual oil saturation can lead to more realistic models that can help improve recovery factors from heavy oil reservoirs.

4.2 FUTURE RESEARCH AND RECOMMENDATIONS

The study investigated the change in permeability, relative permeability and residual oil saturation with stress in unconsolidated sands. Oil and water were used for unsteady state experiments. Using steam instead of water in the experiments to displace oil can emulate the real SAGD conditions giving a better idea of the change in relative permeability to multiple phases flowing in the reservoir.

Secondly using real heavy oil sands that are already oil or bitumen saturated can allow a more realistic experimentation that will represent conditions that are much closer to the conditions existing in heavy oil sand reservoirs.

SAGD causes an increase in pore pressure of the reservoir. Radial extension tests mimic increasing pore pressure by following a path of mean decreasing stress. However actual increases in pore pressure may lead to a higher increase in permeability and consequently the relative permeability change. Therefore, future experiments can be run with pore pressure present in the sand sample.

Saturation and relative permeability studies using a CT scanner is another method of quantifying the changes in petrophysical parameters of the failed sand packs and can also be used for a similar study.

Appendix A: Grain Size Details

Mean grain diameter along with the coefficient of variation (CV) was used to characterize the sand properties. The coefficient of variation is defined as the ratio of standard deviation to mean and is useful in understanding the standard deviation in the context of mean, when the mean varies widely such as in the case of mean grain diameter of sands used in this investigation. Therefore in comparing the properties of sands such as the permeability, the CV can be used instead of the standard deviation for comparison. Samples with CV less than one are considered to have low variance.

Medium Ottawa was the coarsest sand used in the experiments and a histogram plot showed a higher percentage of coarser grains in the sand (Figure A1). It had a mean grain size of 435 microns and a CV of .37. It is well sorted clean sand. Lower Fine Ottawa had a mean grain diameter of 201 microns and a CV of .6. The sand was well sorted but had a higher percentage of the lower diameter grains (Figure A2). It was the finest of the sands used for these experiments. Lower Amalgamated Ottawa sand (LA) was a mixture of Lower Fine Ottawa and Medium Ottawa sands. From the grain size distribution (Figure A3), it had a uniform distribution of fine and coarse grains. The mean grain size diameter for the sand was 300 microns and a CV of .34.

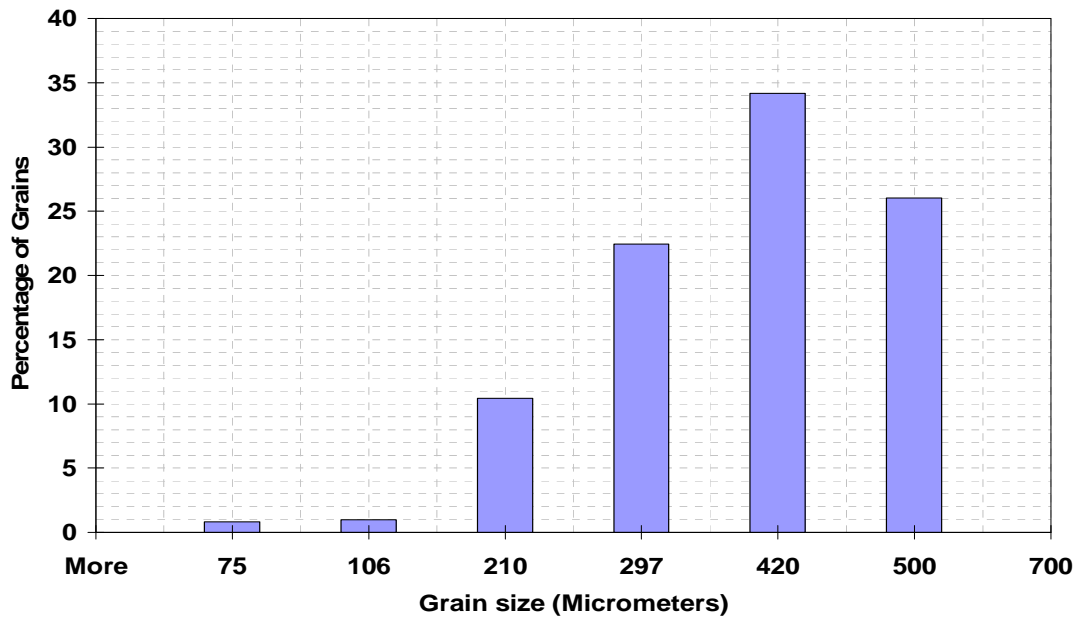


Figure A1: Grain size distribution of the Medium Ottawa .

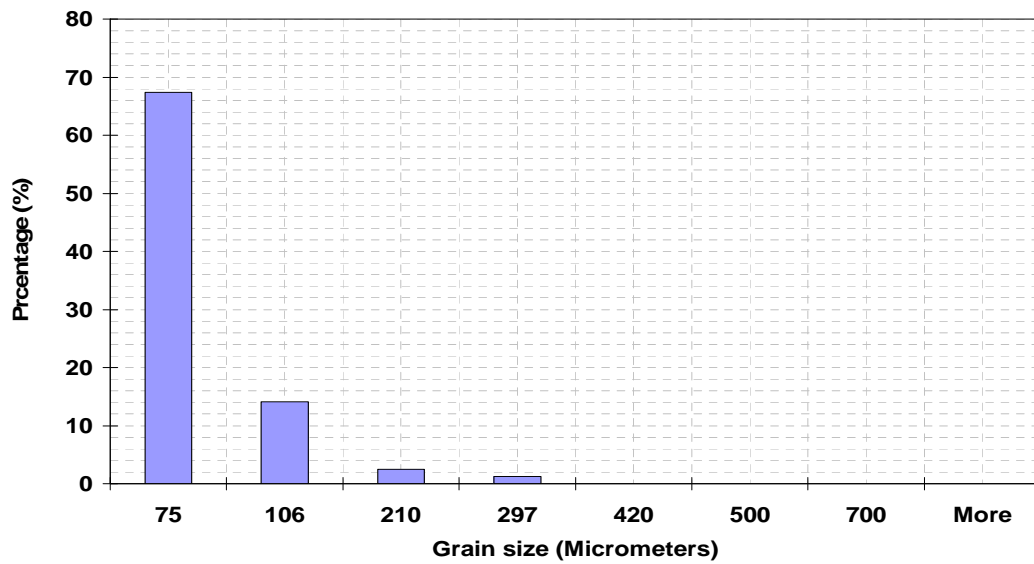


Figure A2: Grain size distribution of the Lower Fine Ottawa .

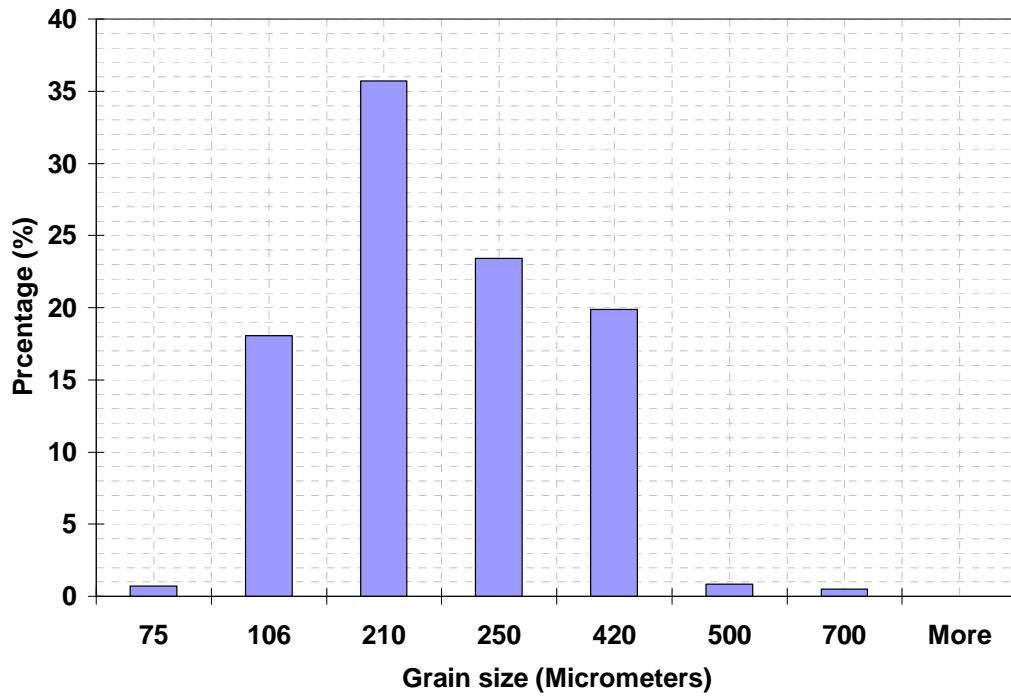


Figure A3: Grain size distribution of the Lower Amalgamated Ottawa (LA).

Appendix B: Stress-Strain and Volumetric Strain curves

This Appendix contains the stress-strain and volumetric strain curves for the sand samples in triaxial compression (Figure B1-B6) and radial extension (Figure B7-B16) tests. The deformation was stopped after reaching the desired value of axial strain (1%, 2%, 3%, 5% and 10%) and permeability and relative permeability measurements were carried out.

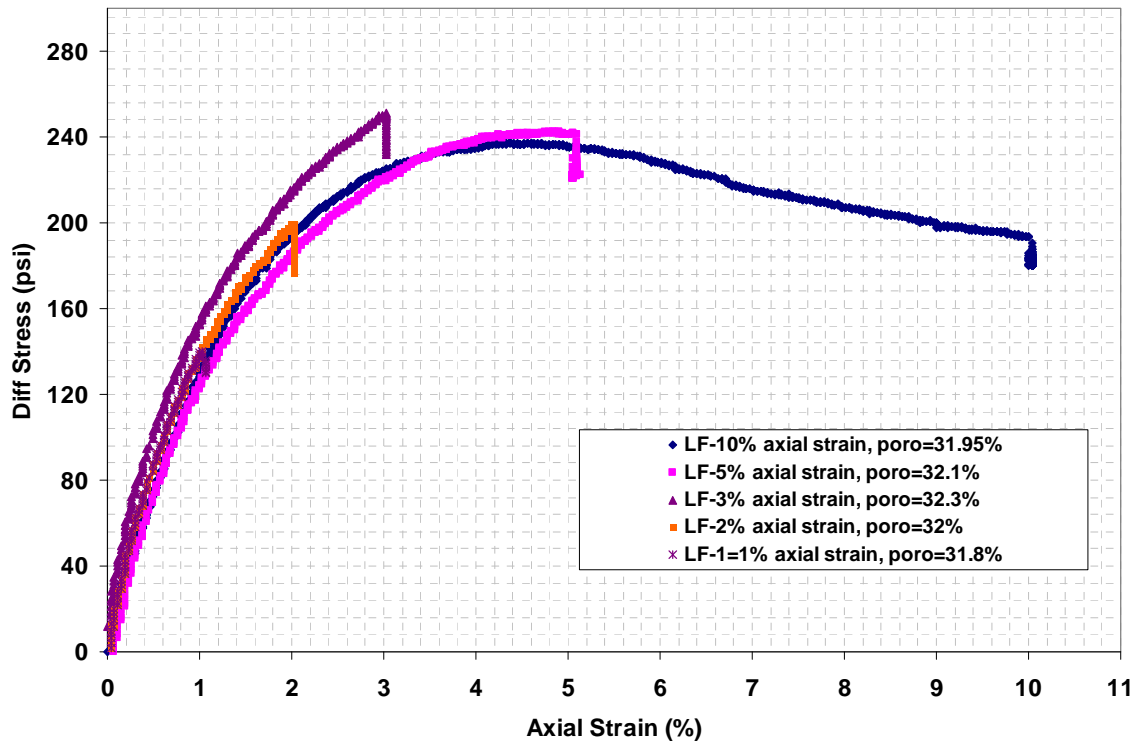


Figure B1: Stress strain curves in triaxial compression (at 2%, 3%, 5% and 10% axial strain) for Lower Fine Ottawa (LF) samples tested with 50 psi confining stress.

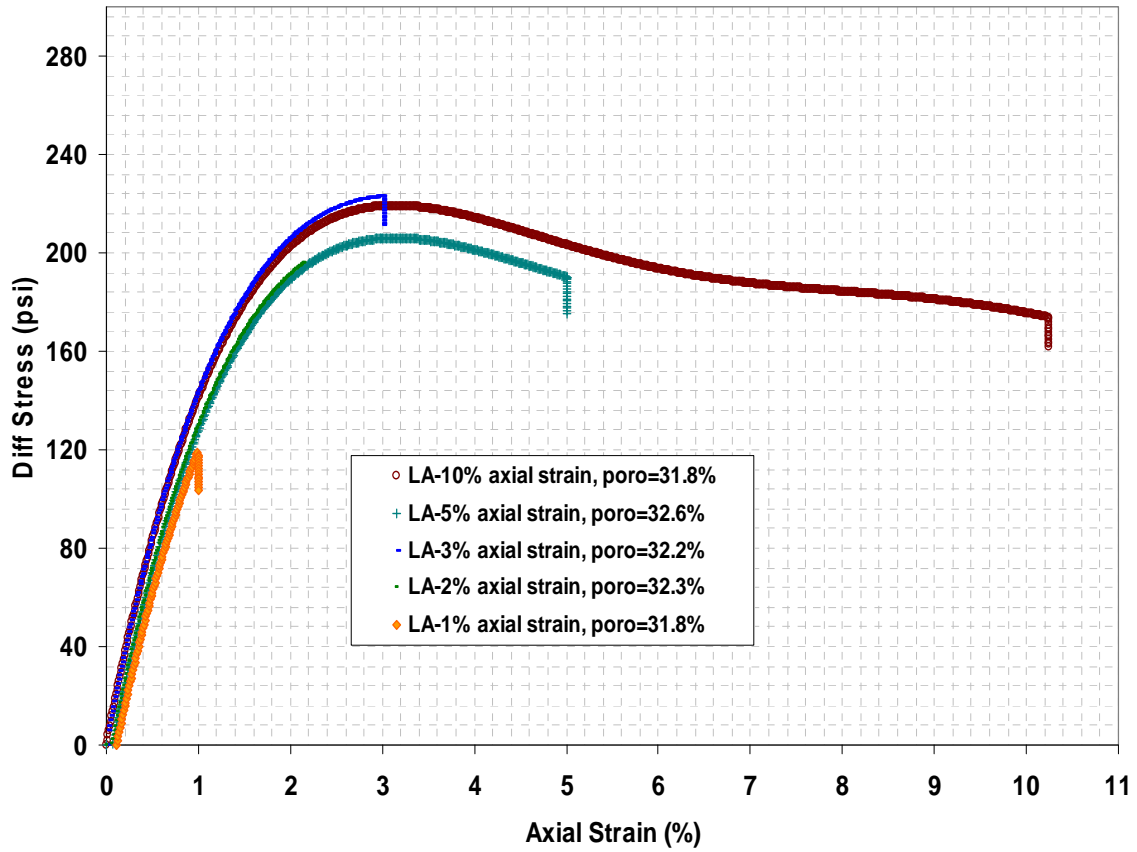


Figure B2: Stress strain curves in triaxial compression (at 2%, 3%, 5% and 10% axial strain) for Lower Amalgamated Ottawa (LA) samples tested with 50 psi confining stress.

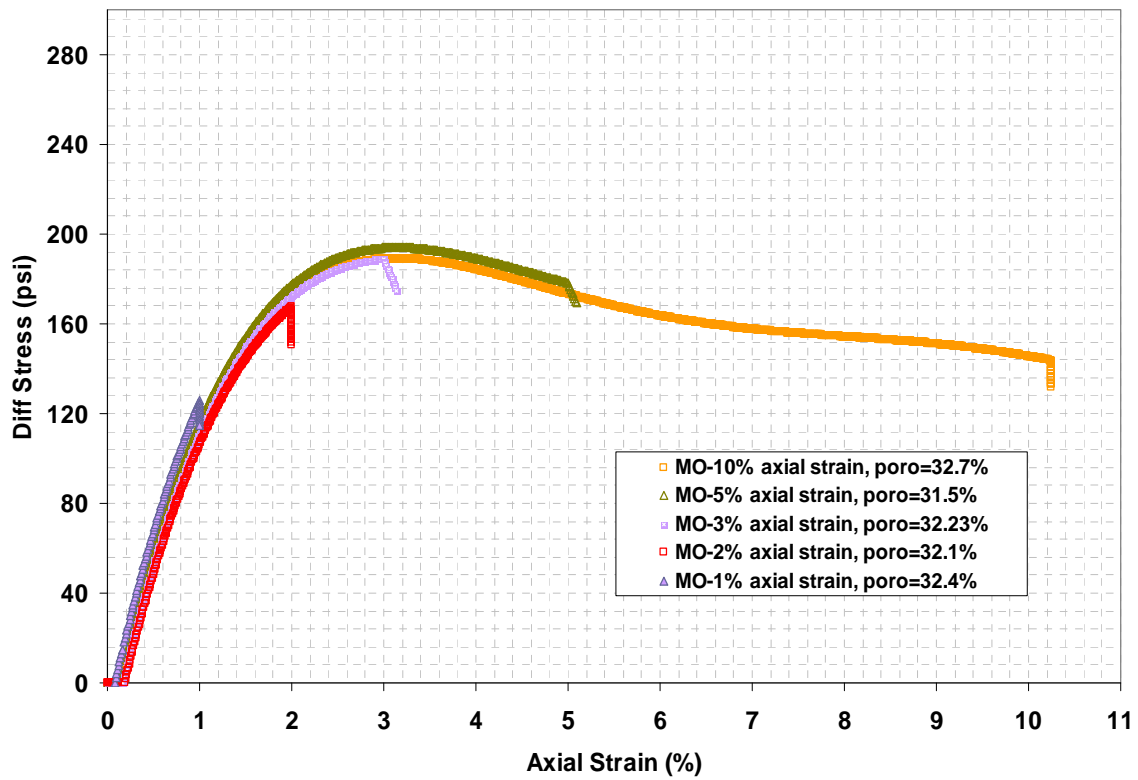


Figure B3: Stress strain curves in triaxial compression (at 1%, 2%, 3%, 5% and 10% axial strain) for Medium Ottawa (MO) samples tested with 50 psi confining stress.

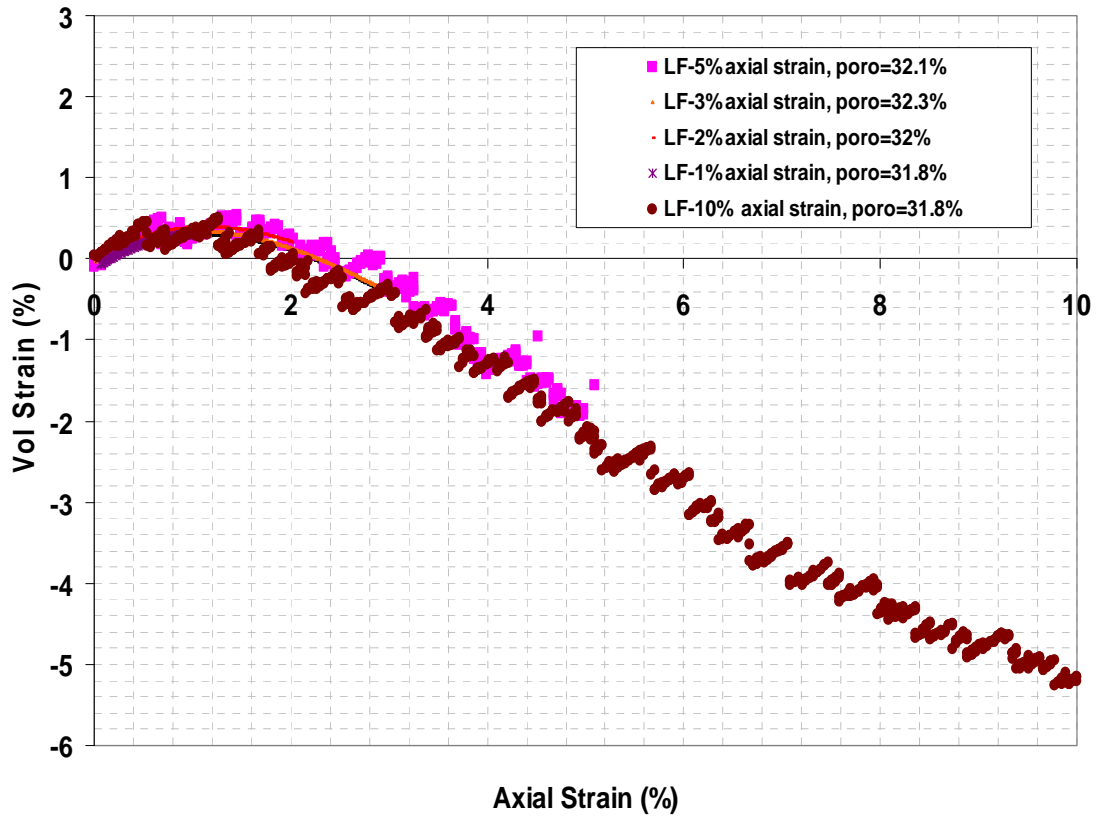


Figure B4: Volumetric strain in triaxial compression tests (at 1%, 2%, 3%, 5% and 10% axial strain) for Lower Fine Ottawa (LF) done with 50 psi confining pressure.

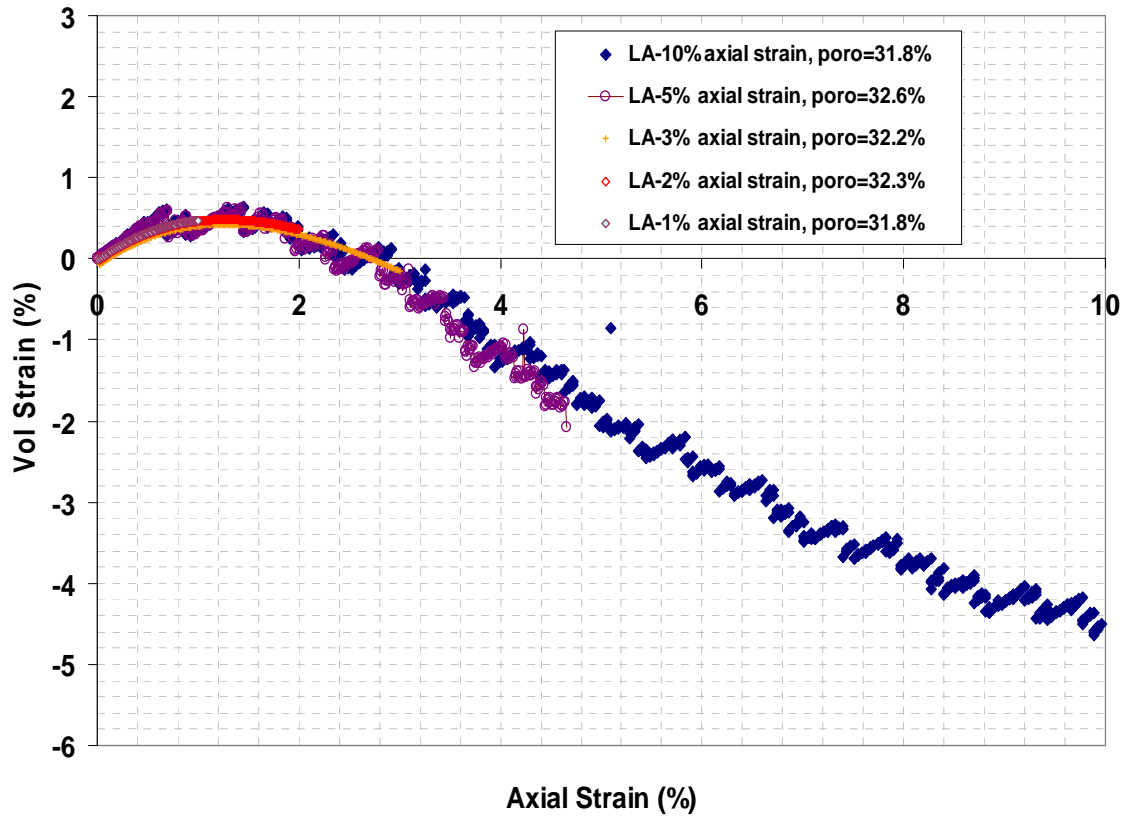


Figure B5: Volumetric strain in triaxial compression tests (at 1%, 2%, 3%, 5% and 10% axial strain) for Lower Amalgamated Ottawa (LA) done with 50 psi confining pressure.

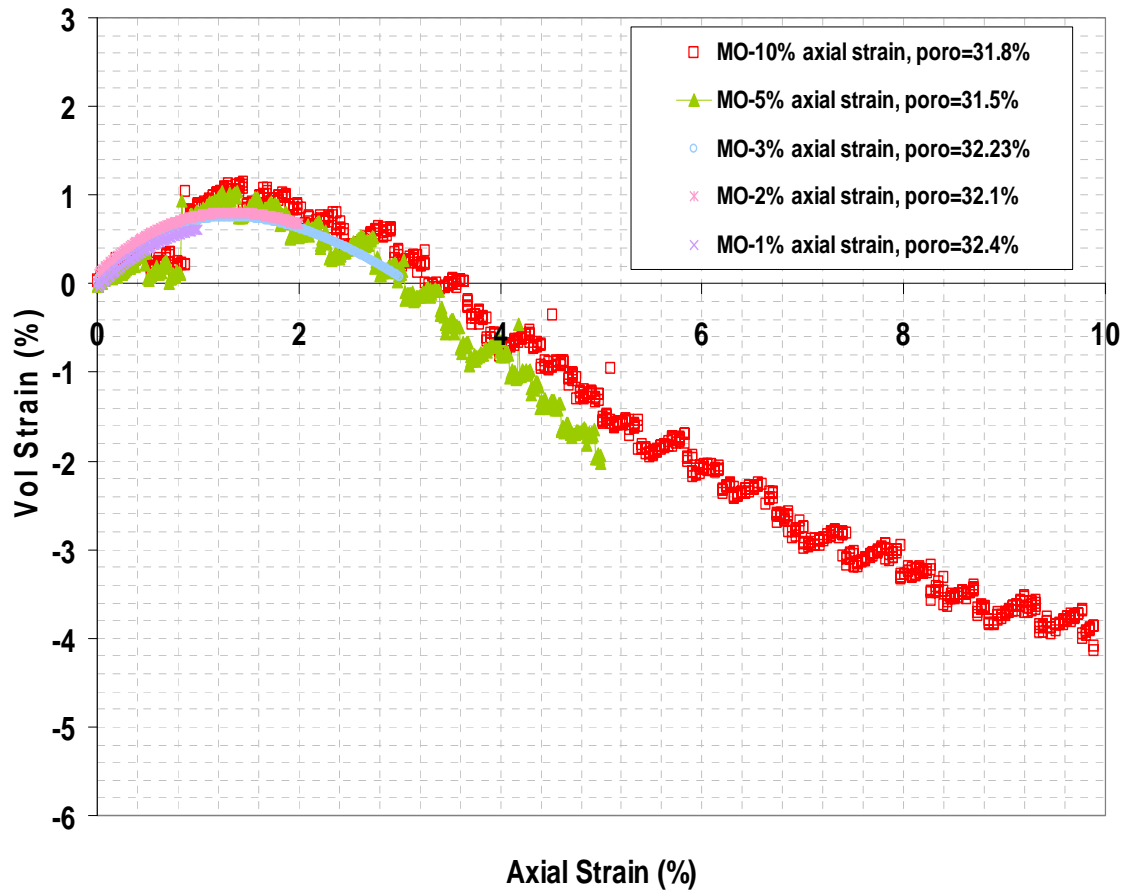


Figure B6: Volumetric strain in triaxial compression tests (at 1%, 2%, 3%, 5% and 10% axial strain) for Medium Ottawa (MO) done with 50 psi confining pressure.

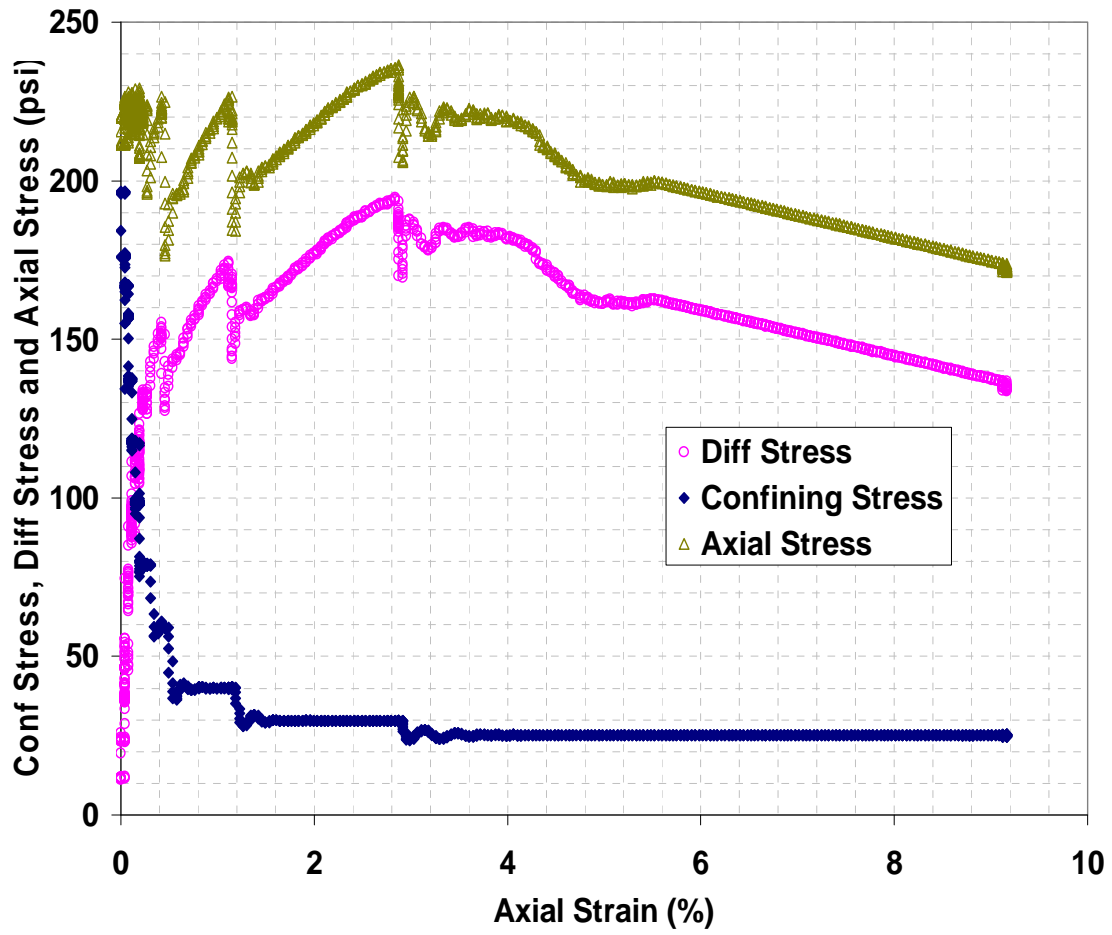


Figure B7: Differential stress, confining stress and axial stress plotted against axial strain for Lower Fine Ottawa Specimens with 200 psi constant axial stress.

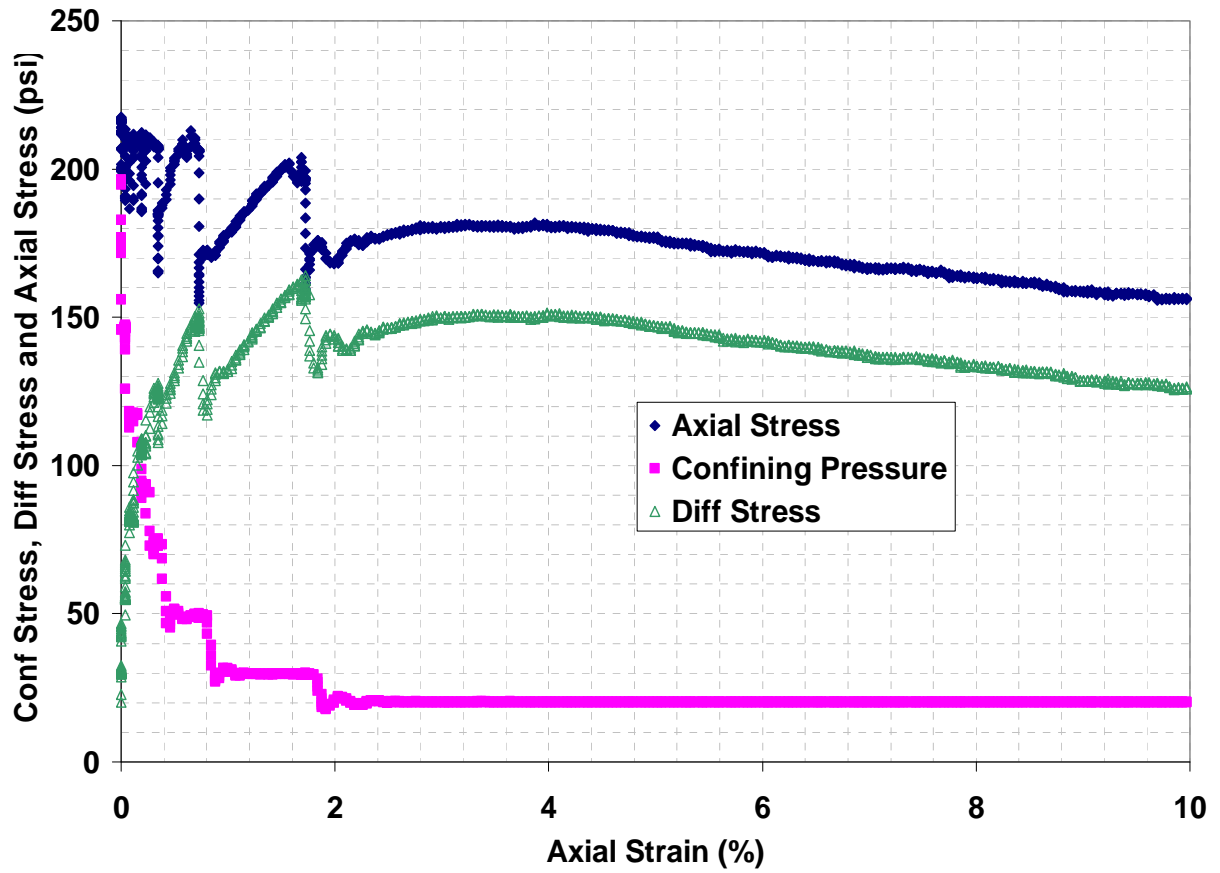


Figure B8: Differential stress, confining stress and axial stress plotted against axial strain for Lower Amalgamated Ottawa Specimens with 200 psi constant axial stress.

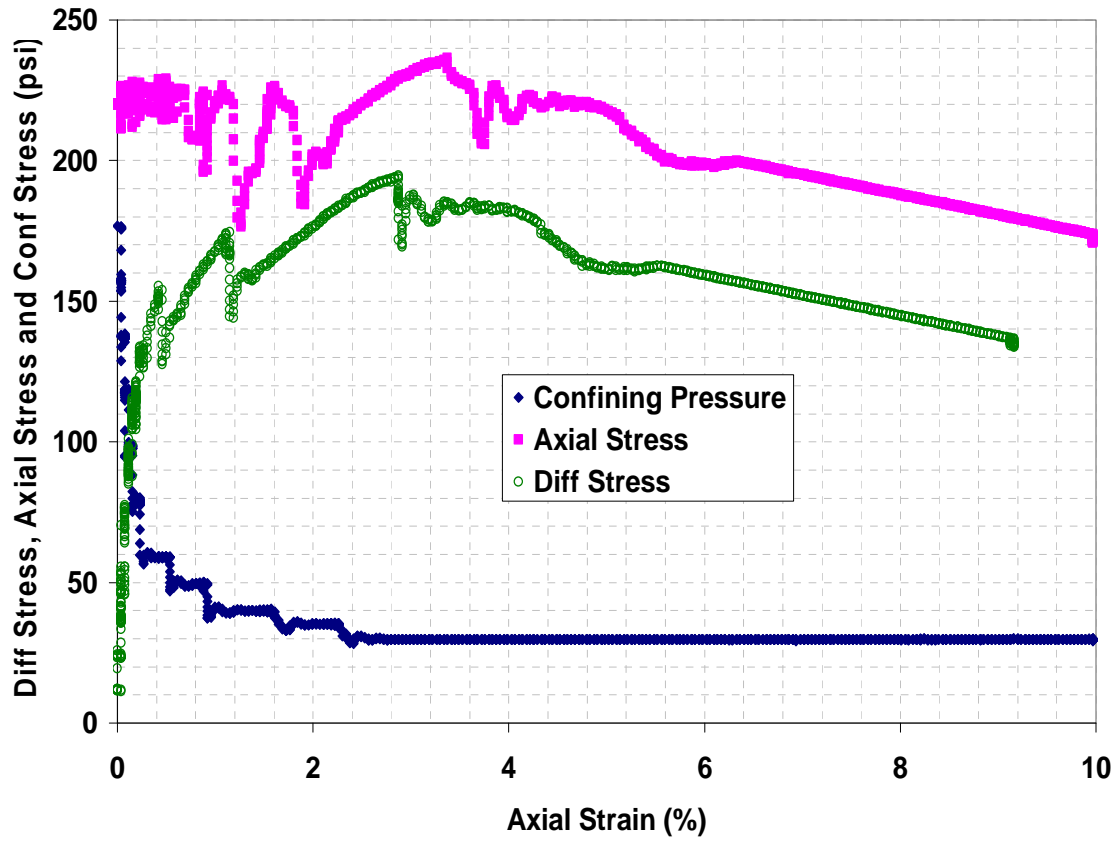


Figure B9: Differential stress, confining stress and axial stress plotted against axial strain for Medium Ottawa Specimens with 200 psi constant axial stress.

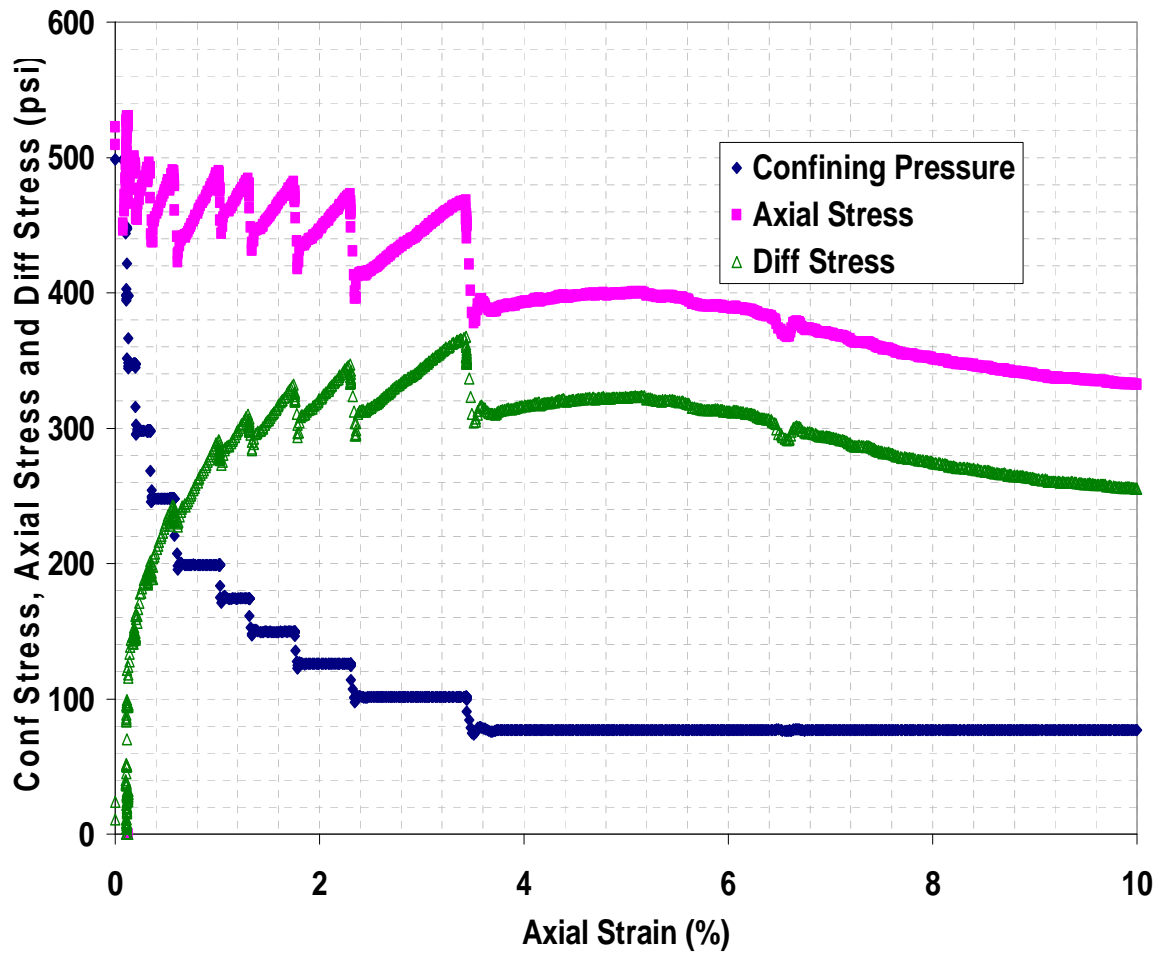


Figure B10: Differential stress, confining stress and axial stress plotted against axial strain for Lower FineOttawa Specimens with 500 psi constant axial stress.

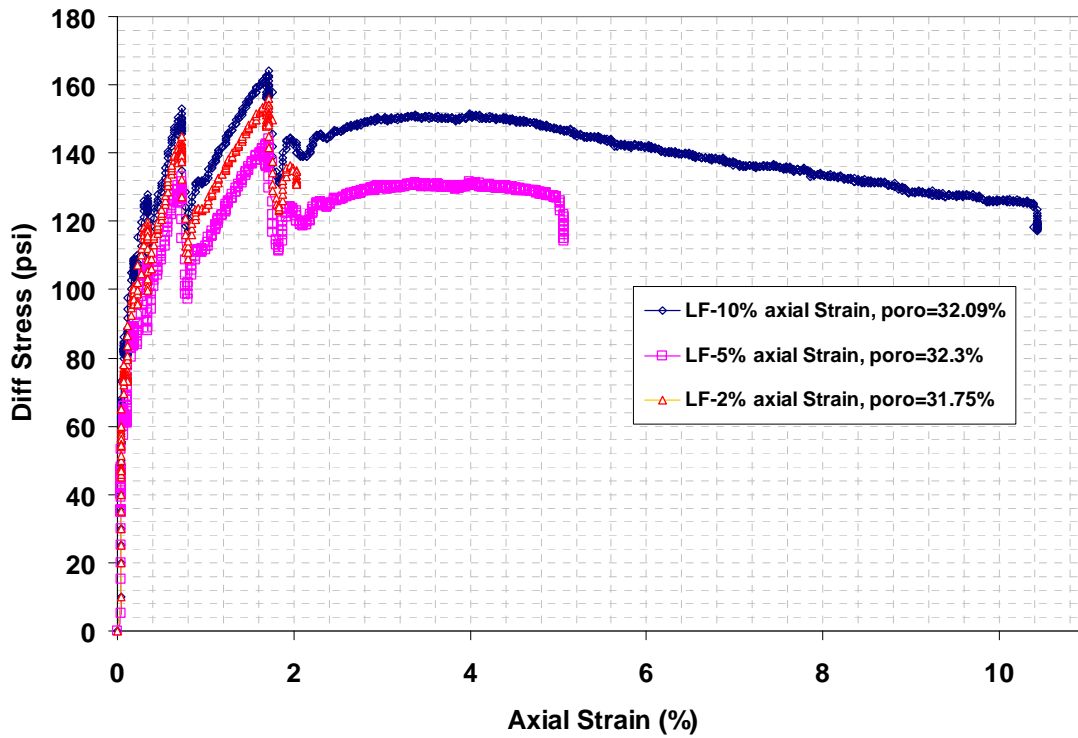


Figure B11: Stress-strain curves for radial extension tests (at 2%, 5% and 10% axial strain) for Lower Fine Ottawa (LF) with constant axial stress of 200 psi and decreasing radial stress.

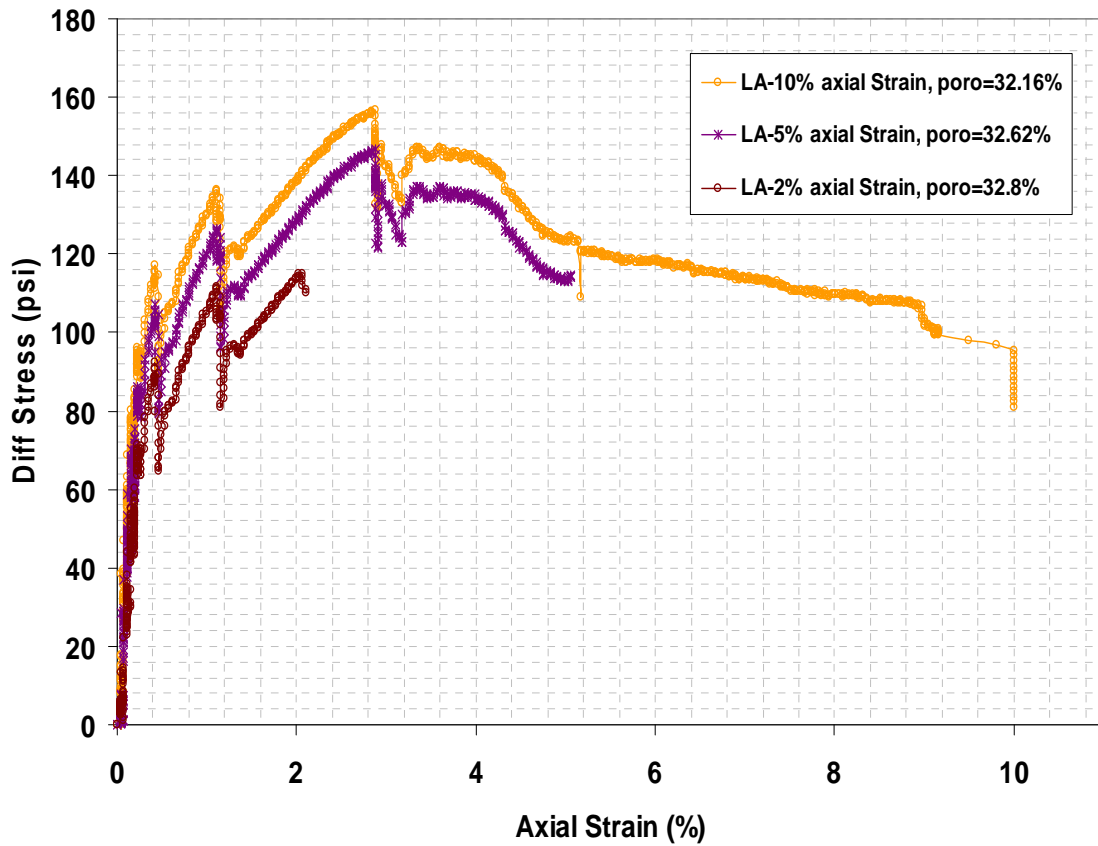


Figure B12: Stress-strain curves for radial extension (at 2%, 5% and 10% axial strain) tests for Lower Amalgamated Ottawa (LA) with constant axial stress of 200 psi and decreasing radial stress.

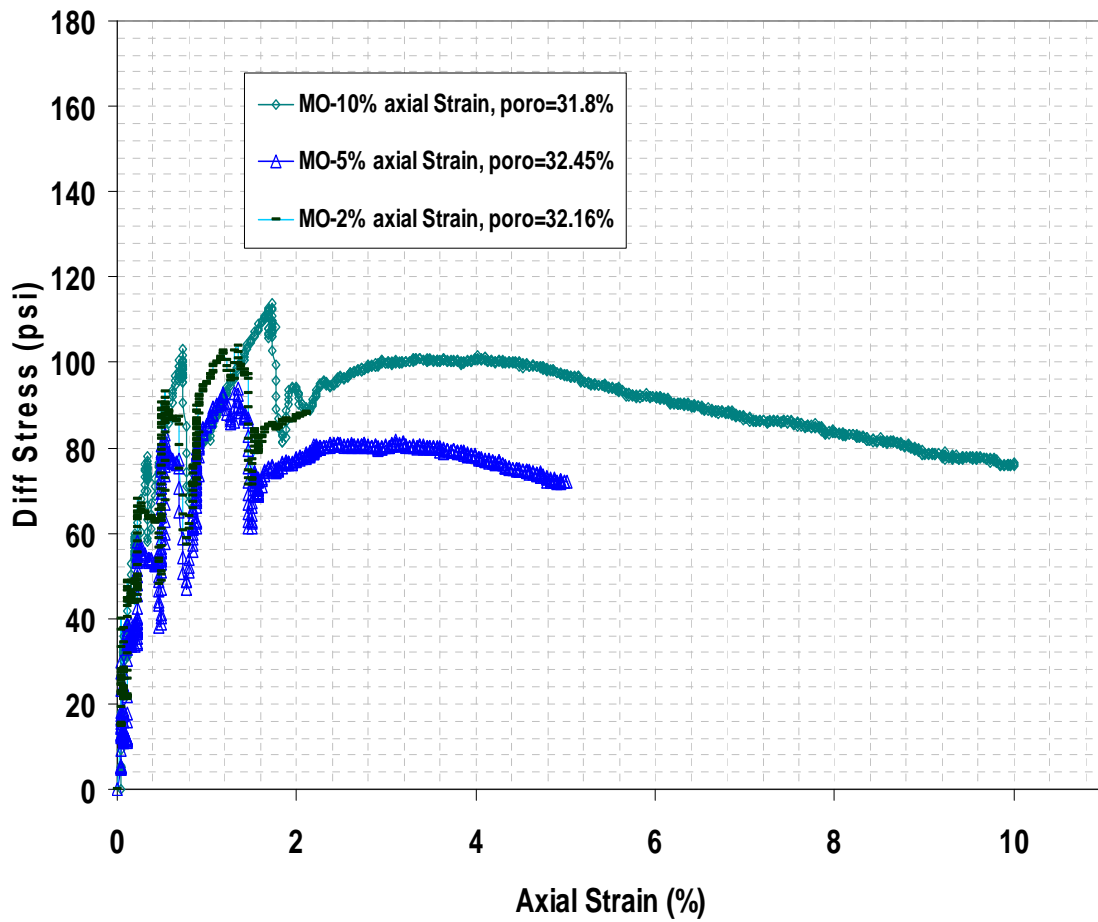


Figure B13: Stress-strain curves for radial extension tests (at 2%, 5% and 10% axial strain) for Medium Ottawa (MO) with constant axial stress of 200 psi and decreasing radial stress.

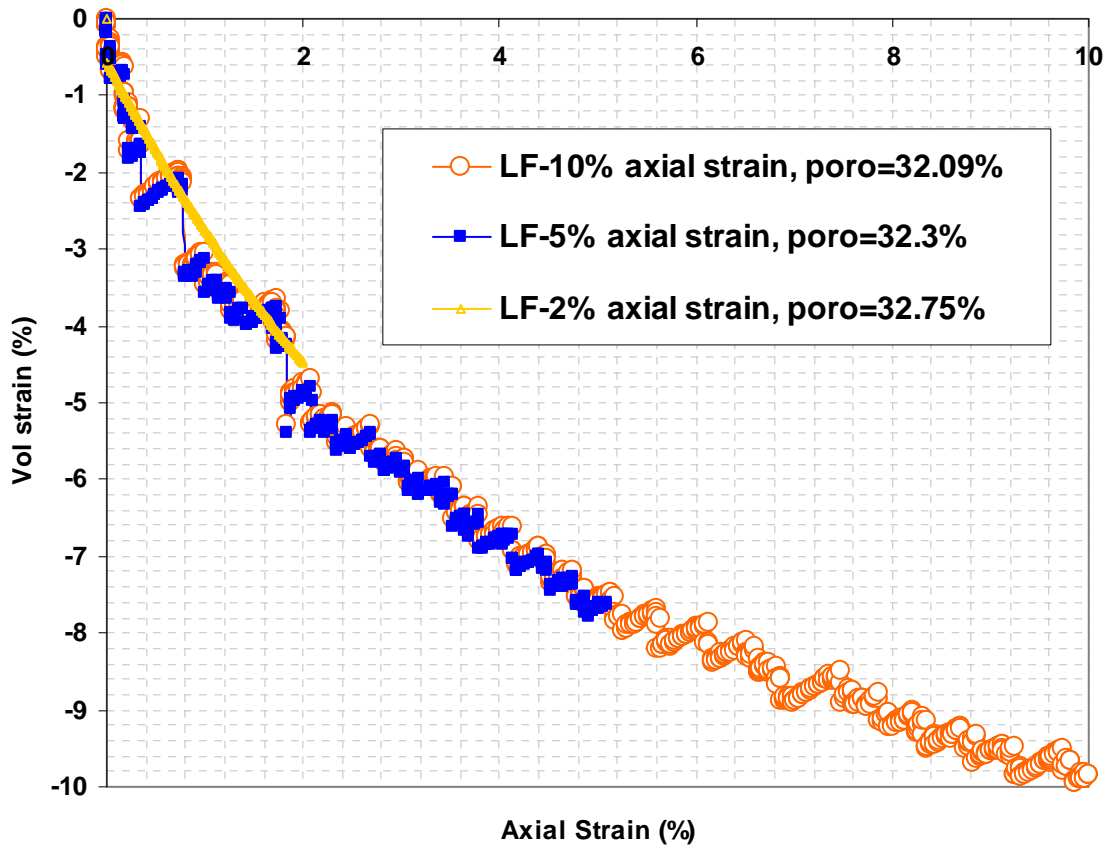


Figure B14: Volumetric strain curves for radial extension tests (at 2%, 5% and 10% axial strain) for Lower Fine Ottawa (LF) with constant axial stress of 200 and decreasing confining stress.

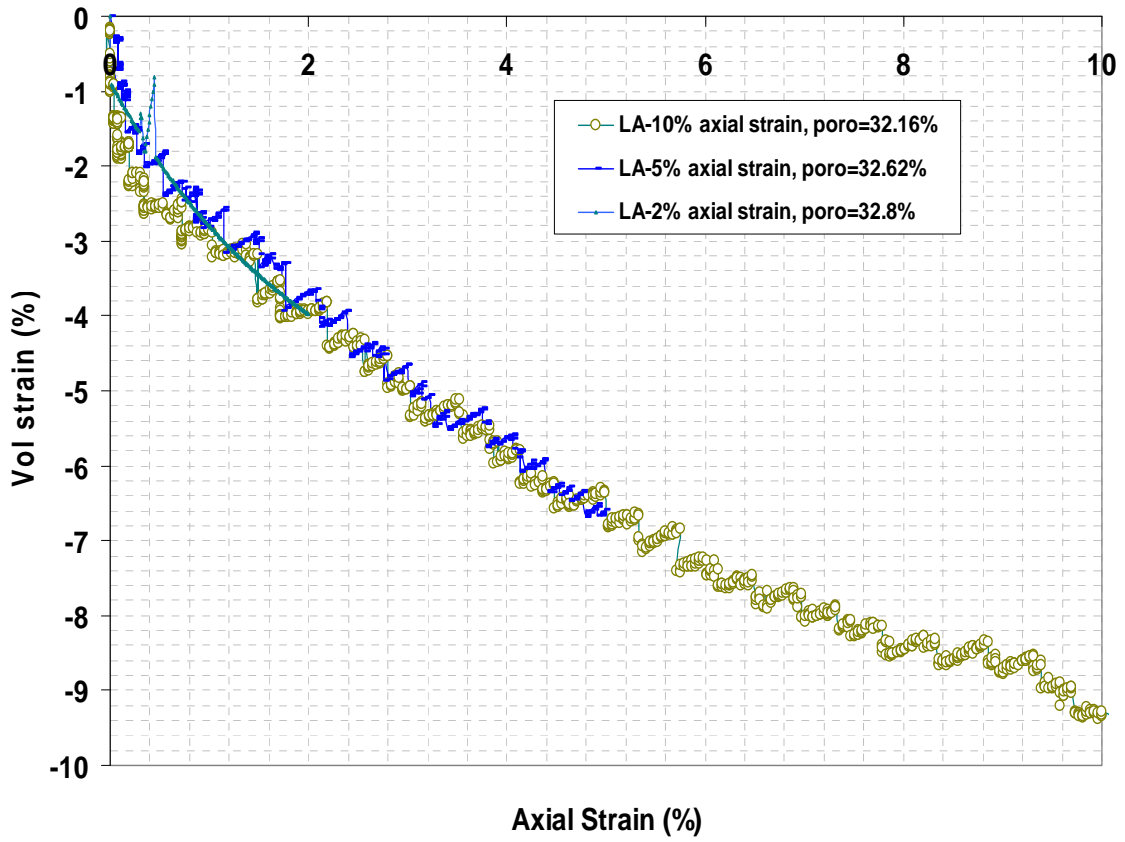


Figure B15: Volumetric strain curves for radial extension tests (at 2%, 5% and 10% axial strain) for Lower Amalgamated Ottawa (LA) with constant axial stress of 200 and decreasing confining stress

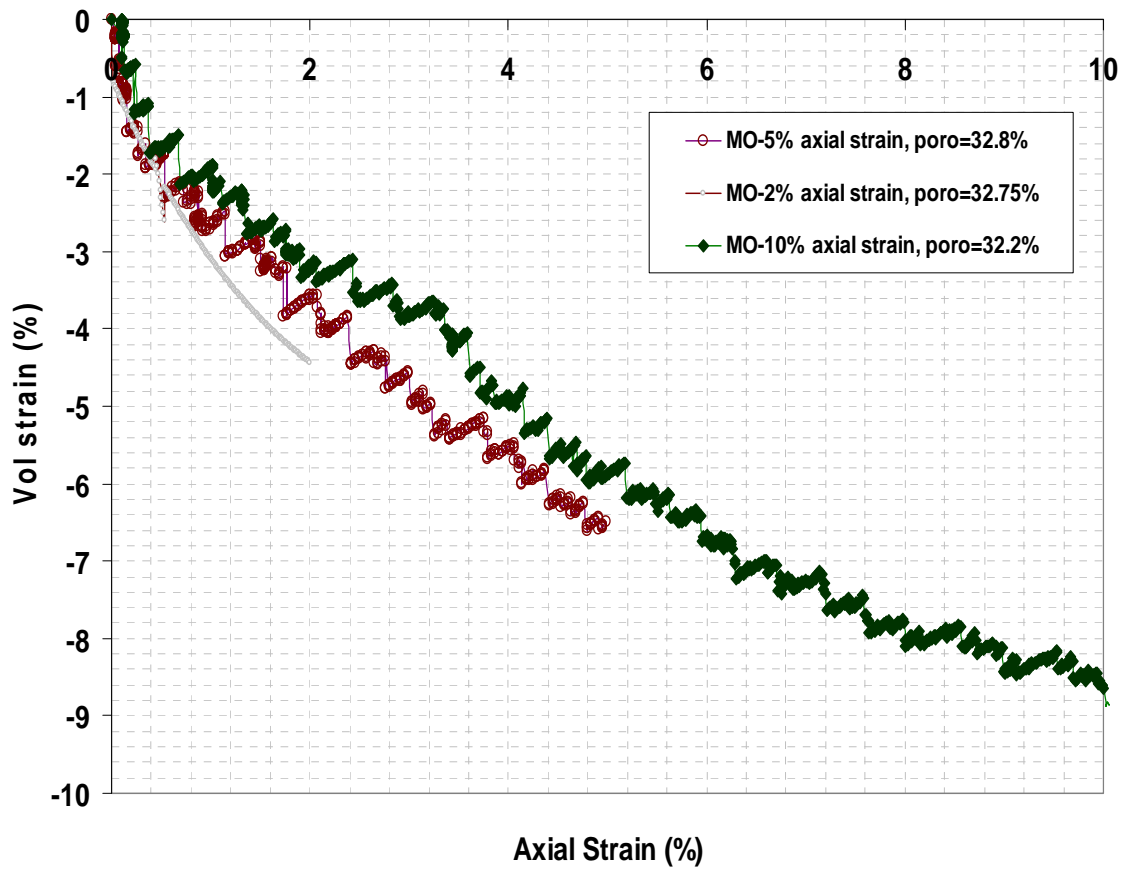


Figure B16: Volumetric strain curves for radial extension tests (at 2%, 5% and 10% axial strain) for Medium Ottawa (MO) with constant axial stress of 200 and decreasing confining stress.

References

- Albahlani, A.M., and Babadagli, T. 2008. A Critical Review of the Status of SAGD: Where are we and What is next?. SPE 113283 presented at the SPE West/AAPG Pacific Section Joint Meeting, Bakersfield, California, USA, 31 March-2 April.
- Agar, J.R. 1984. Geotechnical behavior of Sands at Elevated Temperatures and Pressure. Ph.D. Dissertation, U of Alberta, Edmonton, Alberta.
- Ali, H.S., Al-Marhoun, S.A., Abu-Khamsin and Celik, M.S. 1987. The Effect of Overburden Pressure on Relative Permeability. SPE 15730 presented at SPE Middle East Oil Show, Manama, Bahrain, 7-10 March.
- Ata, A., and Vipulanandan, C. 1999. Factors affecting mechanical and creep properties of silicate-grouted sands. *J. Geotech. Geoenviron. Eng.*, 125_10_, 868-876.
- Blanton, T.L., and Olson, J.E. 1999. Stress magnitudes from Logs: Effects of Tectonics Strain and temperature. *SPE Reservoir Eval & Eng.* 2 (1): 62-68.
- Butler, R.M. 1998. SAGD Comes of Age. *J. Cdn. Pet. Tech.* 37 (7): 9-12.
- Beard, D.C., and Weyl, P.K. 1973. Influence of texture on porosity and permeability of unconsolidated sand: *American Association of Petroleum Geologists Bulletin*, v. 57, p. 349-369.
- Buckley, S. E., and Leveret, M.C. 1942. Mechanism of Fluid Displacement in Sands. *Trans., AIME*, 146, 107.
- Bachu, S., and Undersultz, J. R. 1992. Regional-scale porosity and permeability variations, Peace River Arch area, Alberta, Canada. *AAPG Bulletin*, v. 76, p. 547-562.
- Collins, P.M., Carlson, M.R., Walters, D.A and Settari, A. 2002. Geomechanical and Thermal Reservoir Simulation Demonstrates SAGD Enhancement due to Shear Dilation. Paper. SPE/ISRM 78237 presented at the SPE/ISRM Rock Mechanics Conf. Irving, TX, 20-23 October.
- Collins, P.M. 2007. Geomechanical Effects on the SAGD Process. *SPE Reservoir Evaluation and Engineering*, August.
- Chalaturnyk, R and Scott, J.D. 1995. Geomechanics Issues of Steam Assisted Gravity Drainage. SPE 30280 presented at the SPE international Heavy Oil Symposium, Calgary, Alberta, 19-21 June.

- Chalaturnyk, R and Scott, J.D. 1997. Geomechanical Response of Heavy oil Reservoirs to the Steam Assisted gravity Drainage Process. SPE 37569 presented at the International Thermal operations and heavy Oil Symposium, California, USA, 10-12 February.
- Clark, Brian, Graves, W.G, Gurfinkel, M, Peats, A.W and Lopez-de-Cardenas, J.E. 2007. Heavy Oil. Working Document of the NPC Global Oil and Gas Study.
- Carman, P.C. 1937. Fluid flow through a granular bed, *Trans. Inst. Chem. Eng.* 15, pp.150–156.
- Desrues, J and Viggiani, G. 2004. Strain localization in Sand: An overview of the experimental results obtained in Grenoble using Stereophotogrammetry. *Int. J. Numer. Anal. Meth. Geomech* 28: 279-321.
- Dusseault, M.B and Morgenstern, N.R. 1979. Locked Sand. *Quarterly Journal of Engineering Geology and Hydrogeology* 12 (2): 117-131.
- Dusseault, M.B. 1977. The geotechnical Characteristics of Athabasca oil Sands. Ph.D. Dissertation, U of Alberta, Edmonton, Alberta.
- Chalaturnyk, R. 1996. Geomechanics of the Steam Assisted Gravity Drainage Process in Heavy Oil Reservoirs. Ph.D. Dissertation, U of Alberta, Edmonton, Alberta.
- Fatt, I. and Davis, D.H. 1952. Reduction in Permeability with Overburden Pressure. *Trans., AIME*, 195, 329.
- Fatt, I. 1953. The Effect of Overburden Pressure on relative permeability. *Trans, AIME*, 198, 325.
- Fossen, Hakoon., and Arthur, Bale. 2007. Deformation Bands and their Influence on Fluid Flow. *AAPG Bulletin*, V.91, 1685-1700.
- Gallup, W.B., 1974, The geological history of McMurray-Clearwater deposition in the Athabasca oil sands area, in L.V. Hills, *Oil Sands: Fuel of the Future: Canadian Society of Petroleum Geologists Memoir* 3, p. 100- 114.
- Holt, R.M. 1990 Permeability reduction Induced by a Nonhydrostatic stress Field. *SPE Formation Evaluation*, Decemeber.
- Jones, C., Al-Quraishi, A. A. and Somerville, J.M. 2001. Stress Sensitivity of Saturation and End Point Relative Permeabilities. *Society of Core Analysis*.
- Johnson, E. F., Bossler, D.P., and Naumann, V.O. 1959. Calculation of Relative Permeability from Displacement Experiments. *Trans., AIME*, 216, 370-372.

- Kosar, K.M. 1989. Geotechnical Properties of oil Sands and Related Strata. Ph.D. Dissertation, U of Alberta, Edmonton, Alberta.
- Kumar, M., Satik, C., and Hoang, V. 2005. New Developments in Steamflood Modeling. SPE 97719 presented at SPE International Thermal Operations and Heavy Oil Symposium, Calgary, Canada. November 1-3.
- Li, P. 2006. Numerical Simulation of the SAGD Process Coupled with Geomechanical Behavior. . Ph.D. Dissertation, U of Alberta, Edmonton, Alberta.
- Li, L., Holt, R.M. 2002. Particle Scale Reservoir Mechanics. Oil and Gas Science and Technology-Rev. IFP, Vol. 57, No 5, pp 525-538.
- Lake, L.W. 1989. Enhanced Oil Recovery, Prentice Hall, New Jersey.
- Masih, S, 2006. A New Technique to Measure Steam Relative Permeability for Better Performance Prediction of SAGD. M.S Thesis, U. of Regina, Regina, Canada.
- Morita, N., Gray, K.E., Srouji, F.A.A and Jogi, P.N. 1992. Rock-Property Changes During Reservoir Compaction. SPE Formation Evaluation, September 1992.
- Meyer, R.F., and Attanasi, E.D. 2003. Heavy Oil and Natural Bitumen – Strategic petroleum Resource. USGS Fact Sheet 70-03, August.
- Morse, R.A., Terwilliger, P.L. and Yuster, S.T. 1947. Producers Monthly 9, nr. 10, 19.
- Oldakowski, K. 1994. Stress Induced Permeability Changes of Athabasca oil Sands. M.S Thesis, U. of Alberta, Alberta, Canada.
- Osaba, J.S. 1951. Laboratory Measurements of relative permeability. Trans., AIME, 195, 329.
- Owens, W. W., Parrish, D. R., and Lamoreaux, W. E. 1956. An Evaluation of a Gas Drive Method for Determining Relative Permeability Relationships. Trans., AIME, 207, 275.
- Ozgurell, Gurkan.H., and Cumaraswamy Vipulanandan, 2005. Effect of Grain Size and Distribution on Permeability and Mechanical Behavior of Acrylamide Grouted Sand. Journal of Geotechnical and Geoenvironmental Engineering, Vol. 131, No. 12.
- Plewes, H.D. 1987. Undrained Strength of Athabasca Oil Sand. M.S Thesis, U of Alberta, Edmonton, Alberta.

- Ruistuen, H., Teufel, L.W. and Rhett, D. 1999. Influence of Reservoir Stress path on Deformation and Permeability of Weakly Cemented Sandstone Reservoirs. SPE Reservoir Eval. & Eng. 2 (3), June.
- Rhett, D.W. and Teufel, L.W. 1992. Effect of Reservoir Stress path on Compressibility and Permeability of Sandstones. SPE 24756 presented at 67th Annual Technical Conference, Washington DC, 4-7 Oct.
- Richardson, J.G. 1957. The Calculation of Waterflood Recovery from Steady-State Relative Permeability Data. Trans., AIME 210, 373.
- Richardson, J. G., Kerver, J. K., Hafford, J. A and Osoba, J. S. 1952. Laboratory Determination of Relative Permeability, Trans., AIME, 195, 187.
- Scott, J.D., Adhikary, D. and Proskin, S.A. 1991. Volume and Permeability Changes Associated with Steam Stimulation in an Oil Sand Reservoir. Presented at Petroleum Society of CIM and AOSTARA Tech Conf, Banff, Alberta, April 21-24.
- Samieh, A.M and Wong, R.C.K. 1997. Deformation of Athabasca Oil Sand at low Effective Stresses under Varying Boundary Conditions. Canadian Geotechnical Journal, Vol 34, 985-990.
- Tian, Zhongyuan and Lu, Lianhai. 2000. Determining Petrophysical Parameters of rock during Phase Displacement with CT Technique. SPE 64768 presented at SPE International Oil and Gas Conference and Exhibition, Beijing, China, 7-10 Nov.
- Tohidi-Baghini, A. 1998. Absolute Permeability of McMurray Formation Oil Sands at Low Confining Stresses. Ph.D. Dissertation, U of Alberta, Edmonton, Alberta.
- Li, L and Holt, R.M. 2002. Particle Scale Reservoir Mechanics. Oil and Gas Science and Technology-Rev. IFP, Vol. 57 (2002), No. 5 525-538.
- Terzaghi, K. 1943. Theory of Elasticity. New York City: McGraw-Hill Book Company.
- Wilhelms, A, S. R. Larter, I. Head, P. Farrimond, R. di Primio, and C. Zwach. 2001. Biodegradation of oil in uplifted basins prevented by deep-burial sterilization: Nature, v. 411, p.1034-1037.
- Yaich, E. 2008. The Effect of Stress Paths and Shear Failure on the Permeability of Unconsolidated Sands. M.S Thesis, U. of Texas at Austin, Austin, Texas.
- Wong, R.C.K. 2004. Effect of Sample Disturbance Induced by gas Exsolution on Geotechnical and Hydraulic properties Measurements in Oil Sands. Paper 2004-071 presented at the Canadian Intl. Petroleum Conference, Calgary, 8-10 June.

- Wong, T.-F., Baud, P., Klein, E. 2001. Localized failure modes in a compactant porous rock. *Geophysical Research Letters* 28 (13), 2521–2524.
- Wilson, J.W. 1956. Determination of Relative Permeability under Simulated Reservoir Conditions. *JAIChe* 2(1), 94-100.
- Welge, H. J. 1952. A Simplified Method for Computing Oil recovery by Gas or Water Drive. *Trans., AIME*, 195, 91.
- Zoback, M.D. and Byerlee, J.D. 1975. Permeability and Effective Stress. *AAPG Bulletin* 59, 154-58.
- Zoback, M.L, and Zoback, M.D. 1989. Global Patterns of Tectonic Stress. *Nature* 341:291-298.